A Proof Of Principle Nuclear Forensics Technique for Determining ^{235}U Enrichment from UF_6 Steel Cylinders

by

Morgan C. Collins

A thesis submitted to the

School of Graduate and Postdoctoral Studies

in partial fulfilment of the requirements for the degree of

Master of Applied Science

in

Nuclear Engineering

Department of Energy and Nuclear Engineering

University of Ontario Institute of Technology (Ontario Tech University)

Oshawa, Ontario, Canada

December 2023

THESIS EXAMINATION INFORMATION

Submitted by: **Morgan C. Collins**

Master of Applied Science in **Nuclear Engineering**

Thesis title: A Proof Of Principle Nuclear Forensics Technique for Determining ^{235}U Enrichment from UF_6 Steel Cylinders

An oral defense of this thesis took place on November 27th 2023 in front of the following examination committee:

Examining Committee:

Chair of Examining Committee	Prof. Jennifer McKellar
Research supervisor	Prof. Markus H.A Piro
Research Co-Supervisor	Dr. Bernard W.N. Fitzpatrick
Examining Committee Member	Prof. Edward Waller
Thesis Examiner	Dr. Ike Dimayuga, Canadian Nuclear Laboratories

The above committee determined that the thesis is acceptable in form and content and that a satisfactory knowledge of the field covered by the thesis was demonstrated by the candidate during and oral examination. A signed copy of the Certificate of Approval is available from the School of Graduate and Postdoctoral Studies.

ABSTRACT

Non-proliferation of nuclear materials depends on international regulations and the inspection tools available to safeguard inspectors for ensuring adherence to international treaties such as the Non-Proliferation Treaty (NPT). In collaboration with Dr. Michael P. Short (MIT) and the Mesoscale Nuclear Materials Group, this work investigated UF_6 cylinders as a proof of principle to determine whether steel materials can be used as forensic materials for uranium enrichment. SEM, EDS, XPS, ToF-SIMS, TEM and FlashDSC were performed to determine if the surface deposition left chemical or damage signatures that could infer the presence of high enrichment ^{235}U via the decay products present. Additionally, compositional and calorimetric analyses were performed to identify if radiation damage was detectable in the outer layer of the oxide, and was differentiable from chemical damage. The conclusion of this work indicates UF_6 drums hold significant forensics information, and have promise for future research as an inspection tool.

Keywords: Radiation Damage, Nuclear Forensics, Material Characterization, Safeguards, Non-Proliferation

AUTHOR'S DECLARATION

I hereby declare that this thesis consists of original work of which I have authored. This is a true copy of the thesis, including any required final revisions, as accepted by my examiners.

I authorize the University of Ontario Institute of Technology (Ontario Tech University) to lend this thesis to other institutions or individuals for the purpose of scholarly research. I further authorize University of Ontario Institute of Technology (Ontario Tech University) to reproduce this thesis by photocopying or by other means, in total or in part, at the request of other institutions or individuals for the purpose of scholarly research. I understand that my thesis will be made electronically available to the public.

Morgan C. Collins

STATEMENT OF CONTRIBUTIONS

I hereby certify that the entirety of this thesis is of my own work, and no part has been published or is currently submitted for publication. Throughout the report, standardized citation practices were utilized to reference and acknowledge the work of others, and any techniques or materials utilized.

SEM, EDS and XPS Analyses:

The work for SEM, EDS and XPS analyses was performed at the Materials Characterization Facility at Ontario Tech University. XPS analysis data collection was performed by Dr. I. Ebralidze. Data collection for SEM and EDS, along with all experimental data analyses, were performed by myself.

FIB, TEM and ToF-SIMS:

The work for FIB, TEM and ToF-SIMS was done at the Open Center for the Characterization of Advanced Materials at the University of Toronto, and data collection was performed by P. Brodersen. Data analysis and creation of report content was performed by myself.

FlashDSC:

The work for FlashDSC was performed in the Mesoscale Nuclear Materials Group Laboratory at the Massachusetts Institute of Technology. A. Nguyen and D.R. Reinfurt assisted me with experimentation and data collection.

ACKNOWLEDGEMENTS

Dr. E. Geiger is thanked for helpful discussions and sample preparation. A. Pandhi (UofT) is thanked for guidance of and significant help with figure creation. R. Ulrich is thanked for all the assistance, work and discussions around the preparation of the samples. F. Arnaldo is thanked for assisting with all regulatory issues and safety precautions regarding transportation and preparation of the samples. Dr. J. Howe (UofT) is thanked for helpful discussions and assistance when working with OCCAM at UofT. P. Broderson (UofT) is thanked for performing the TEM and SIMS measurements, as well as helpful discussions regarding planning analyses. A. Nguyen (MIT) and D.R. Reinfurt (MIT) are thanked for helping perform the FlashDSC measurements, show me around MIT, as well as for helpful discussions. M. Laughter (IAEA) is thanked for helpful discussions regarding industry knowledge, and for providing helpful information for my overall thesis topic. Dr. R.S. Kemp (MIT) is thanked for helpful discussions regarding thesis results while performing work at MIT.

First, I'd like to acknowledge the significant impacts of Bernie and Markus on my degree, and my future in academia as a whole. When I began my degree, I didn't know about graduate work or how to write a paper, but here I am now, hopefully submitting a thesis deserving of an acceptance. The efforts of both of you in being both my supervisors and mentors throughout my degree have helped me to get where I am today, more than you realize. I could not be more grateful for what both of you have done for me, and how you have impacted my future.

I'd like to thank Bernie for the numerous occasions where I would send an email asking for help, and receive a response almost immediately saying that it was no problem and that a call at 10 pm would work. Bernie always went above and beyond as a supervisor to this project, and I sincerely cannot thank him enough for the time, effort and mentoring that went into my time as a graduate student. I definitely would not have gotten through my first research project, let alone 3 without your guidance, especially at the beginning of my time here.

I would like to thank Markus for giving me the opportunity to be where I am today, as without both his pushing, and his help when I was just a previous student, I would not have ended up in graduate school. Coming from reaching out for resume help, to submitting a thesis was quite a jump, but I am very glad to have done it, and gone down the path I did. I appreciate everything you have done in the past 2 (and a bit) years, for always taking time to have a chat, and for helping with issues when they were urgent. Thanks for always looking out and helping with my future.

I'd like to thank Mike Short for the numerous conversations about both my research and the concept of nuclear forensics, as well as being a huge contributor to this research so far. I appreciate you taking time at the conference to go through my entire presentation while giving me tips on data analysis and layout. My conversations with you are a big part of my interest in the nuclear forensics and material characterization fields.

Thank you to K.J. McInall, G.J. Francolini. K. Sawatsky, and N.L. Scuro for always listening to my rants and complaints about how my research was going horribly, for having discussions about my research, and giving me advice when it was needed. I'd also like to thank the Nuclear Fuels and Materials Group as a whole for always being supportive as a community.

Lastly, I would like to thank my family for always supporting and believing in me, even when responding to calls and texts isn't my best skill. Thank you to my partner for always being supportive, accommodating, and helping me through tougher times when I really needed it. I would not be here without the extensive support throughout the years from you all.

This research was undertaken, in part, thanks to funding from the Canada Research Chairs (950-231328) and Discovery Grants program of the Natural Sciences and Engineering Research Council of Canada. We also thank Cameco Corporation for donating the UF_6 cylinder samples used in this work. M. Murchie is thanked for facilitating the donation of the samples to the university, and for arranging delivery of the shipment.

We acknowledge the Ontario Tech University Materials Characterization Facility, which is supported by the Canada Foundation for Innovation (CFI), NSERC Research Tools and Instruments (RTI), and Ontario Tech University.

CONTENTS

List of Figures

LIST OF TABLES

ABBREVIATIONS

BE: Binding Energy

CNSC: Canadian Nuclear Safety Commission

EDS: Energy Dispersive Spectroscopy

FIB: Focused Ion Beam

HEU: Highly Enriched Uranium

ICP-MS: Inductively Coupled Plasma Mass Spectrometry

LEU: Low Enrichment Uranium

MIT: Massachussetts Institute of Technology

NPT: Non-Proliferation Treaty

NU: Naturally enriched Uranium

OCCAM: Open Centre for the Characterization of Advanced Materials

SEM: Scanning Electron Microscopy

SIMS: Secondary Ion Mass Spectrometry

ToF-SIMS: Time of Flight Secondary Ion Mass Spectrometry

TEM: Transmission Electron Microscopy

T_A: Annealing Temperature

T_M: Melting Temperature

UF_6: Uranium Hexa-fluoride

UofT: University of Toronto

XPS: X-ray Photoelectron Spectroscopy

1

INTRODUCTION

With nuclear energy viewed to play a prominent role to combat climate change concerns and a number of international nuclear power reactors currently under construction, the use of nuclear power is expected to continue to expand internationally [2]. Due to the history involved with nuclear energy, the handling of nuclear materials is heavily regulated, with oversight by various governmental agencies (e.g. Canadian Nuclear Safety Commission (CNSC)), as well as the International Atomic Energy Agency (IAEA) as an international inspector. The role of these inspectors and regulators is to ensure adherence to the Non-Proliferation Treaty (NPT), which limits the production of Highly Enriched Uranium (HEU) internationally [3]. Verifying uranium enrichment and NPT compliance can be challenging, with few ways to confirm, with those methods being difficult and time consuming. The concern with proliferation generally does not include Low Enriched Uranium (LEU), or High-Assay Low Enriched Uranium (HALEU), and is focused on preventing the production of HEU.

The aim of this work was to explore the viability of a new proof-of-principle forensics method for the potential determination of ^{235}U enrichment levels in UF_6 steel cylinders, which are commonly used to transport and store UF_6 within the fuel fabrication and enrichment process. The development of such a technique is hoped to provide an additional tool-set that IAEA inspectors could potentially

use, but requires significant research and development time before it could reach a state past proof of principle. The introduction to this thesis aims to provide context to the nuclear forensics issue in regards to current international affairs, as well as the difficulty and issues that forensics currently faces. While the use of 48Y cylinders in the proliferation and transport of HEU is highly unlikely, the knowledge and experiences gained from the performance of characterization on the material can be used in future research after validation that metals, and specifically steels are likely hold significant enough information for enrichment determination.

The introduction of this thesis outlines the concept of proliferation and the role of international inspectors and regulators in the efforts to combat proliferation of nuclear materials. A brief explanation will be given of the specific 48Y steel cylinders used in this work, as well as the regulations that they must adhere to is given (Section 1.3.2), with a final explanation of material characteristics and how it both applies to (Section 1.3.1), and is vital to the progression of the nuclear forensics field (Section 1.3).

1.1. NUCLEAR PROLIFERATION

Nuclear proliferation is an effort to produce or obtain nuclear materials for use in nuclear weapons production through non-regulated means, whether this be fissionable isotopes, enriched uranium, or weapons-ready technologies [4]. Generally the term is used to define the manufacture, transfer, or acquiring of nuclear weapons by non-nuclear states, as defined by the IAEA. Proliferation of nuclear materials can occur through various methods, with the main intent being to distribute or obtain large amounts of HEU such that nuclear weapons can be produced, whether this be by malicious entities, or bodies outside of proliferation treaties. Outside of certain ratifiers defined within international treaties, the production of HEU is not accepted, as well as the production, concealment, or holding of nuclear weapons [4]. Preventing the proliferation of nuclear materials is defined as non-proliferation, indicating the methods taken, and regulatory efforts put towards ensuring safe nuclear energy, and preventing future building of nuclear weapons within the international community.

1.1.1. INTERNATIONAL TREATIES AND REGULATIONS

To prevent proliferation of nuclear materials, a number of international treaties and agreements have been signed over the years addressing concerns and providing avenues for ensuring safety and adher-

ence. The Treaty on the Non-Proliferation of Nuclear Weapons, or Non-Proliferation Treaty (NPT) was a global effort to prevent the spread of nuclear weapons, and reduce the risk of proliferation [3]. Signed and ratified in 1968 - 1970, the treaty was proposed to act as an intermediary as the threat of using nuclear weapons was used as a deterrent between nations. The objective of the treaty had three points, with those being: i) disarmament of nuclear weapons, ii) non-proliferation of nuclear weapons, and iii) the safe use of nuclear for energy purposes. Verifying each nation state is in adherence to the NPT was difficult, and the IAEA was selected as an international body to verify nation states were in compliance with the NPT, by performing inspections within nuclear facilities. To perform these inspections, the agency requires a set of tools that allows them to determine whether agreements are being followed. This generally includes tools that can identify and quantify HEU, or other proliferated materials with enough accuracy and confidence to act upon results.

Designated as a non-nuclear weapon state, and a ratifier of the NPT, Canada does not produce HEU for commercial or power production reasons at this time [3]. The Canadian Nuclear Safety Commission, has designated a regulation document outlining the requirements and regulations of an operational nuclear facility within Canada, to ensure proliferation of nuclear materials does not occur [5]. REGDOC-2.13.1, "Safeguards and Nuclear Material Accountancy", outlines the commitment to ensuring radioisotopes are accounted for at all stages of the uranium production process, and proliferation of potential weapons grade materials is limited as much as possible [5]. The materials that are considered radioisotopes, or materials of concern for proliferation are outlined, as well as guidelines for reporting mass accountancy, and inspection of fissile material stores. Additionally, the document allows IAEA inspectors full access given adequate notice of a request, allowing inspections to be performed at nuclear facilities such that adherence to both international regulations, and non-proliferation treaties is upheld.

An additional protocol, that being the Agreement Between the Government of Canada and the International Atomic Energy Agency for the Application of Safeguards in Connection with the Treaty on the Non-Proliferation of Nuclear Weapons, was signed in addition to the NPT between Canada and the IAEA. The supplemental protocol, initially signed in 1972, was updated in 2000, with the main purpose being that Canada accepts the use of safeguards pursuant to the agreement on all fissionable material within the country, or under its control [6]. The terms further outline the agreeance between

Canada and the IAEA on the topic of ensuring proliferation of nuclear materials does not occur, and nuclear weapons are not further distributed or produced [6]. The document outlines provisions and protocols on the transfer, safeguarding, and distribution of fissile material by Canada to prevent or reduce the possibility of proliferation [6]. Additionally, the requirement that all fissionable material is quantified and strict records kept was stated, and material must be tracked at all times [6].

1.2. ENRICHMENT AND THE INTERNATIONAL COMMUNITY

Typically, UF_6 is used in the production of enriched uranium based reactor fuels (such as Pressurized Water Reactor and Boiling Water Reactor fuel forms) [7]. Currently it is the only uranium bearing compound capable of being used in commercial enrichment methods as it remains both the sole uranium compound known to be in a gaseous phase at modest temperatures and pressures, as well as containing fluorine, which has only one stable isotope. Together, these attributes are useful for centrifuge processing [7, 8]. Throughout commercial enrichment processes, UF_6 is often stored within standardized cylinders for storage and transportation of the material to the next stage of the fuel cycle [9]. While Canada does not commercially enrich uranium, various operations across the globe store material that has been enriched, or is currently undergoing the enrichment process within either 48Y or 30B cylinders. These cylinders are utilized during the conversion to enrichment phases, where UF_6 is transported and stored. As can be seen in Figure 1.1, the conversion process takes place before enrichment or fuel fabrication, and this is where 48Y cylinders are utilized. Additionally, the deconversion process takes place after enrichment, where UF_6 would be converted back to UO_2 after enrichment.

On that concept, widening the possible options for detecting enrichment has issues due to the micro-scale nature, and difficulty of detecting radiation damage in the low quantities required to isolate nuclear weapons levels of enrichment. Tools and technologies for determining enrichment are difficult and generally include obtaining a bulk material sample of the uranium in question and performing an isotopic analysis using mass spectrometry methods to determine enrichment [10]. While this method is high in accuracy, the requirement for high material mass, and ability to hide or conceal material that would have a higher enrichment is possible. Ensuring minimal damage to both the equipment in use by the operating facility and ensuring the material mass is low enough such that small samples can be taken from anywhere would reduce the ability to conceal HEU. Additionally,

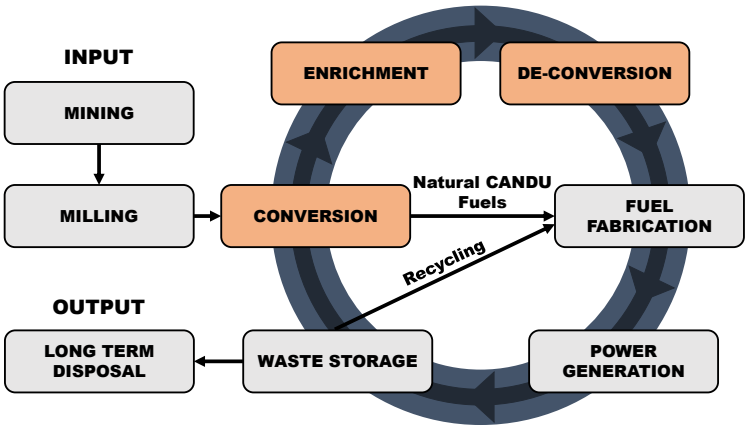

Figure 1.1: Overview of the nuclear fuel cycle, indicating the conversion process can directly lead to either enrichment, or fuel fabrication where 48Y, or 30B cylinders would be used to hold UF_6.

many tests and tools require specific equipment, with the most likely being the use of a colimmated channel with gamma detector that can determine enrichment, but requires specific, expensive equipment that is hard to transport and setup remotely and process samples [10].

1.2.1. ENRICHMENT REQUIREMENTS

Enrichment of uranium requires significant processing utilizing gas centrifuges before HEU can be produced, or an enrichment suitable for weapons production [7]. The setups required for enrichment are large, often requiring a cascade of dozens to hundreds of centrifuge machines to obtain HEU as an output [11]. Due to the large required setups, the potential materials for use within the enrichment process are numerous, but have low radiation damage signatures. Determination of enrichment through physical examination of output uranium is both the easiest, and highest accuracy method of enrichment determination, but the potential for malicious concealing of singular containers of uranium is too high to depend on [10, 11]. The point of interest for future research has turned to components within the enrichment process, including machine parts from centrifuges, as well as intermediary steps such as the storage cylinders that hold UF_6. The main method for investigating these components includes the use of nuclear forensics, a series of techniques used for characterizing and identifying markers within materials.

1.3. NUCLEAR FORENSICS

Forensics is the science of characterizing materials and identifying material markers on the (often) micro-scale size, in the hopes of determining information not inherently visible or clear without specialized methods [12]. Nuclear forensics as an independent field looks to combine forensics with materials science to detect trace amounts of nuclear material or radiological effects through a preventative, or post-event analysis. With non-proliferation as a concern, the focus is on preventative measures to detect the transport, proliferation, and/or enrichment of nuclear material.

To support the prevention of unauthorized or unwanted enrichment within the international community, forensic tools are being developed to detect minuscule traces of nuclear materials that can determine both the origin of the uranium and enrichment in terms of potential danger. By expanding the list of available tools, the scenarios in which an appropriate tool is available to confirm adherence increases, reducing the scenarios in which mistrust of results or parties is present. Nuclear forensics target choices are limited to materials that are readily available, hard to conceal, and contain fingerprints significant enough for data retrieval. Additionally, options that allow quick access to the material without causing extensive monetary damages through the destruction of assets are favoured, to reduce any conflicts that may arise with testing of enrichment apparatus. These constraints lead to a number of paths which future research can focus on, including but not limited to: Storage containers, intermediary tubing and pipes, and centrifuge mechanisms and material as the main foci.

1.3.1. MATERIAL CHARACTERIZATION

Characterization of materials in the micro-scale generally takes on three forms, including characterization of the surface composition and phase, calorimetry, or chemical bonding and structure. Each form utilizes a separate set of analysis methods and focuses on the specific material properties associated with the intended target. As nuclear forensics focuses on mesoscale changes and the atomic structure, or influences of radiation damage on the material, all three paths provide significant information on the history of the material regarding interactions with nuclear materials.

Surface characterization focuses on determination of composition of the material, or the specific phases in which the material presents under given conditions. Many methods utilize various mi-

croscopy or spectroscopy methods (to be discussed within Chapter 4) to determine the surface composition of the material to determine the physical effects on structure that are caused by chemical or radiological interactions. Additionally, phenomena such as re-crystallization or oxidation effects can be observed, determining the formations and grain structure differences of the material. Calorimetric data investigates the stored energy within the lattice, or the changes in heat capacity within the material caused by outside influences such as radiation damage, or changes to the chemical composition of the material after chemical reactions and phase changes. These are often less visible with microscopy based techniques, and are difficult to quantify without isolation of the target material in significant quantities. Analysis of the chemical bonding or structure of a crystalline lattice within a material presents information regarding the phases present, as well as the molecules and compounds that have formed within the material. These analyses give detailed information on the bonds that have formed and provide info on what specific chemical interactions and compositions may have been present during interactions. The use of each analysis background together forms the basis of forensics, specifically when investigations involve micro-scale sizes that make visual inspection difficult.

1.3.2. CYLINDER SPECIFICATIONS AND REGULATIONS

While the material in question was selected for investigation, understanding the exact specifications, and consistency in results was vital for finding a direction to start in. To perform material characterization, and identify forensic markers, a material in constant contact with UF_6, or another enrichment based material was needed, which indicated hope for the standard 48Y cylinders. The specifications for safe handling and storage of UF_6 are given in ANSI N14.1 and ISO/7195 [9]. Two cylinder types, with slightly differing constructions and regulations are utilized depending on whether the uranium in question is naturally enriched, or has gone through the enrichment process [9, 13]. Naturally enriched uranium is held within 48Y cylinders (the cylinders utilized within this research), whereas enriched uranium is held within a 30B cylinder. From the conversion process to enrichment, a 48Y cylinder is utilized, and after enrichment, the uranium is deposited within a 48Y cylinder for storage and transportation purposes [9, 13].

Compliance with ANSI N14.1 and ISO/7195 indicate a potential range of metal grades to be utilized, but the specific cylinders within this work adhered to ANSI N14.1, and were constructed of A516

steel, grade 65 or 70. While of differing grades, the major composition changes consist of carbon and chromium content between the two. Grade 70 generally has higher tensile strength, and a higher working temperature, which should not have any significant impact on this work when considering the differences between grades. The exact grade will have to be known before performing forensics work on a specific cylinder, but for this purpose any effects should be negligible. While this work is performed on 48Y cylinders (seen in Figure 1.2) and enriched uranium materials will use 30B cylinders, which adhere to slightly differing construction standards, the information found through the completion of this work will be applicable, and will determine if the material is viable for future research. The specific differences between cylinder types consist of slightly different constructions and specifications, but the circumstances surrounding the storage of uranium and the materials used in construction are very similar. The underlying concepts for determining radiation damage and the relationships on enrichment will be independent of the exact material composition of the cylinders. Due to the stringent regulatory requirements on cylinder construction, the chemical makeup, and therefore, chemical and radiological damage influences within the material should be similar in nature to those of differing construction for various uses.

Figure 1.2: Photograph of a 48Y cylinder used to store UF_6 [14]. Dimensions of a 48Y cylinder are: 150” in length with a diameter of 48”.

1.4. REPORT LAYOUT

The layout of this thesis is as follows: the overall objectives and tasks are laid out in Chapter 2, followed by a background of the subjects discussed, and a review of literature of parallel studies in Chap-

ters 3 and 4 respectively. A description of all methodologies used for sample preparation and analysis is given in Chapter 5 with the obtained results presented in Chapter 6. This is followed by a discussion and comparison of the results in Chapter 7. Finally, conclusions of the work are summarized in Chapter 8, before additional recommendations on future research are given in Chapter 9, for if this topic is to be continued in the future.

2

STATEMENT OF WORK

2.1. PROBLEM STATEMENT

For nuclear forensics to be used as a tool to help determine uranium enrichment in inspection based scenarios, a deep understanding of the radiation damage, and chemical interactions of a material are required. While there is hope for UF_6 to contain a viable ^{235}U fingerprint for future enrichment determination, the material has received very little previous research in terms of material characterization, especially in regards to radiation damage of the material. Due to the meso-scale size of the potential damage, as well as the highly reactive elements present, little knowledge on the inner damage mechanisms of the material are available. While several other materials have had previous research performed, significant headway will be required for UF_6 to be considered a viable material for forensics inspections. As such, the use of a variety of characterization methods is required to determine validity, and consistency of the results, to understand the material interactions in a storage environment.

2.2. OBJECTIVE STATEMENT

The main objective of this work was to perform a proof of principle analysis to determine whether any forensic fingerprints in the surface layer were both identifiable and quantifiable to potentially determine ^{235}U enrichment levels. In this work, 48Y cylinders that previously contained UF_6 were used to test a number of characterization techniques to quantify results such that they could be benchmarked and correlated against one another to validate consistency. The results of this work were then to be used to determine whether UF_6 cylinders are viable for future characterization research of enriched 30B cylinders, and hopeful eventual use in an inspection program for forensics enrichment determination.

2.3. PROJECT TASKS

To complete the above central objectives, a number of tasks were set such that efforts could be categorized and kept on track. Each task was established as a goal such that a decision on viability of the sample as a forensics option could be made after each step, to confirm the research was heading in the correct direction.

1. Determine and develop method for the sectioning and preparing material samples for use in various analysis methods.

2. Utilize Scanning Electron Microscopy (SEM) and Energy Dispersive Spectroscopy (EDS) to validate sample health, and determine if overall oxide formation was viable for further investigation.

3. Investigate radiation damage markers using Transmission Electron Spectroscopy (TEM) and X-Ray Photoelectron Spectroscopy (XPS) to observe micro-scale changes in the material.

4. Perform Flash Differential Scanning Calorimetry (FDSC) calorimetric measurements in collaboration with the Massachusetts Institute of Technology, and corroborate surface characterization results.

5. Produce an outline of viable methods for further investigation of forensic fingerprints for future research.

3

BACKGROUND

This chapter of gives a background of the various aspects of nuclear forensics, specifically in the case of steel 48Y cylinders used to store UF_6. An overview of forensics history will be followed by how radiation causes damage in steels, as well as the corrosion expected to occur over the cylinder lifetime, with a final description of the surface characterization techniques utilized within this research.

3.1. HISTORY OF NUCLEAR FORENSICS

The concept of nuclear forensics was first introduced in the early 1990s, in which there was a concern with the identification of unclaimed nuclear materials and potential trafficking for nefarious purposes. The main question focused how a source of weapons grade nuclear material be identified through a small fingerprint left in the material, such as contaminants or other visible materials information [12]. That question led to decades of further research in which the ability to identify and quantify nuclear materials has improved significantly but the issue of concealment or proliferation of nuclear materials is still a significant security concern on both domestic and international fronts. To help reduce proliferation concerns, research has been conducted on the ability to identify the production of singular

amounts of HEU within a traditional supply chain [15, 16]. These methods look to use materials within the supply chain to identify characteristics or radiation damage within the material itself to quantify the fingerprint leftover by HEU. While this work focuses on the quantification of ^{235}U, it isn't the only isotope that is considered, the most significant other component being ^{239}Pu. This isotope is generally proliferated through re-processing of spent fuel, and as such would be found within the other side of the fuel production cycle, far from the conversion and enrichment stages in common commercial production.

The main method for quantification of enriched uranium has been the detection of unintended inclusions from the supply chain (such as traces of locational resources) used to produce the material [10]. This concept, while being able to identify HEU given a sample of the material, cannot identify if equipment has been used to produce HEU in the past. Commonly, the use of Inductively Coupled Plasma Mass Spectrometry (ICP-MS) has been employed to measure the composition of trace elements within aqueous solutions [17]. These solutions can be prepared from samples of uranium material from inspection points to be evaluated for ^{235}U. One common point across previous inspection techniques is the requirement for large uranium samples (samples must be isolatable, and prepared for ICP-MS) to determine enrichment [17].

Several points of interest with significant contact with uranium during the supply chain have been identified and are in the process of being evaluated to determine the viability of the material's use as a forensic fingerprint. Whether the material has both a consistent and significant enough fingerprint for quantification of a damage signature, and eventual uranium enrichment are key-points for viability of the material. Materials in contact with uranium during the enrichment stages likely hold significant markers indicating the enrichment content, but the micro, or meso-scale of the damage leads to difficulties with retrieval and extraction of the information. This has led to a number of specialized methods being utilized to analyse atomic changes in material composition, structural integrity, and lattice structure to investigate changes after irradiation to levels similar to those in a traditional supply chain. Experiences using these techniques by other authors will be further described within Chapter 4.

These methods allow inspections to be performed on components within the enrichment supply chain to take material that is otherwise much harder to conceal or obscure than traditional inspection materials. Obscuring a singular container of enriched uranium is much more simple than upheaval

and replacement of a series of mechanical components exposed to enriched UF_6 gas. Widening the scope of inspection to increase the components within the chain able to be investigated improved security of the process, and makes obfuscation much more complex. Continuing to determine the materials that best display a fingerprint of the exposed enrichment contents will provide an avenue to continue research to expand the current list of materials available for forensics analysis on the uranium supply chain.

3.2. URANIUM DECAY AND RADIATION INTERACTIONS

Naturally occurring uranium contains three isotopes: ^{238}U, ^{235}U, and ^{234}U, in decreasing concentrations respectively. ^{238}U and ^{235}U are components of the ore, while ^{234}U is a product from the decay chain of ^{238}U and is produced in small quantities in a transient equilibrium with ^{238}U [1]. Decay of both ^{238}U and ^{235}U are incredibly slow, with half lives of the order of millions to billions of years, indicating a low specific activity for the isotopes without neutron interaction [1]. As such, the radiation produced, and subsequent decay of these isotopes into decay products happens in low quantities, leading to little potential radiation damage per time unit. The decay chains of both ^{235}U and ^{238}U indicate a number of isotopes that produce alpha or beta radiation in varying amounts and energies [1]. Tables 3.1 and 3.2 indicate the decay series for both isotopes with the produced radiation type upon decay and half life. Each series contains isotopes producing α and β radiation, as well as several isotopes with half-lives in the order of thousands to millions of years. Given steel's high resistance to wear and long use-time of 48Y cylinders, the steel surface will have received large relative fluences, even with low fluence per unit time period with the long half-lives of the decay chains. While ^{235}U has a half life roughly one order of magnitude lower than that of ^{238}U, due to the low concentration in natural uranium, ^{238}U and ^{234}U contribute roughly 98% of the activity, while contributing roughly 99.28% of the mass by weight. Both ^{234}U and ^{238}U are roughly equal in activity due to the secular equilibrium present within the decay chain, as the half life of ^{238}U is magnitudes higher than that of ^{234}U [1]. The relative concentration of ^{234}U should remain stable over time, in accordance with the concentration of ^{238}U as it decays.

While alpha particles have adequate energy for causing knock-on effects [18], the excitations caused by beta interactions would likely not be permanent, or cause any significant visible damage in steel

Table 3.1: Uranium ^{235}U Decay Series [1]

Isotope	Half-Life	Radiation Type
^{235}U	7.04×10^8 y	α
^{231}Th	25.5 h	β
^{231}Pa	32 800 y	α
^{227}Ac	21.7 y	β
^{227}Th	18.7 d	α
^{223}Ra	11.4 d	α
^{219}Rn	3.96 s	α
^{215}Po	778 µs	α
^{211}Pb	36.1 min	β
^{211}Bi	2.1 min	α
^{207}Ti	36.1 min	β
^{207}Pb	Stable	N/A

Table 3.2: Uranium ^{238}U Decay Series [1]

Isotope	Half-Life	Radiation Type
^{238}U	4.5×10^9 y	α
^{234}Th	24.1 d	β
^{234m}Pa	1.2 m	β
^{234}U	244 500 y	α
^{230}Th	77 000 y	α
^{226}Ra	1600 y	α
^{222}Rn	3.8 d	α
^{218}Po	3.05 m	α
^{214}Pb	26.8 m	β
^{214}Bi	19.9 m	β
^{214}Po	63.7 µs	α
^{210}Pb	22.26 y	β
^{210}Bi	5.01 d	β
^{210}Po	138.4 d	α
^{206}Pb	Stable	N/A

materials [19]. As such, the main proponent of radiation damage in metals would be the production and interaction of alpha particles with the outer surface, as particle penetration would be limited. Alpha particles have low penetration coefficients already, and a high density material such as A516 steel would indicate a penetration depth in the nm range [15]. Due to this fact, the outer layer of oxide buildup on the steel surface would be influenced by radiation, while the bulk material inside would remain unaffected and without any significant radiation damage [15].

Alpha particles are emitted as a form of radiation when the nucleus decays to produce both an α particle, and an atom with a lower atomic mass than the original parent isotope. The general form of an α producing decay is given in Eq. 3.1, in which an α is produced with the same atomic properties as a ${}^{4}_{2}\mathrm{He}$. As such, for most intents and purposes it can be stated that α radiation produces a helium atom for the purposes of material characterization and compositional analyses.

$$ {}^{A}_{Z}X => {}^{A-4}_{Z-2}Y + {}^{4}_{2}\alpha \tag{3.1} $$

Alpha particles will cause knock-on effects when interacting with matter in two main ways: electronic stopping, and nuclear stopping [18]. Electronic stopping is the phenomena when energy from a particle transfers or is deposited into the electrons during inelastic interaction or slowing of the particle as it travels through a medium [18]. During this interaction the particle loses kinetic energy, which is transferred to electrons and (in this case) temporary excitation of the atom occurs. While both interaction mediums are prevalent, the two phenomena are largely isolated in occurrence as they rely heavily on particle energy at the time of interaction. At high energies, the α particle is much more likely to undergo electronic stopping, as it continues to interact with the lattice and lose kinetic energy, slowing down over time. Eventually, the kinetic energy of the particle becomes low enough that nuclear stopping overtakes it as the major interaction mechanism before completely yielding. A representation of the particle stopping power over time can be seen in Figure 3.1 in which the particle initially undergoes long tracks of electronic stopping as it loses energy before undergoing nuclear stopping and causing knock-on effects within the lattice. The localization of radiation damage markers will also concentrate further into the sample as the particle loses energy and undergoes a higher percentage of nuclear stopping, thereby losing more energy [18]. This causes localized helium concentrations to rise where

the expected particles are likely to come to rest. The total stopping power of the particle is given as a function of the nuclear stopping power [F_n] and the electronic stopping power [F_e], in which the sum is equal to the non-relativistic stopping power of the particle. This can be represented by Eq. 3.2 [18]:

$$F(E) = F_e(E) + F_n(E) \tag{3.2}$$

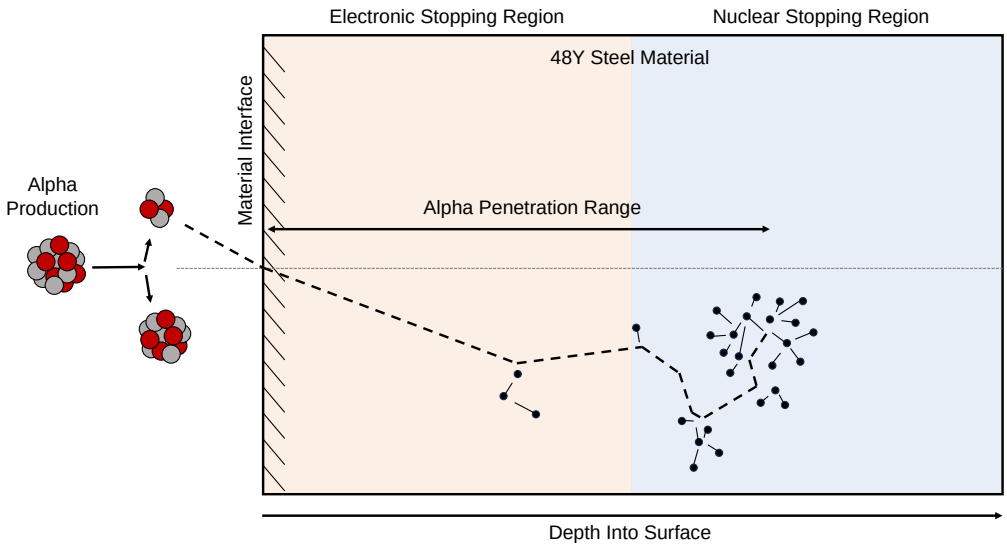

Figure 3.1: Representation of how an α particle will interact with the outer surface of the material. The particle will initially undergo electronic stopping before losing enough energy to undergo nuclear stopping, before coming to rest.

While certain materials are more susceptible to permanent effects caused by excitation of atoms within the particle's path, such as polymers, metals do not react significantly enough to excitation to cause permanent visible damage [18, 19]. Other materials may undergo polymerization, re-organization, or re-crystallization of the material which are valuable methods for understanding radiation damage absorbed if the material is susceptible, and will be discussed within Chapter 4 as the topic has been investigated previously [15]. In the case of uranium decay, the particles released will not likely have significant enough energy or undergo enough deflections to cause radiative stopping, often known as the release of Bremsstrahlung radiation [18]. As such, this phenomena does not have a significant impact on the damage received by the material surface.

Nuclear stopping, unlike the electron interactions of electronic stopping, is when a particle elastically interacts with the nuclei of an atom, leading to more pronounced permanent effects [18]. With the

relatively high energy of the alpha particles produced through decay of uranium [1], interaction of the particles with the material surface can lead to defect production, sputtering of the surface, and potentially re-crystallization or re-alloying of localized areas [15, 18, 20]. During interactions, the particle will cause dislocations or damage cascades as the atom that is impacted is displaced, locally disrupting the atomic lattice of the material, and causing defects, interstitials, and/or crystallographic changes [21]. The atom will continue to interact with other atoms in the lattice, leading to a cascade of interactions, fanning out to a larger area as the atoms continue to interact. This phenomena can lead to defect production and is the main cause of the higher interstitial defect concentration as is common with radiation effects, as atoms are implanted into the atomic lattice. As the particle interacts with atoms of the material, energy is deposited in an area and can lead to sputtering of the surface as rapid heating of localized areas can occur, causing atoms to be released from the lattice [18, 21]. Additionally, the rapid heating and cooling of localized areas can cause phase changes, or re-crystallization of the atomic lattice into other forms, as is more common in certain materials [20]. This can have significant effects on certain materials, but varies on the properties and composition of the target surface. Alloys with higher carbon compositions have been previously observed to undergo radiation induced effects, indicating the potential for alloy effects in steel materials [22]. It likely that under significant enough absorbed fluences, the grain boundaries of metals will begin to migrate or deform, which may be quantifiable through analytical means [23].

The dislocation of atoms from their initial position is an important damage mode for the quantification of received damage, as this movement, causing atoms to be displaced outside of the lattice results in potential energy to be stored due to added stresses [15, 24]. As atoms are displaced, they rest outside of the set planes and structures of the lattice, leading to stresses being placed due to voids or interstitial defects. These stresses within the lattice are removed through annealing of the material, or other working processes in other materials and will release the energy stored within the lattice as atoms shift locations, removing interstitial defects and filling voids. This energy can be quantified through other means, as will be discussed in Chapters 5 and 6.

Due to the kinetics of nuclear stopping vs electronic stopping, the highest concentration of defects or visible radiation damage in the material should occur at a distance into the oxide such that the kinetic energy as an average of all particles has dropped, leading to nuclear stopping interactions oc-

curring more frequently [18, 25]. This leads to the outer surface undergoing more electronic stopping, or non-permanent damage, while a majority of the damage being done is unseen, or located at a further depth below the surface. This effect is an average of all particle collisions, and as such a number of particles will undergo collisions near the surface, causing the path to run parallel to the surface of the sample, leading to radiation damage at lower depths.

If the material in question is crystalline, the lattice structure may lead to potential channeling of the particle, in which the particle travels parallel to a crystalline plane, passing through a gap in the lattice and interacting with fewer atoms [21]. This may lead to a much longer penetration path and few interactions along the way. With interactions such as this, the electronic stopping power losses of the particle will be greatly reduced, and the time for reduction of kinetic energy will be greatly increased, leading to a further depth for radiation damage to peak, or be visible. While this phenomena may occur in a number of materials, it is much more likely to occur in materials with specific and consistent crystallographic structures, and small ion sizes as to allow it to pass through without impediment.

As the penetration of the α particle into a material is heavily dependent on the energy of the incident particle, if the initial energy is higher, penetration further into the surface is more likely [25]. Due to this fact, there should be depths in which certain energy particles are more likely to deposit at the end of their penetration track due to the lower overall energy. If there is enough separation of particle energies, and with a high enough resolution detector, it may be possible to identify peaks that correlate to the energy of the incident particles. The average energy loss per interaction will correlate the mean penetration depth of the particle to the incident kinetic energy, and it is possible to calculate an average penetration depth for a particle with a set energy [25]. Attenuation or collisions before entering the surface of the material would lead to inconsistencies with incident energy of the particle, indicating that a sufficiently even or thin surface would be required for the accuracy needed to quantify results.

3.3. DISLOCATIONS AND DEFECT PROPAGATION

As atoms are hit by α particles, knock-on effects are caused as the particle loses energy, eventually coming to rest within the lattice itself, with both interactions causing dislocations and defects to form within the atomic structure [18]. These defects can be caused through a number of mechanisms, but the result is atoms being moved and transported through the atomic lattice, leading to vacancies and

interstitials forming as well as other effects on the overall structure of the material. One notable effect is the production of dislocation loops, which are a buildup of dislocations caused by knock-on effects that form a line or structure of dislocations that eventually close to form a loop structure within the lattice [26]. These dislocations are more likely to grow on certain planes, which are dependent on the crystalline structure of the material, and continually grow after exposure to a source of radiation as atoms are affected [26]. There are a number of ways that dislocation loops can begin forming, depending on the circumstances of the situation, as well as the crystalline lattice in which the defects are forming.

Dislocation loops are an effect caused by stacking dislocation or interstitial defects within a line congregate to form discs located between atomic planes. These formations continue to grow in size as additional defects are displaced, growing the fault such that loops, or cylindrical structures displaced within the lattice form, and are observable on macroscopic scales [26]. After the loops become fully formed, they continue to grow in radial size and can develop inner loops, leading to a cascade of dislocation loops [27]. It is worth noting that a dislocation loop can either be a disc of vacancies or interstitials, leading to an additional plane of atoms being placed within the structure of the material, or the removal of a plane [27]. Dislocation loops can be observed from certain unit directions where the planes of atoms can be seen shifted, causing a rift or disconnection between the contained atoms and the original plane. The disconnection forms various shapes depending on whether the loops is formed from interstitial or vacancy based defects, and will eventually grow in length and radial size to form a disconnected structure. This effect can be seen in Figure 3.2, where fully formed dislocations in the form of stacked ribbon faults are visible in the atomic structure planes. These dislocations generally form hexagonal or circular shapes within the crystalline lattice, spanning across and through planes, and can be observed to be within the μm scale within the material showcased. In this instance, the presence of a stacking fault led to the repeated ribbon pattern observed due to voids forming in the lattice, causing collapse [28]. The development of the dislocation loops can be measured in such a way, as by utilizing directional microscopy, the loops will light up and allow quantification of the defect propagation.

Dislocation loops provide a means to measure the number of defects within a material by examining the quantity and growth of the loops within specified planes of the structure. As dislocation loops

are more likely to form under certain planes, the loops located on certain unit vectors can be counted through microscopic analyses such as TEM [26]. Through measuring the size and number of dislocation loops, the estimated defect propagation associated with the loops can be quantified which can correlate the overall defect production within the material. It is worth noting that dislocation loops will not be observable in an amorphous material, requiring a consistent crystalline structure to be present to form them [27]. This is due to a consistent atomic pattern being required to form observable loops, as an amorphous material would not have differentiable planes within the surface to form loops [27]. As such, the presence of dislocation loops in oxide materials is less likely due to the low presence of consistent crystalline structures with oxide based metals.

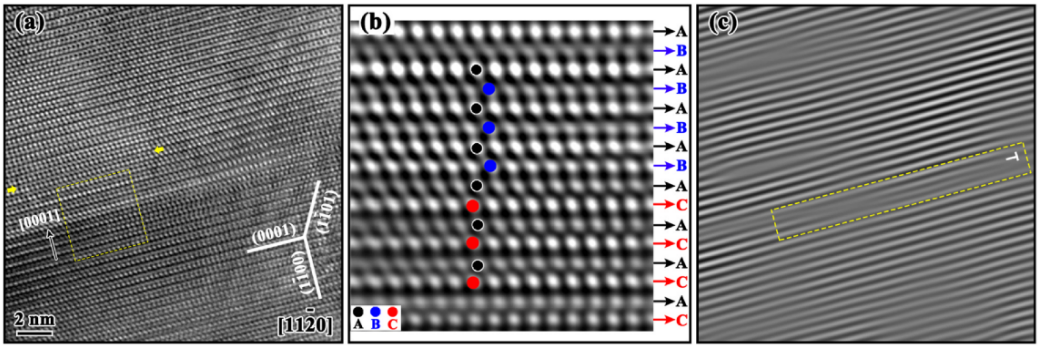

Figure 3.2: Example of stacking ribbon faults in a metal material from S. Wu, C. Cao, H. Bo *et al.* [28].

It is well understood that radiation induced dislocations are more likely to cause interstitial dislocations to be created than vacancies, which can be a factor causing swelling of the material as the volume increases with a higher ratio of interstitial defects [29]. While swelling is a relatively small issue until absorbed doses are very high, it can have an effect and be measured through microscopic means as a way of determining interstitial ratios [29].

Additionally, as the α particles come to rest, the atoms generally take place within the lattice, becoming a defect themselves, either becoming an interstitial or knocking other atoms out of the lattice and taking their place [18]. As α particles can be considered He atoms for the purposes of material characterization, this leads to the posited helium gradient within the sample surface as the particles come to rest after undergoing nuclear stopping and losing significant energy. The atoms will eventually stop, after enough collisions such that they rest near the point where most knock-on based effects are located [18]. The concepts of radiation damage discussed within this section will be utilized in the

context of analysing 48Y cylinders, to identify traces of ^{235}U damage as radiation damage isn't the only phenomena occurring to cause changes to the properties of the analysed cylinders.

3.4. 48Y CYLINDER CORROSION

Assuming the cylinders were not damaged significantly enough over their life-time to allow outside influences (e.g. atmospheric elements) to interact with the stored UF_6, the inner surface of the cylinders should have underwent corrosion within a predictable pattern. As described in Barber [30], a number of compounds are produced as UF_6 is exposed to outside atmospheric influence, indicating a general expected material gradient closer to the exposed surface. This gradient indicates the progression of the material from pure UF_6 to a ferric fluoride compound in the form of FeF_2.

The UF_6 within the cylinders is generally within solid form during storage phases as the ambient temperature is below the melting temperature of the material (64 °C), and the hydrostatic pressure is kept below the triple point (1.5 barr) [31]. The cylinders are filled with solid UF_6 and an overfill of gaseous UF_6 [31]. This limits the material movement during storage and reduces the potential interaction rates of the material with the metal surface. Additionally, this leads to potential composition gradients as the material moves further from the surface as UF_6 will minimally react with the alloy, causing compounds to form at the surface and remain there [30]. The conditions of the boundary between UF_6 and the metal surface significantly affect the corrosion rates observed, with higher HF_4 concentrations associated with heightened corrosion rates, and solubility of UF_6 compounds around the borders [30]. Reaction of UF_6 with ambient moisture contained within the material as a result of contamination during previous processes causes the production of HF_4. The resultant lower localized pH causes additional reactions to occur, leading to the heightened production of additional acid compounds, introducing a cyclic loop to the corrosion properties.

Previous research suggests that under normal conditions, UF_6 should cause minimal corrosion with the metal surface over the lifetime of the cylinders with only certain materials being more likely to undergo corrosion [30]. Those materials including nickel, which UF_4 would act as an oxidizing agent for, causing the production of NiF_2 and UF_3, or a number of other fluoride based compounds and depends on the partial pressure of UF_6 within the cylinder [31]. It is unlikely that the cylinders underwent significant enough atmospheric exposure to cause oxidation and reaction to that extent,

but the ambient oxygen and moisture contained within the UF_6 was likely enough to form HF_4. The increased concentration of acid compounds can cause reaction of the UF_6 with the metal surface, leading to the production of the iron and or uranium fluoride compounds seen in Table 3.3. The table lists the compounds experimentally observed to occur as the iron metal and UF_6 transition through corrosion to a series of fluoride materials. These compounds have been determined to have certain identifying properties and are likely to form from the metal surface, causing the formation of deposits on the surface. These deposits are likely to remain affixed to the cylinder surface, or become a part of the metal as the materials react and undergo corrosion. This indicates visual inspection of the metal surface through optical photon means could provide an avenue for estimating material composition, as each material in the oxidation gradient has been expressed to have differentiable colours present. Using such means would provide a low barrier for entry method in determining whether deposits are valid for later analysis through certain compositional analysis methods.

Table 3.3: Progression of corrosion compounds within 48Y cylinder [30].

Material	Colour
Fe	Metallic
FeF_2	White (Not Seen)
Fe_2F_3 * xH_2O (x=<7)	Gray to Brown
Fe_3 * xH_2O (x=<3)	Whitish to Light Tan
FeF_3 * $3H_2O$ & UF_4 * $0.75H_2O$	Light Violet
UF_4 * $2.5H_2O$	Green
UF_4 * $1.5H_2O$ & UF_4 * $0.75H_2O$	Slightly Darker Green
UO_2F_2 * H_2O	Fluorescent Yellow
$(H_3O)_2(U(OH)_4F_4)$ & UO_2F_2	Yellow
$U_2O_3F_6$	Orange
UOF_4	Bright Orange
UF_6	Clear Solid

Additionally, the temperature in which cylinders are stored at significantly alters the corrosion rates of the material inside, with lowered temperatures correlating heavily with reduced corrosion effects within the cylinder [30]. As such, it is likely that cylinders stored in winter conditions are likely to experience less corrosion within the inside of the cylinder, and are likely to have fewer uranyl fluoride build-up markers on the inner metal surface. Further research could be performed to fully grasp the effects temperature control has on the corrosion rate, and eventual effect on radiation damage to the

metal surface of the cylinders.

The progression of "pure" non-corroded steel cylinder to a fluoride based compound, whether that be ferric fluoride or a compound involving uranium additions, would likely have a significant effect on the crystalline structure, that may be present on the inner surface. As the inner surface continues to undergo corrosion over time, the atomic lattice would undergo significant structural changes, it is expected it would likely lose a large portion of the fingerprint or data associated with defects and interstitials within the lattice. While unconfirmed, it is possible that the radiation fingerprint on the outer surface, regarding calorimetric data would grow significantly once the outer surface of the material had undergone enough corrosion that changes become less frequent. This would allow more time for the damage to grow without disruption or lost information, which would be impacted both by age of the cylinder, and the ambient storage conditions impacting corrosion rate.

3.5. URANIUM HEXAFLUORIDE CHEMICAL PROPERTIES

As discussed in the previous section, the inner surface of the storage cylinders will undergo a corrosion progression over their lifetime as the bare metal alloy is exposed to solid UF_6 held within. Chemical reactions between UF_6 and the steel alloy are expected to be low, leading to an overall low corrosion rate, with the exception of nickel as an added inclusion to the alloy. UF_6 is known to act as an oxidizing agent towards certain metals, with one of such being Ni, which would likely produce NiF_2 and UF_3, and several other fluoride compounds in lower quantities based on the partial pressure in the cylinder [30]. The presence of localized high Ni concentration areas could lead to localized oxidation, causing pitting or removal of material if degradation occurs which could further allow penetration of UF_6. If this was to happen, certain areas may undergo more significant corrosion or pitting as HF_4 is produced, allowing further ingress into the metal surface. This effect could have an impact on expected radiation damage markers, such as penetration depth for α particles based upon incident depth, and electronic stopping power.

The UF_6 being held in a solid state as a colourless, often translucent solid, assists in reducing the overall corrosion rate experienced within the cylinders due to the lower reaction rate between the materials and the lower movement within the UF_6 body [31]. The low reactivity between UF_6 and the metal surface leads to relatively low rates of corrosion, and a layered structure [30]. Formation of such

a structure may be helpful in determining chemical interactions between the two, and the true age of a cylinder given reaction rates are consistent enough for future development. Additionally, the UF_6 is contained in the lower sections of the cylinder with the upper section containing gaseous phase material [31]. This material constitutes the vapour space left within the cylinder to account for both the production of any potential gasses produced during ambient reaction over the life time of the cylinders, as well as the production of additional UF_6 gas, as the material's vapour pressure is volatile [31]. This indicated the potential for multiple radiation damage modes to be present based on the location within the cylinder, the potential for movement or various configurations throughout the cylinder's lifetime, as well as the fill state. As certain locations may only be exposed to solid UF_6, and certain areas exposed to a combination of materials, it is likely that at a minimum, slight changes in chemical properties and reactions will be present between the two areas. Unfortunately due to the available information, it is not possible to identify whether the cylinder sections utilized within this research were exposed to gaseous or solid phase material, or a combination of the two. Future developments with known samples could further identify any differences.

3.6. OVERVIEW OF CHARACTERIZATION METHODS

Identification of any radiation damage markers, or forensics fingerprint left on the surface of the cylinders will rely heavily on analysis methods that can identify trace elements, or microscopic markers present on the surface. This research utilized a number of methods spread across various techniques to identify which had promise for future development. The characterization methods utilized are briefly described below, with an overview of their function, and general use within this research.

3.6.1. SCANNING ELECTRON MICROSCOPY

SEM is a surface characterization microscopy technique that utilizes a focused electron beam to produce images of a sample surface through various interaction means. The voltage, and size of the electron beam can be adjusted to analyse varied spot sizes, and better identify high or low conductance materials. As the method of detection is the scattering and detection of electrons that have interacted with the sample surface, the topography of the sample can have a significant effect on the performance and resolution of the machine [32]. Surfaces with high variance or scattering coefficients can have a

resolution lowering effect as the surface does not cleanly scatter electrons back to the detector from a consistent angle [32]. As such, materials that are less flat, or possibly porous will likely fair much worse than surfaces with a consistent scattering surface.

Commonly, SEMs are run in Secondary Electron (SE) mode, which detects the production of secondary electrons, which are produced after excitation of atoms within the surface undergo de-excitation and emit an electron. A second mode, called Back Scattered Electron (BSE) mode, can also be utilized to get a better look at heavy elements, such as uranium, rare earth metals, or high atomic mass metals. BSE mode measures electrons that undergo elastic scattering, and are scattered or reflected back at the detector after interaction with the surface [32]. Generally BSE mode employs a higher voltage or higher energy electrons to allow scattering to occur without stopping or complete interaction of the electron with the sample surface. Both SE and BSE modes have uses within surface characterization, especially within the area of characterizing heavy metals and uranium based compounds in the forensics field.

3.6.2. ENERGY DISPERSIVE X-RAY SPECTRSOCOPY

EDS is a compositional characterization technique in which the elemental composition of the surface can be analysed through the detection of x-rays released during excitation of atoms [33]. Atoms have a characteristic energy associated with x-rays released after excitation, which can be used to isolate the composition of the surface after consistent application of an excitation source, which is generally a focused electron beam [33]. The composition of the element can be correlated to the intensity of the x-rays absorbed by the detector after excitation of the surface at a uniform, stable rate. The intensity can be utilized to construct a spectra, which correlate to the elemental composition of the surface.

A limitation of EDS is the resolution when dealing with elements of similar x-ray energies. Certain elements may release x-rays in similar enough energies such that isolation of the resultant spectra peaks is difficult or even impossible, leading to obscurity of certain elements within the composition. This effect can lead to certain elements being omitted from results, even when the composition of such is much higher than what would otherwise be the detection limit. EDS provides a valuable non-destructive method of determining elemental composition within the sample surface, and can differentiate between most materials with significant resolution and limits (minimum detection limits generally 0.1%) [33].

It is common to pair an SEM with additional EDS capabilities to improve the capabilities of the two methods in a complimentary fashion. SEM provides an avenue for optical measurements and observation to be made, while EDS can be utilized to further investigate locations of interest through a compositional analysis. The SEM and EDS performed within this work utilized a combination SEM/EDS system.

3.6.3. TRANSMISSION ELECTRON MICROSCOPY

While SEM provided a surface level view of the oxide formation and gives a general idea of the oxide health while identifying potential damage markers, the magnification is not high enough to provide data on the development of meso-scale, or atomic level changes within a material sample. A higher level magnification is required, or a technique that could identify lower compositional impurities or inclusions than previous analysis methods. A higher magnification allows the user to identify grain structure and growth within the material, as well as observe any defect growths in a crystalline lattice. TEM is a microscopy method that utilizes an electron beam to obtain microscopy images at magnifications much higher than SEM or EDS can obtain, with an optimum resolution of roughly 0.2 nm (but is dependent on specific machine capabilities) [34]. TEM differs from other microscopy methods through its use of a number of condensing lenses, which focus the electron beam much more finely than lower magnification machines. These lenses rely on electromagnetic forces that constrict and focus the movement of electrons from the electron gun to fire a very precise beam onto the sample [34]. The electrons from the beam are fired at the sample surface, and transmit through the sample towards a detection device located below, hence the term *transmission electron microscopy* [34]. Due to this mechanism, sample thickness can have a significant effect on the resolution of the produced images, with low resolution images being possible with sample thicknesses of roughly 1 µm, while reducing sample thickness to the order of tens of nm greatly improves output quality [34].

Preparation of samples as thin as those required for TEM generally consists of two methods: use of an FIB to cut samples from the surface utilizing an ion beam, or through a ultramicrotome, which can slice very thin samples [34]. A microtome is more applicable for samples that are softer or more amenable to being sliced such as plastics or biological tissue, whereas FIB is utilized to cut harder materials such as metals or ceramics. Utilizing an ion beam, ions can be focused towards a specific

point on the materail surface to cause localized sputtering and removal of material. This beam can be slowly moved to cut-out a section of the sample material, and produce samples in the sizes required for later TEM analysis.

TEM is generally paired with compositional analysis methods such as variations of EDS or other spectroscopy methods, to both take high magnification images, while simultaneously analysing the composition or elemental makeup of the sample [34]. The two methods together can be utilized to observe a number of applications, with some of those being the development of grains and crystalline structures, alloy distributions and imperfections, as well as defect growths such as dislocation loops [34].

3.6.4. X-RAY PHOTOELECTRON SPECTROSCOPY

Previously described techniques can be utilized to observe and identify the surface of the material, whereas XPS specializes in determining atomic concentration. XPS utilizes x-rays (in this case, a K-α source), to concentrate x-rays on the sample surface which interact with the atoms of surface molecules and cause the photoelectric effect to occur. The atom becomes excited, which leads to the release of an electron with a specific energy related to the binding energy of the elements which is later detected and the energy quantified [35]. The intensity of electrons detected can be correlated to the overall spectrum to produce a compositional analysis or ratio of the surface material. XPS produces clearly defined peaks as the resolution for detection is quite fine, leading to extensive use in material sciences, for determination of specific bindings of elements [35]. XPS measurements are taken within a vacuum chamber to prevent the potential interaction of any x-rays or produced electrons with ambient air which could produce noise or errors within the analysis [36].

The composition of the surface is measured through detection of electrons produced after interaction of the x-rays with elements and bound compounds. The produced photon energies are dependent on the bindings present, as the attraction or electron binding to the nucleus will differ significantly based on the elements [36]. As such, this method provides high resolution to different elemental bindings, allowing differentiation between known compounds or measurements of total compositions through summation of the results.

Additionally, XPS can be utilized with a sputtering device, or auger mechanism such that quanti-

tative measurements can be taken at depths into the surface, providing a profile for the compositional analysis of the sample at depths generally up to 20 nm, which can be used to remove surface contamination that may be present. This value differs significantly based on the material in question, as resistance to sputtering and consistency in surface can alter results.

3.6.5. SECONDARY ION MASS SPECTROMETRY

While XPS identified the binding energies, leading to a elemental compositional analysis, SIMS would provide a compositional analysis through an ion analysis from the sample surface. SIMS, is a technique that utilizes the sputtering of a material surface to produce ions of the sample material. A primary focused ion beam is used to heat and sputter a surface, before the ejected ions produced are collected via a detector, and a mass analysis device utilized. The sputtering of ions releases them from the sample surface, which further exposes atoms located further into the sample. This can lead to inconsistencies within the results as certain elements and materials are more prone to sputtering, leading to inconsistent intensities of detection as certain elements are more readily ionized. To account for the potential inconsistent sputtering, a number of specific calibrations must be utilized for the SIMS machine such that quantifiable results are both possible, and accurate. The specific analysis method utilized within this research was Time of Flight (ToF)-SIMS, in which the subtle mass differences between ions cause a change in the velocity of the sputtered ions towards the mass collector. This, when used in combination with a calibration using well known elements, allows differentiation between singular mass unit differences.

The method of sputtering secondary ions, and utilizing a mass analyser device leads to very high resolutions, and detection limits when analysing with SIMS. Generally, it is noted that SIMS, or MicroSIMS, are the highest accuracy surface composition technique, and can measure elements in the parts per billion range under the correct conditions. For most instruments, the composition of the element must be in the range of 10^{12} and 10^{16} atoms per cubic centimetre to be detectable using the technique.

3.6.6. FLASHDSC

Differential Scanning Calorimetry (DSC) is an analysis technique that measures the effective heat transport or flow into a sample under a specified heating or cooling rate to measure the changes in the material heat capacity over time [37]. This can be used to measure a number of phenomena, including phase changes, annealing of the material, and chemical interactions as the materials interact. By measuring the specific heat flow into the sample, determination of whether a reaction or interaction is exothermic, or endothermic is possible. This can be utilized to further characterize materials and the property changes over a specific temperature range, with accuracy in the mW range [37].

The usage of FlashDSC, a derivative of DSC, reduces the sample mass from the mg range to the ng range, such that microscopic, or meso-scale changes in the material can be quantified. Generally, these changes in the material would otherwise not be measureable with conventional DSC due to detection limitations as other phenomena overpower the resulting peaks or changes in thermal capacity [37]. By reducing the size of the sample, and ensuring good thermal contact with the heating contacts, the sample can be heated at an extremely precise rate, and the accuracy of the energy transport measured to a much higher degree than otherwise possible with conventional DSC instruments. Measuring meso-scale changes in atomic lattice or alloy composition can be completed when outside influences are removed, such as large scale material inconsistencies, or the possibility of atmospheric and slight temperature based “contamination” [37]. FlashDSC instruments also include the use of an interchange supercooler such that the temperature of the thermocouple does not vary, and the specific heating rate can be adhered to, thereby further improving results.

Due to the meso-scale of both the samples utilized for FlashDSC experiments, and the relatively small measurable heat flow changes, the ability to measure atomic changes in the material is almost unparalleled. During the initial heating cycles of FlashDSC samples, the energy released through annealing of the atomic lattice is measurable, inferring the radiation damage within the surface to the energy release through the energy released per defect annealed. This allows non-visible radiation damage to the atomic lattice to be quantified through release of stored lattice energy as the sample is heated, by isolation of DSC peaks in post-experiment analysis.

4

LITERATURE REVIEW

This chapter provides an overview of work reported in the open literature in the fields of materials science and forensics of nuclear materials, and non-proliferation of enriched uranium. Other materials currently being investigated by other groups for nuclear forensics purposes will be described, as well as other materials that have undergone characterization regarding radiation damage investigating damage markers and radiation induced phenomena.

Section 4.1 will identify other materials currently being investigated for nuclear forensics purposes, namely by the Mesoscale Nuclear Materials Group led by Dr. Michael P. Short at MIT and their efforts in determining radiation damage through calorimetric analyses and the stored energy within the atomic lattice.

4.1. NUCLEAR FORENSICS OF NON-STEEL MATERIALS

The Mesoscale Nuclear Materials Group at MIT, which has a focus on investigating nuclear forensics through the characterization of various materials within the enrichment supply chain in the hope of finding methods to correlate radiation damage to the enrichment of uranium that has passed through

the chain. This section describes some of the work performed by members of that group, and elaborates on the concept of enrichment determination through stored energy. A number of materials have previously been investigated, each showing promise for enrichment determination with high accuracy, indicating the methods utilized are likely to be applicable across the supply chain.

4.1.1. POLYMERS

One material of interest within the gas centrifuge enrichment process was the tubing between the centrifuges in a cascade, which is constructed of Polytetrafluoroethylene (PTFE), a material also known as Teflon. This material was selected as it displays plastic-like properties with many favorable for the absorption of radiation damage as visible markers. The material is inherently resistant to fluorination by UF_6 gas due to it being a fluoropolymer [38]. Additionally, the material exhibits low reactivity overall, contains a semi-crystalline structure, and is susceptible to α interactions through it being a polymer based material [38–40]. Extensive research was performed on this material to understand radiation damage with low absorbed doses and provided a threshold in which damage to the material was significant enough for external observation [15]. Measurement of the radiation dose absorbed was thought to be possible through measurement of the stored energy within the crystalline structure of the material or through polymer cross linking [15]. Previous work performed indicated that low doses of ion based radiation absorbed by the material could cause an observable change in the crystallinity of the PTFE material [39, 40]. It was hypothesized that while cross linking and crystalline changes in the material were observed at generally higher doses of α irradiation, the impact on the structure could still be quantified through the use of Fast Scanning Calorimetry (FSC) [15, 39, 40].

The experimental method for the irradiation and subsequent analysis of PTFE samples relied on two pairs of experimental campaigns, with the first being the irradiation of 5 samples to differing enrichment equivalent doses. That being doses that the material would absorb after being exposed to a level of enriched uranium. The results of these experiments indicate significant correlation between predicted absorbed dose, and what was observed utilizing conventional DSC methods. Previous work had the dose multiple magnitudes lower than expected, whereas the results utilizing FSC indicated almost perfect correlation between predicted dose and stored energy release. The second set of experiments being α irradiation of 5 samples to a fluence of 1×10^{11} $[\alpha/cm^2]$ using a colimated mono-

energetic helium ion beam [15]. After which, the samples were sectioned into 32 specimens using a microtome to isolate the outer irradiated sections of the material such that a depth profile could be produced utilizing FSC [15].

From the FSC results, the stored energy release was compared to the simulated α penetration range and intensities to determine whether simulated α irradiation of the sample could both be quantified accurately and whether the resultant fingerprint was similar to that of reference material [15]. The obtained data indicated that it was possible to measure the irradiation of the material accurately and a depth profile produced was similar to that which was expected through simulation based work [15]. Previous literature and the radiation profile produced through simulated radiation was significantly different than that of natural irradiation [15]. While the observable error between results of the work were higher than hoped for radiation penetration depth experiments, it proved that radiation damage signatures within PTFE materials were absolutely measurable and the isotope of origin was able to be determined [15]. Although the results of the work indicated that PTFE exhibited accurate correlations for absorbed radiation dose, the major result was the ability to accurately measure and correlate the absorbed dose to the stored energy, indicating transference of this technique to other materials was quite possible, and could provide fruitful for determining enrichment signatures elsewhere in the supply chain.

4.1.2. METALLIC ALLOYS

A material closer to the interests of this research is irradiated titanium, which was previously investigated in the work by Hirst *et al.* [16] during preliminary experiments identifying whether DSC was a viable technique for correlating the radiation dose to defect propagation throughout the material. It was hypothesized that while metal materials were less receptive than plastic materials to low dose radiation damage or alternative forms of material damage such as excitations as previously discussed, if reconfiguration of the lattice occurred and defects could propagate, the stored energy would be much higher than plastics and other polymer materials. The goal of the work was to validate previous radiation damage simulations and determine if the method posed as a way to perform *a posteriori* radiation analyses, which would support forensic investigations [16]. Previous studies had not utilized analysis methods with a high enough spatial resolution to properly quantify the defects caused by

material damage within metals and the use of a combination of TEM and conventional DSC could answer that question. Initially, sections of CP-2 Ti alloy were taken and neutron irradiated at a temperature of 300 °C to an expected fluence of roughly 6.3×10^{20} $[particles/cm^2]$ [16]. The samples were then annealed using traditional DSC to measure the released stored energy from within the atomic lattice of the material by heating the samples to 1000 °C, which was above the expecting annealing temperature of the material [16]. It is important to note the temperatures utilized for conventional DSC were much higher than would have been possible with FlashDSC due to the contraints of the Mettler-Toledo FlashDSC 1 instrument. The melting temperature of titanium is 1668 °C, which would place the annealing temperature in the 800 °C to 900 °C range, which would be outside of the operating temperatures of a FlashDSC 1 instrument. Conventional DSC of the samples was possible due to the availability of large amounts of irradiated sample, with masses in the mg possible. Use of conventional DSC for α irradiated materials would likely not be possible due to the very thin irradiated outer layer, which would not provide enough testable material.

The results of the work indicated clear differentiable energy releases within the produced curves for irradiated Ti samples, indicating retrieval of the stored damage marker was possible and gave much better results than through traditional TEM methods [16]. Comparison of stored energy release by TEM and DSC techniques indicated stored energy observed through DSC was three times higher than that seen through TEM. This meant that the quantified energy observed through DSC was much higher than TEM, and was able to "observe" data that would otherwise be unavailable [16]. It was also noted that separate energy release functions were observed at varying temperatures. This was confirmed through annealing of the material at various temperatures to investigate the proportion of energy that was released during lower temperature annealing compared to the total stored energy release [16]. The work utilized traditional DSC and proved that it was possible to retrieve radiation damage marker information from larger irradiated samples of metal materials without the use of finer techniques such as micro-DSC or FlashDSC. The two studies discussed laid the foundations for utilizing DSC as a method within nuclear forensics and confirmed the viability of radiation damage extraction from both polymers and metallic materials with both FlashDSC and traditional DSC methods.

4.2. CHARACTERIZATION OF MATERIALS

While this thesis is specific to steels, a plethora of other materials have been investigated to determine the effects of radiation on various materials forms, whether that be ceramics, plastics, or other non-organic materials. The information gained through these studies paints the picture of how steels absorb and display radiation damage, and formed the initial directions to explore for the work performed. Identifying radiation induced phenomena ensures any potential damage markers observed through surface characterization could be identified during analysis. The quantification of dislocation loops has previously been proven to be an acceptable measure for absorbed radiation in metallic materials, and could provide an avenue for the correlation or uranium enrichment through TEM analysis.

A number of materials have had their radiation damage profiles characterized through quantification and analysis of dislocation loop formation after irradiation to set Dislocations Per Atom (DPA) amounts. Some of these materials include alloys used for common reactor materials such as Zr alloys [41–43] and carbon steels [22, 41, 44], or other materials such as ceramics [20], glasses [45] and other metals [23, 41, 46, 47]. Many of these studies investigated radiation damage caused by other forms or radiation such as neutron or gamma radiation, as well as various high energy, high mass ions. These materials, while not being directly comparable to the 48Y cylinders utilized, should undergo similar processes after absorbing significant radiation doses, and provide an indication on the experimental methodologies utilized, and which analysis methods have promise.

4.2.1. DISLOCATION LOOPS AND DEFECT PROPAGATION

Dislocation loops are formed through the propagation of defects in the lattice caused by radiation interactions with the atoms should be an identifiable phenomena within bulk metals, or organized materials. Quantifying dislocation loops begins with the artificial propagation of defects throughout the material to grow the size and quantity of dislocation loops. In regards to nuclear research, this is done through irradiation of the material through an artificial irradiator, such as an α, γ or neutron source. In work by Yao *et al.* [44], bcc structure reduced activation ferritic/martensitic steel was irradiated with a neutron source at 400 °C using the High Flux Isotope Reactor at the Oak Ridge National Laboratory to an He/DPA ratio of roughly 23 [44], which indicates the atomic defects per implanted α (helium) atom.

The work was done to investigate the effects of He implantation caused by neutron interactions with the NiAl layer deposited on the outer surface of the samples. From those experiments, it was noted that significant growth in the (100)(200) and 1/2(111)(111) dislocation loops was observed with the density of (100) loops observed to be much higher than 1/2(111) [44]. This indicated significant growth in the number of dislocation loops observed in the metal alloy, confirming the formation of loops should be quantifiable under 48Y conditions if the presence of a crystalline metal material is confirmed.

4.2.2. OTHER CHARACTERIZATION TECHNIQUES

In a study by Yu *et al.* [48], stainless steel 316L was bombarded with α particles and neutrons to simulate fusion conditions and investigate material performance in a future assembly. The TRIM code was utilized to simulate the effects beforehand, before the samples were irradiated with α and neutrons (1.8 MeV and 1.5 MeV respectively) to a DPA of 50 [48]. From those results, it was determined that a significant peak in helium bubble diameter was present within the sample as the particles came to rest within the surface [48]. The peak was observed at a depth of roughly 2.5 µm as helium bubble diameter was at a max of 20 nm [48]. The density of bubbles within the surface was also verified, in which it was observed that annealing or cold working of the material had a significant effect on the formation of bubbles. Cold worked steel retained far fewer bubbles than solution annealed steel, and had a higher concentration of bubbles at lower depths, whereas the solution annealed steel had a higher density, concentrated at higher depths [48]. The much lower energy of the α particles indicated penetration into the sample would be much lower than through uranium decay. The results concluded that helium bubble formation should be a viable method of quantifying α radiation damage through compositional analyses of a cross sectional view of the surface [48].

While not directly quantification of radiation damage, the work by Daub *et al.* [22] investigated the effects of γ radiation on the corrosion rate exhibited by carbon steel within aqueous environments. It was shown that irradiating carbon steel coupons using a ^{60}Co irradiator with a fluence of 6.2 kGy/h for a period of 20 h or 66 h, the observed corrosion rate of the steel within the aqueous medium significantly affected the corrosion rates of the metal and impacted the compounds present within the surface [22]. The study utilized SEM for observation and RAMAN spectroscopy to identify the Raman shift parameters observed after irradiation and corrosion of the coupons to identify any significant changes

between experiments at varying pH levels and temperatures. From that study, it was also noted that temperature dependence of corrosion played a significant part in the observed rates, supporting evidence that corrosion withing 48Y cylinders would rely heavily on ambient storage conditions [22, 31].

Later work by Aljohani *et al.* [49] investigated a similar phenomena in which carbon steel was exposed to high doses of γ radiation within a sodium-chorlide electrolytic environment to investigate the effects of radiation on observed corrosion rate to support future use of the material as a long term storage material. Small carbon steel coupons were used with a ^{60}Co irradiator, much like the previous study but three dose points were utilized: 70 kGy, 150 kGy and 250 kGy [49]. After irradiation, the coupons were analysed utilizing SEM, EDS, X-ray fluorescence and X-ray diffraction to identify the effect of γ irradiation on the corrosion mechanisms. It was observed that the potential energy for the system was greatly increased after γ irradiation, as well as the X-ray diffraction patterns indicating much higher intensities. These results indicated an increased presence of dislocations and defects within the crystalline structure of the material, with an expected linear interpolation visible between irradiation doses [49].

Both previous studies utilized a carbon steel similar in composition to the material from which 48Y cylinders are manufactured, indicating the potential for non-α radiation sources to cause alterations to the corrosion mechanics inside the cylinders. While the studies utilized γ radiation, significant damage profiles were observed even in hard carbon based steels. Neither study looked into the characterization of dislocation loops within the corroded material and did not utilize a technique with high enough spatial resolution to identify whether dislocation loops were forming due to the radiation damage incurred.

4.3. OVERVIEW ON LITERATURE METHODS

While a variety of methods were utilized to categorize and investigate radiation based damage within multiple types of materials, to quantify the results in a manner that isolates specifically the damage caused by unknown radiation sources, the macroscopic analysis methods such as SEM and low-resolution EDS can be removed from contention. While a number of studies utilized the methods, the results were not accurate enough to discern radiation damage in the levels required to differentiate ^{235}U damage from that caused by ^{238}U. A number of studies showed promise in analysing micro-

scopic levels of radiation damage, such as through quantification of the location and density of He bubbles in Yu *et al.* [48], as well as the investigation of unit dislocation loops in ferritic steels by Yao *et al.* [44]. While the work by Aljohani *et al.* [49] and Daub *et al.* [22] were investigating wider areas of radiation damage corresponding to corrosion, the use of XRD and RAMAN spectroscopy to confirm microscopic changes in the composition was supported. It was confirmed these techniques could be to determine crystalline structure changes and the compositional differences, and be used in parallel to the techniques discussed previously to confirm radiation damage after the annealing stages of FlashDSC. While results indicate the potential for chemical interactions, utilizing a confirmatory technique to remove phase transitions from the equation using a pre and post annealing analysis would further improve confidence.

The most favorable results were shown by Connick *et al.* [15] and Hirst *et al.*, [16] in which HEU damage signatures were able to be differentiated from lower enrichment radiation damage amounts through micro calorimetric means such as the use of FlashDSC and confirmatory TEM analysis had the highest confidence intervals for the purposes stated. The methods were able to differentiate the radiation damage in both a polymer based material, which was expected to better absorb damage signatures, but also a metal based material, increasing confidence in the potential use of 48Y cylinder sections [15, 16].

5

METHODOLOGY

This chapter provides a description of the various experimental methodologies used for sample preparation and analysis of this research. The project involved steel materials donated by Cameco Corporation in the form of 48Y cylinder samples which were sectioned at Ontario Tech and prepared for subsequent analyses.

This chapter will provide an overview of the methodologies for preparation and sectioning of the samples from as-received material to analysis ready sizes, as well as the overall analysis procedures used to calculate and provide final results for each of the methods. Sections 5.1 and 5.2 overview the initial sample sectioning from the as-received forms, followed by Section 5.3 which details procedures for each specific analysis method. The overall experimental analysis procedures, and data analysis steps are described in Sections 5.5 and 5.6 respectively.

5.1. AS-RECEIVED MATERIALS

Steel A516 cylinders (48Y cylinder), of grade 65 or 70 were donated by Cameco Corporation in the form of 12” to 18” square sections, of roughly 3/4” thickness, as seen in Figure 5.4. Smaller samples were

received, being sized at roughly 2" to 3", but were determined to be too small to isolate material from the outer edges damaged during the initial plasma cutting by Cameco Corporation. These cylinders were used to hold UF_6 during the conversion process for enriched fuels for use in non-Canadian reactors. The cylinders have been used for a period of 44 years, in which cumulative radiation would have influenced the steel surface. Along with the extensive time of use, ambient moisture from the UF_6 would interact with the steel and a corrosion deposition layer will have formed. This oxide or fluoride layer would likely contain a forensic fingerprint caused by radiation, mainly in the form of α particles, produced through decay of the UF_6 throughout its lifetime usage.

5.2. GENERAL SAMPLE PREPARATION

5.2.1. SAFETY WHILE SECTIONING SAMPLES FROM CYLINDERS

Due to the sample surface containing trace amounts of uranium and fluorine based compounds, a Standard Operating Procedure (SOP) was developed to ensure safety during the sample preparation and analysis portions of the research. While very low in amount, alpha and beta radiation producing isotopes were present, indicating accidental inhalation or consumption of any sample material would be hazardous to the health of individuals working with, or nearby the samples. Additionally, the high chemical reactivity of fluorine led to the need for additional reaction tests to be completed to ensure materials in contact with the surface during sample preparation did not lead to the production of hazardous materials, or reaction on the surface leading to sample damage.

To ensure safety during preparation of the samples, precautionary Personal Protective Equipment (PPE) was worn at all times when contact with the samples was required. The major hazards associated with the samples included inhalation of radioisotopes or oxide material, hearing damage when operating machinery, and potential projectiles causing harm to the operators. As such, at all times the operator of the machine required a fit certified N95 mask to be worn (certified through Maskfit Plus), safety glasses, and hearing protection rated to the expected level of danger. Additionally, nitrile gloves were worn during handling both for protection from surface material, and to prevent contamination of the surface from any material or oil present on the hands of the operators. To prevent projectiles, the steel was fastened to the stage using 4 adjustable C-clamps to both prevent the sample from falling

off and to reduce vibration during cutting. Additionally, a deep-set McMaster-Carr 3" hole saw bit was utilized to hold the inner cut piece inside to prevent it from flying off of the drill press after it had been released. An auger bit was selected to provide additional support, while causing minimal damage to the inner sample surface. Additionally, all cutting procedures were performed with the assistance of an experienced technician to both assure the safety of all operating personnel, and to prevent any damage to the samples.

Before and after every preparation step, the area around the machine was cleaned of any debris, and a radiation scan performed to determine the background radiation of the area for comparison after operation. To ensure any possible radiation contamination was kept contained, a radiation scan was performed to determine if any observable increase was noted, on which cleaning operations were performed if an increase was determined. The radiation scans completed on the full samples, samples after cutting, and final sectioned samples can be seen in Table 5.1. In the case of the increase being less than three times the background radiation amount, the area could be cleaned and decontaminated, but if the increase was greater than three times background, the Radiation Safety Officer was required to be notified, and an official decontamination procedure begun. To reduce the likelihood of the spread of material, a magnetic sweeper was used to pick up any metal shavings or particulates that may have been spread, along with the collection of any machining oil to a central container which could be radiation monitored all at once. Once the cutting had been completed, a scan of the debris was performed, and safe disposal of all garbage and waste material completed. Throughout the sample preparation stages, there were no radiation contamination incidents as the use of the safety precautions outlined in this section were used, as well as the radiation contained on the sample was minimal.

Calculations were performed to measure the safety impact of the radiation from the samples for both personnel safety reasons, and for export regulations while sending samples for analysis at other institutions. From the calculations, it was determined that the radiation was well below exemption limits according to regulatory guidelines, and was within safe limits for the purposes of this research. While precautions were to be taken during preparation and analyses, the radiation contained within the samples was not a source of hazard under normal conditions, as long as safety precautions were followed.

Table 5.1: Radiation scans of the steel samples for both α and β radiation, in counts per second.

Radiation Type	Full Sections	3” Cutouts	Final Sample	Background
α	0.45	0.3	0.1	0
β	4.1	1.3	0.5	1.6
α and β	4.5	1.5	0.6	1.6

5.2.2. PREPARATION PROCEDURES

The steel cylinder sections received were initially far too large to prepare for analysis with the precision required with the tools available and as such, additional sample preparation methods were required. For the steel to be cut within the institution, they required significant down-sizing before precise cuts could be made using a precision cutter. The required size for the precision cutter available was in the range of roughly 10 cm pieces, with the thickness being in an acceptable range. The cutter utilized could theoretically accept a longer sample than this width, but due to limitations with cutting the steel it was likely that a square or circular sample would best fit the circumstances. To prepare the steel cylinders for sectioning in the precision cutter, a number of methods were considered before the use of a hole saw and drill press were selected to produce 3" circular cut outs of the cylinder, as shown in Figure 5.1. These smaller samples could then be sectioned using a precision cutter as to not damage the micro-structure of the steel, or the fragile forensic fingerprint that was to be investigated.

Once the method had been selected, before any work on the full samples was done, a test was completed on a non-radioactive sample that had been sandblasted prior to arrival. This was done to test both the hardness of the material, and confirm the cutting methods utilized would not damage the surface of the sample through over-heating or wearing of the surface. The test sample shown in Figure 5.2 was initially cut on a different small drill press (as seen in Figure 5.3(a)) and multi-use hole saw bit, where it was noted that a much more powerful press would be required (as seen in Figure 5.3(b)). Additionally, it was noted that the multi-use cutting bit that was tested would not be adequate, and a specialty bit specifically designed for cutting steels would be needed to prevent damage or blowout. Due to the low drill press power and ineffective hole saw bit, the cutting was stopped after a period of 1.5 h as it was decided that enough information had been gathered and full cutting of the sample would not be beneficial.

Initial sectioning was performed using a RIGID DP15501 drill press, along with a 3" diameter,

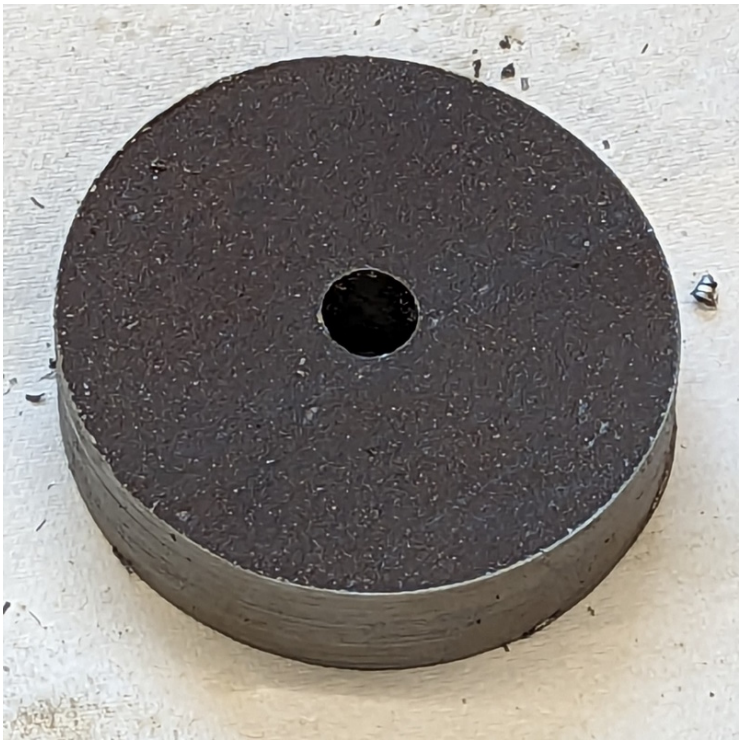

Figure 5.1: Image of samples after being sectioned using the hole saw and drill press. Circular cutouts were 3” in diameter.

2" depth, circular hole saw bit with included pilot drill bit from McMaster-Carr. These bits ensured a relatively clean cut with minimal vibration to reduce damage to the sample surface. Additionally, generic machining oil was used, which was applied regularly to cool the sample surface, remove debris from the cutting hole, prevent burning while cutting, and ensure any produced powder was sequestered as to not become a radiation inhalation hazard. During cutting, the sample was secured using 4 C-clamps, with each located on a corner of the steel to reduce vibration and ensure the sample isn’t dislodged during cutting, both becoming a health hazard, and damaging the bit or surface. Cutting of the sample progressed slowly, as to prevent overheating, and intermittent breaks were taken to allow the drill press motor, and sample to cool adequately. All stages of the cutting process were performed with, and supervised by an experience technician. The location of circular cut outs from plate 7A can be seen in Figure 5.4, where two cut outs were taken.

After each round was cut with a large drill press, the sample was blotted to remove excess machining oil before being placed in a sample container and left to air dry for a period before additional sectioning could occur. Additionally, it was placed in a closed zip-lock bag to reduce dust or air con-

Figure 5.2: Photograph of small sand blasted sample after test cuts were made. The sample was difficult to cut through, and was stopped after it was decided high power equipment was required.

tamination of the surface during holding periods. Visual checks were performed with each sample to identify if any significant surface damage was incurred during the initial cutting measures, as if any were identified, the sample would be removed from contention to ensure sample health was in good standing.

For further sectioning of the samples into analysis ready sizes, a Metkon Metacut M250 precision cutter (As seen in Figure 5.5) was used that could accommodate both cutting the steel material without damaging the micro-structure, and the small constraints of the final sample required. While the outer edges of the circular cut outs likely underwent heating due to the friction from the drill bit, the use of coolant during operation, and the low speed utilized should have minimized the damage into the sample. This would preserve the inner material of the samples, and ensure the micro-structure stayed healthy. The precision cutter used abrasive cut-off blades purposed for cutting hard steels or other hard ceramics materials. Additional Metkon Metcool machining fluid was used to prevent material build-up during cutting, cool the cutting apparatus, and ensure no airborne powders were produced. While the precision cutter had an enclosed space which further reduced the potential for spreading

(a) Smaller drill press initially used for test cuts.

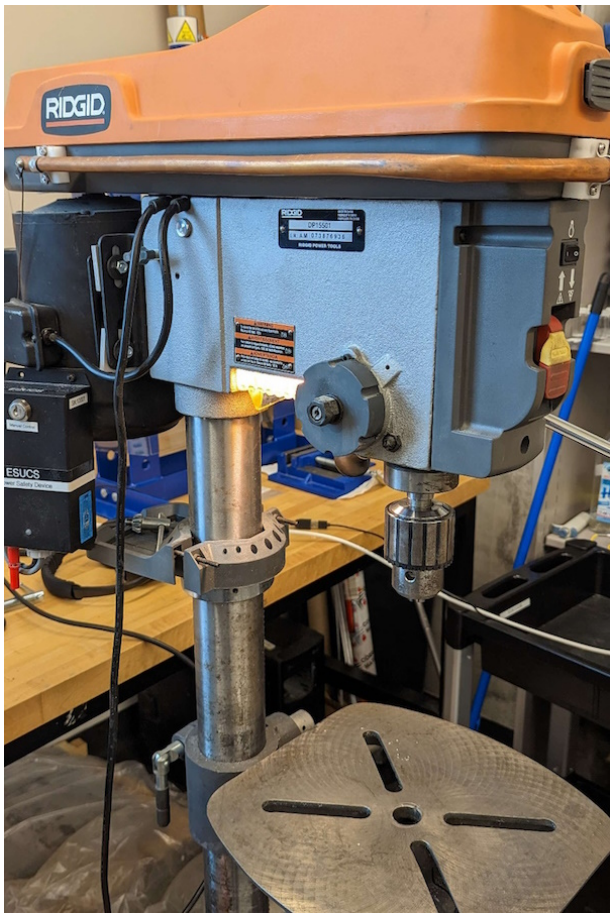

(b) Larger RIGID drill press used for cutting of samples.

Figure 5.3: Photographs of drill presses used for this work.

Figure 5.4: Photograph of full sample as received from Cameco Corporation with two cut out holes. Four plates were received, two large (18" x 18"), and two small (12" x 12").

dust or powders, the use of a fluid further reduced any risks. To secure the sample during cutting, Metkon C-clamps held the sample from either side of the cutting location. This prevented potential damage through vibration of the sample, and allowed clamping without touching the sample surface. Before and after each cut, a radiation scan was completed to ensure no contamination of the area occurred and the precision cutter was cleaned thoroughly afterwards to remove any particulates. During cutting, the abrasive wheel of the precision cutter was moved very slowly to prevent excessive heat buildup through abrasion. After the first cuts, the temperature of the samples was checked using an infra-red temperature monitor, in which the cut surface of the samples was measured below 80 °C. However the measurement was not instant, and cooling fluid would have reduced the temperature before readings could be accurately taken. While the cut could not be stopped during intermediate stages as to prevent damage or vibration of the blade causing blowout, care was taken to follow correct operational guidelines as per vendor recommendations to prevent any damage to the sample itself. The final sample after sectioning within the precision cutter can be seen in Figure 5.6.

A consideration during preparation of the samples was potentially damaging the microstructure of the steel or removing some of the material held on the outer surface of the steel due to vibration or localized heating. As the material was quite tough to cut, it was likely that the metal would get hot if

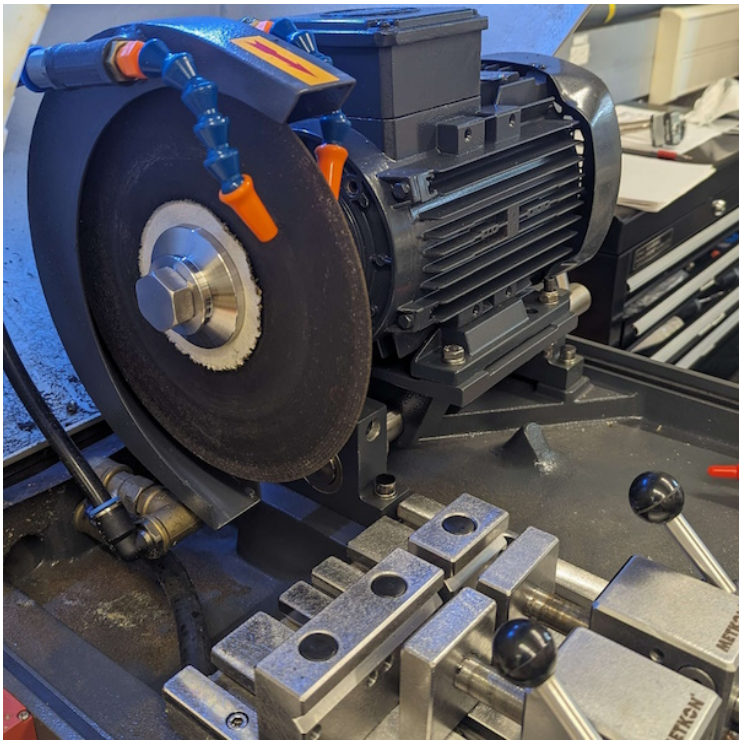

Figure 5.5: Photograph of the Metkon Metacut M250 precision cutter used for the sectioning within this work.

Figure 5.6: Image of sectioned sample, ready for ultrasonic cleaning. Field of view is approximately 2 cm.

continued operation was held, and was likely that some damage to the surface would occur. To prevent this from happening, adequate machining oil was used at all times during cutting operations to remove heat from the cutting surface, as well as stopping cutting operations for a period to let the sample cool off periodically. These precautions helped ensure the surface remained semi-cool, or below a point that would cause significant damage to the sample. Additionally, during final sectioning using the precision cutter, it was made sure that any final samples were located away from the outer edges of the circular cutouts, and were taken from an inside area, as to further isolate any potential heat based damage effects.

The final step before the samples were ready for initial analyses was the cleaning of the samples using a Vevor Ultrasonic Cleaner (seen in Figure 5.7) in which the samples were cleaned for a period of 15 min at 40 °C in an ethanol bath. The time period was selected to allow particulates to be cleaned from the surface of the samples, while limiting the run time to prevent causing excessive damage to the oxide layer, or other features of the surface. It was likely that any loose particulates would be removed during cleaning, but to prevent the excess removal of more stable oxides, the time was reduced. After cleaning, the solution was noted to have minimal to no discolouration, or particulates removed from the surface indicating little damage had been caused by the process. After cleaning, the samples were left to air-dry for a minimum period of 24 h before the analysis would proceed. The final sample, ready for analysis can be seen in Figure 5.8. The samples produced using these steps were used for SEM, EDS, and XPS analyses but additional preparation steps were required for further analysis which are described in the following sub-sections.

5.2.3. WATER VS. ETHANOL SAMPLE CLEANING

During the analysis, literature regarding uranium-fluoride compound build-ups in 48Y cylinders was discovered [30, 31], largely explaining the material buildup on the outer layers and chemical properties of the materials on the surface of the cylinders. Based on the reports, it was believed that uranyl fluoride compounds were present on the surface in surface deposit form. This was coherent with initial SEM results obtained, which will be discussed in Chapter 6. It was found that fluoride compounds are extremely soluble in water, with little to no solubility in alcohol or ethanol based solutions [30]. An additional sample was prepared utilizing an ultrasonic cleaning period in de-ionized water. The cleaning

Figure 5.7: Photograph of Vevor Ultrasonic Cleaner used in this work for sample cleaning.

operation was performed at 40 °C for a period of 15 min. After cleaning, the sample was left to air-dry for a period of 24 h before use. A number of additional samples were cleaned this way to be compared to the ethanol cleaned samples. While the samples would have been exposed to water during the sample preparation stages, as the coolants were diluted with water, the ultrasonic vibrations, and heightened temperatures increased the dissolution of the surface, allowing the deposit to be removed.

After cleaning of the sample, once the sample had been placed back within the sample bag, it was noticed that a contaminant spot was identified within the bag. It was possible that this contaminant was the dissolved uranyl fluoride compounds from the surface which had been removed, and come together on top of the water surface, being picked up by the sample when removed. The contaminant had adhered to the sample bag as seen in Figure 5.9, and was dry enough such that isolation or air contamination of the sample was deemed not a risk. The sample bag was then isolated and the contaminant section removed with a knife such that the sample could be further identified. Additionally, after any testing, the sample had tape placed over the surface to further reduce any possible radiation contamination concerns, such that particles could not be aerosolized or further removed from

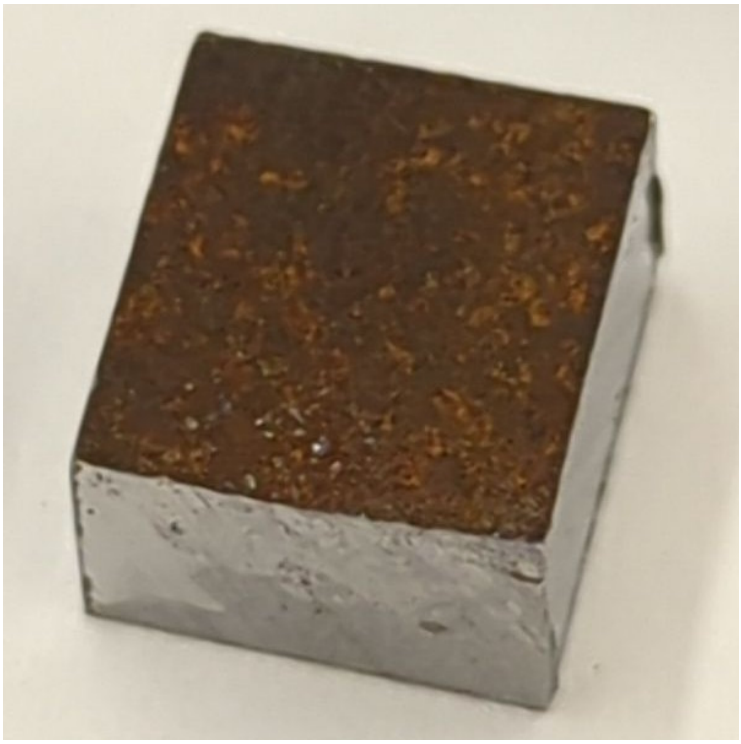

Figure 5.8: Image of final sample, ready for analysis. Final dimensions of analysis sample were 1 cm x 1 cm x 0.5 cm.

the surface.

It should be noted that both washing methods underwent an ethanol wash for analysed samples, due to the initial washing to remove machining oils from the preparation stages. As the samples were initially all cleaned with ethanol, before the uranyl fluorides were discovered, the water washed sample underwent a secondary cleaning which identified the deposits on the surface. At the time, the effects were expected to be negligible due to the solubility of fluorides in water, however it was identified that certain uranyl fluorides, specifically UO_2F_2 are susceptible to dissolution in water. Due to the solubility, it is possible that any uranium bearing compounds dissolved in the initial ethanol wash, before the other fluorides were exposed to, and dissolved in the water wash.

5.3. SPECIALIZED PREPARATION FOR ANALYSIS METHODS

5.3.1. TEM PREPARATION USING FIB

To prepare samples for TEM analysis, the size of the samples had to be massively reduced to the 100 nm range, to allow electron transmission through the samples. A Hitachi Dual-beam FIB-SEM NB5000 in-

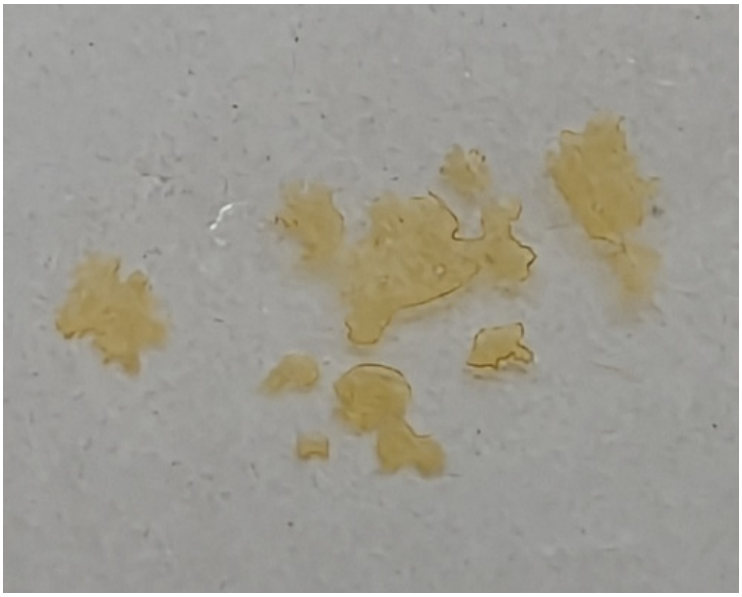

Figure 5.9: Image of dissolved material after cleaning within de-ionized water.

strument was utilized to section the samples for further analysis. The instrument utilizes a focused Ga ion, and e-beam system to cut small sample sections out from the surface. The beam has a max power of 50 nA, with a current of 40 kV, which allows precision cutting of the surface during SEM analysis and observation of the cutting area. After the samples have been sectioned, the instrument allows easy transportation to the TEM analysis instrument through a side-enclosed TEM stage. Use of the FIB allows removal of sample material, and sectioning of samples to be analysed in the TEM on the sub-µm range.

The samples prepared for TEM included one sample from the water washed sample and one control sample from an inner cut side untouched by UF_6. This allowed a control count for dislocations to be taken, while comparing the two surfaces of the washed samples. Each of the samples was prepared to be 6 µm x 6 µm in across, with a thickness in the 100 nm range.

5.3.2. ToF-SIMS Addition

In addition to TEM analysis, ToF-SIMS was utilized as an addition to the analysis methods performed at UofT, and provided compositional data for the sample surface. The usage of SIMS included additional samples to be utilized to provide results due to the difference in analytical setups. With the limitation of SIMS depth (maximum depth being roughly 20 to 30 Å, or 0.2 nm to 0.3 nm), a side-cut sample was

utilized in addition to the previous samples such that depth could be measured through the surface, instead of sputtering due to the high depths requested. Samples were initially prepared at Ontario Tech University and sent to UofT where the work was performed.

5.3.3. FLASHDSC PREPARATION

To prepare samples for FlashDSC analysis, a total of four cylinder sections were brought to the Mesoscale Nuclear Material Group's laboratory at MIT where both the preparation and analyses were performed during a stay at the campus in June 2023. Initially, the samples were checked for any damage during transportation before identifying regions in which small oxide pieces could be sectioned away. The oxide was then observed to identify regions of the surface that were of good health, and had oxide that was fully formed without prior scratches. A new razor blade was then used to scrape the surface of the oxide to remove particles that were placed on a glass slide for isolation, to be later picked up and transported to the FlashDSC machine. If particle sizes were too large for use, they were further broken up using the razor blade while reducing the particle size for pickup. During this process it was ensured that no material from the razor blade contaminated the sample as the colour of the particulates were carefully examined.

5.4. EXPERIMENTAL MATRIX

From the four large steel sections donated by Cameco Corporation, it was decided that utilizing two sections to produce samples would provide enough consistency in the results to draw conclusions while ensuring enough separation between locations. From these two sections, a total of four circular cutouts were taken, each from a separate area of the two sections. From these cutouts, an experimental matrix was created to identify which samples would be used for ensuring data spread between the sections, while providing enough samples to confirm consistency in results. The experimental matrix for this work is given in Table 5.2. A total of eight samples were prepared, of which four were utilized for surface characterization, one sample initially used at MIT, and two samples for work at UofT.

Table 5.2: Experimental Matrix

Sample Identifier	Analysis at OTU	Analysis at UofT	Analysis at MIT
A1-1	SEM, EDS, XPS	SIMS, TEM	FlashDSC
A1-2	SEM, EDS		
A2-1	SEM, EDS, XPS		
A2-2	SEM, EDS	SIMS, TEM	
B1-1	SEM, EDS, XPS		
B1-2	SEM, EDS		
B2-1	SEM, EDS		
B2-2	SEM, EDS, XPS		

5.5. ANALYSIS PROCEDURES

5.5.1. SEM & EDS

SEM and EDS analyses were performed within the Materials Characterization facility at Ontario Tech University using a Hitachi FlexSEM 1000 Scanning Electron Microscope coupled with a Peltier-cooled Energy Dispersive X-Ray Detector, in which each sample was observed for notable radiation damage markers and the overall condition and buildup of the corrosion deposition layer on the outer sample surface. For each sample, a number of images were taken, with magnifications ranging from 100x to 5000x to identify significant features or phenomena that occurred that indicated radiation affecting the micro, or macro-structure of the sample. Due to the samples being magnetic in nature, the height of the detector was increased from 5 mm to 10 mm to prevent loose particulates from being attracted to the detector device and potentially causing damage. Once a feature had been identified, an additional spot EDS analysis was completed to determine any compositional artifacts or gradients that may be present. For smaller defects, an area analysis was performed to save analysis time and provide a higher resolution specified area. During EDS analyses, common steel inclusions were tracked, as well as any potential elements from the UF_6 interactions such as uranium, fluorine or other actinides.

During EDS analyses, determining the presence of fluorine was difficult due to the functional areas of F and Fe within the EDS spectrum. With the high composition of Fe in the surface, the peak associated with it was significantly higher than F, and could have overshadowed any presence of F due to their close locations. It is unlikely that EDS could be used to reliably quantify fluorine concentrations within the samples with iron present. A number of common contaminations were removed during EDS analyses due to their low value within the results. After confirmation that elements such as C,

Si, and N were very unlikely to be anything significant within the results, the compositions were removed from analyses afterwards to prevent data crowding within the images, such that the valuable information could be left isolated.

5.5.2. XPS

The compositional analyses performed utilizing XPS were performed with a Nexsa ThermoScientific System that allowed XPS, Auger Electron Spectroscopy and Reflected Electron Energy Loss Spectroscopy to be performed within one instrument. The analysis system utilized a monochromated, low power Al K-Alpha X-ray source to collect compositional data from each of the samples with a spot size of 400 µm. The analysis period for each sample was increased to allow the potential observation of lower inclusion elements and bindings, and ensure the results would report consistent results between plate pieces.

It was determined that the possible depth of performing Auger Spectroscopy on the sample was not deep enough to provide valuable results regarding radiation damage, and would only provide results of the contamination of the outer surface, which was deemed not significant enough. Due to A516 steel's inherent material composition, sputtering of the surface would likely have led to inconsistent removal of material, and non-accurate depth profiles produced. As such, it was removed from consideration of XPS results early in the process.

In the process of observing actinide compositions within the samples, XPS analysis was utilized as a first choice. Due to data availability and machine constraints, the binding energy ranges for the actinide compounds had to be observed through widened observation ranges of nearby known elements. From Krause *et al.* [50], it was indicated that binding energies for Th and Pa would be located around the known binding energies for Ca, and Ca compounds (345 eV - 348 eV). While the binding energies for certain Th and Pa compounds were known, the exact elements bound were likely to be different leading to an approximation of the area being used to determine their presence. Due to how XPS functions, the difference in isotopes and bound elements would lead to minor differences in final binding energy in the results, indicating exact determination would be difficult through XPS. Due to the limitations of the XPS machine, the search range for Ca was extended to both sides to include the potential binding energies for the actinides expected.

5.5.3. ToF-SIMS

ToF-SIMS was performed within the Open Centre for the Characterization of Advanced Materials (OCCAM) at UofT, where an IONTOF TOFSIMS 5 instrument was utilized. The instrument uses a 0.3 pA Bi3 primary ion source at 30 keV to remove molecules and isotopes from the outer surface of the sample with a spatial resolution greater than 300 nm. Each measurement was taken over a 500 µm or 250 µm area. The cycle time between the sputtering and collection for the measurements was 100 µs. After sputtering of the surface, a polarity was applied to the surface to attract charged particles to the Reflectron ToF mass analyzer. Both a negative and positive polarity were applied to collect particles of both charges. Due to the consistent applied polarity, an initial kinetic energy is applied to the particles, wherein the mass differences cause a difference in velocity, and therefore a higher Time of Flight (ToF) depending on atomic mass. As the velocity changes, the atomic masses of the particles can be differentiated, and the number of particles counted at a certain time step can be binned to apply an expected mass/charge ratio to determine the composition of the particles in question. Resolution of the instrument allows differentiation between particles that are generally considered to be the same mass, down to decimal points, due to the specific time taken to travel to the detector. The isolation of height effects can be used to increase accuracy and confidence in the results as removal of low or high areas can reduce uncertainty in particle travel time due to initial delta height differences across the sample surface.

5.5.4. TEM

TEM analysis was completed using a Hitachi CFE-TEM HF3300 instrument, which was capable of performing 300 kV FE-TEM. The instrument produced an electon beam, aimed through the top of the sectioned sample surface, before being captured by a detection instrument. For each of the samples, a number of images were taken identifying the presence of dislocation loops, defects, and overlapping grain structures, allowing qualitative assessments of radiation based damage to be made. The location analysed was centred on the boundary between the underlying metal, and the deposition layer on the outer surface, with an image of the boundary seen in Figure 5.10. From the boundary point, all analyses and images were taken at a maximum distance of 100 nm into the material. This would have placed the analyses well within the expected 20 µm penetration depth of the α particles from the UF_6

material.

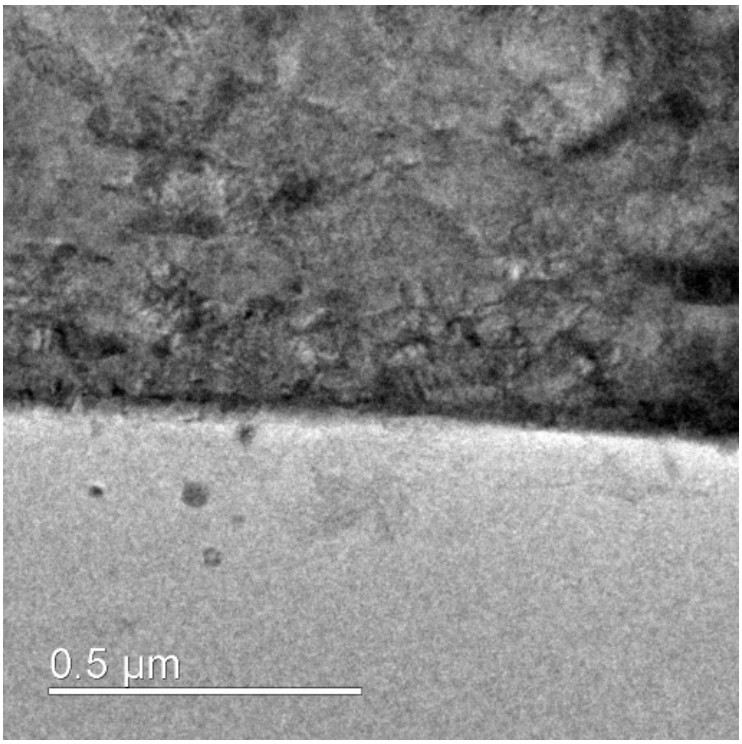

Figure 5.10: TEM image of boundary between bare metal and deposit interface. Deposit material was seen on the lower half of the image, and metal on the upper half.

5.5.5. FLASHDSC

To prepare for experimentation, the sample particles were transferred to a FlashDSC microchip (as seen in Figure 5.11) while ensuring that the material stayed within the central area of the chip. The microchip contains a number of heating elements and thermocouples on the outer edges that heat and measure the heat flow into the sample during experimentation. For proper measurements to be taken, it was vital that the sample did not lay on an area other than the central pad, which is visible in Figure 5.12, showing the sample was contained within the centre area of the chip. This area ensures solid thermal contact with the material, and the plating increases the thermal conductivity such that accurate measurements can be taken as heat flow into the sample should not be limited. Transportation of the sample from the glass slide to the microchip was performed using a human eyelash in combination with electrostatic forces due to the microscopic scale of the samples. Any other transportation method either would not work, or would crush the sample during attempts to move it. It is estimated that the

final mass of each sample utilized for FlashDSC was in the 1 µg range.

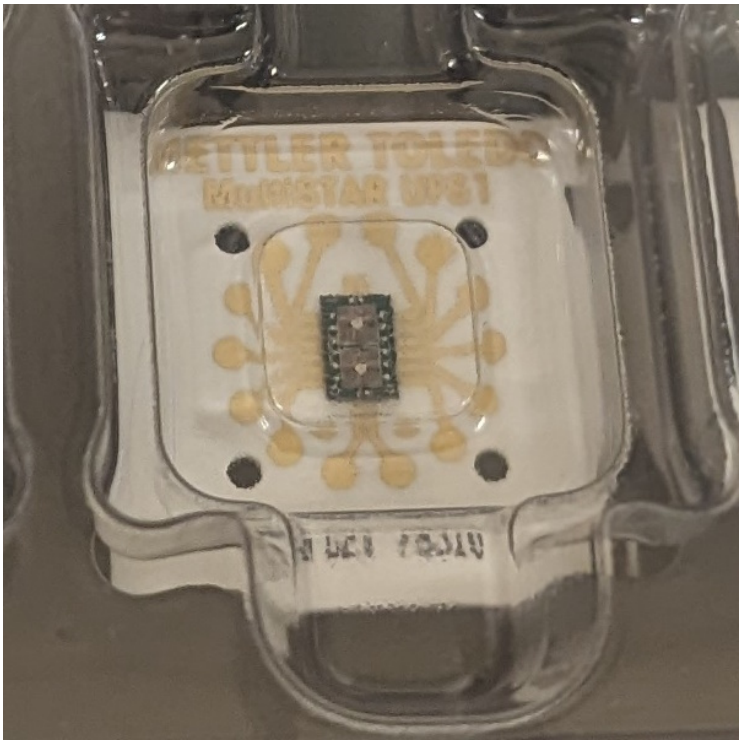

Figure 5.11: Photograph of full UFS 1 microchip used for FlashDSC experimentation, produced by Mettler-Toledo.

The samples were added to the centre of the microchip, such that material stayed within the bounds of the chip contacts and away from external heating or sensing instrumentation. The material was transferred using an eyelash in combination with electrostatic forces due to the extremely small nature of the samples. In total, it is estimated a maximum of 1 µg of material was utilized for the experiments.

A standard UFS 1 Chip for use up to 500 °C was conditioned for experimentation in the FlashDSC instrument at MIT before the sample could be set on the chip. Chip sets for the FlashDSC are produced in sets of 10 with identifiers given by the manufacturer for each chip such that a specific conditioning program could be run within the flashDSC to remove any internal stresses created during manufacturing or transportation. A series of 5 conditioning runs were completed before the sample could be added. To prepare the machine for experimentation, the super-cooler was activated, and ample time waited to bring the machine to a stable temperature of 25 °C. At the same time, the argon protective gasses were initiated to protect the mass-balance within the machine from flash freezing, or overheating during experimentation. A flow rate of 50 mL/min was initially utilized according to recommenda-

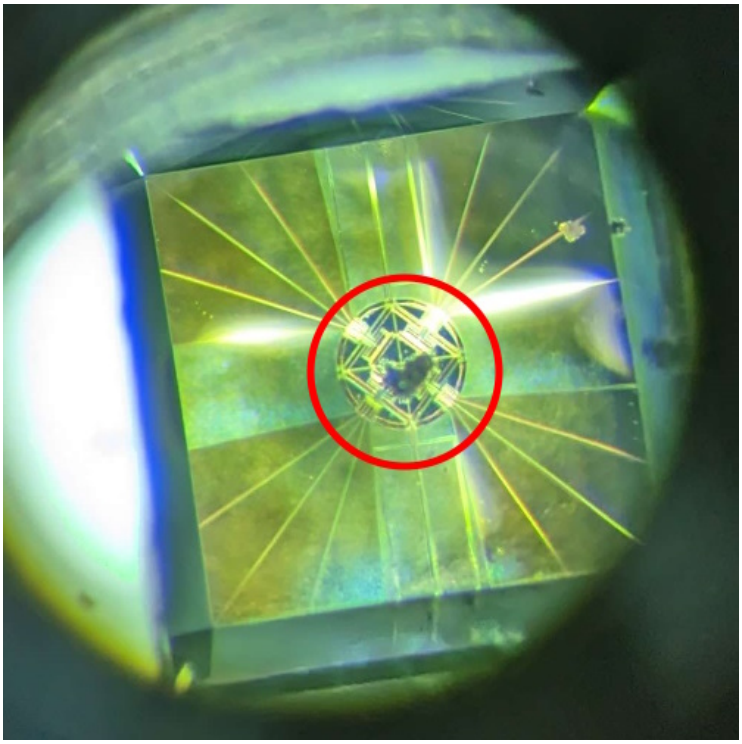

Figure 5.12: Photograph of sample placed on FlashDSC microchip, indicating the sample was fully contained within the central chip location.

tions by Mettler Toledo, however additional sensitivity analyses were performed as will be described in Chapter 6.

Conditioning followed a set program in which the temperature of the chip was raised according to the manufacturer's specifications as per the software provided with the FlashDSC. A total of five conditioning cycles were run before a final readying cycle to prepare it for use. After the conditioning had been performed, the FlashDSC could be opened, and the sample transferred onto the chip. After the sample was placed, the position and condition were verified through an optical microscope. The FlashDSC could then be closed and sealed, and the program initialized.

A number of initial experiments were performed to identify the ideal heating rate for the sample material, to find a middle ground between low-noise measurements, and ensuring the heating rate wasn't too high as to skip vital information. A series of 5 experiments were performed with varying heating rates, before a value was selected. A number of additional experiments including the use of a temperature melt-in period, to reduce moisture or other contaminants without causing annealing within the sample was used. This included 5 cycles in which the sample was heated to 120 °C, and

back to 25 °C at a heating rate of 1 °C/s. This was done to allow the sample to settle onto the microchip, and isolate any effects that may have been caused by the inclusion of moisture or other contaminants, and did not cause melting of the actual sample, as it was far below the expected melting temperature. After the melt-in period, the sample was heated to a max temperature of 420 °C a total of 6 times, which was selected as to not pass the acceptable temperature limit for the UFS 1 microchips while remaining reasonably close to the expected annealing temperature of the material. The addition heating cycles allowed the isolation of the first cycle, improving confidence in the results by exhibiting the difference in curve shape from the first cycles. The overall temperature program for the experiments, showing the melt-in cycles, and the experimental cycles can be seen in Figure 5.13.

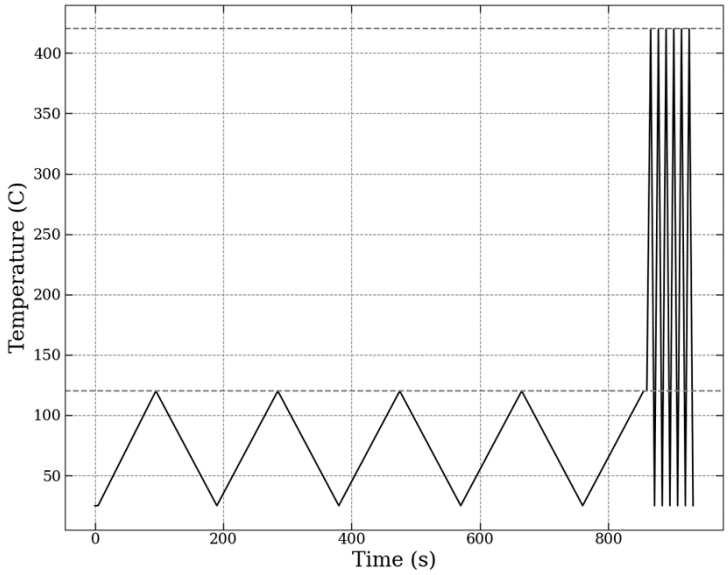

Figure 5.13: Overview of FlashDSC melt-in and experimentation temperature cycles.

5.6. DATA ANALYSIS

5.6.1. XPS ANALYSIS

After the results from XPS had been obtained, the data was in the form of raw counts per second based on binding energy of the scan area. Each of the scanned areas needed to be checked and have background noise removed such that only the relevant peaks for the data were isolated. This was performed using the software included with the Nexsa instrumentation, which allowed peaks and doublets to be applied to the data, and adjust the spread, amplitude and binding energy ranges for each data set

to better ensure validity of the results. After the peaks had been isolated, all data was exported to a manipulatable form, in which the total compositions were summed, and normalized to allow a final compositional analysis to be done on the elements observed. Each binding pair for the material was designated as an A, B or C binding, to be reported within the results. Some peaks may have been a combination of a number of elemental bindings due to the relatively low differentiation between pairs, and the inability to tell exactly which bindings would be present within the sample at the time.

5.6.2. TEM ANALYSIS

Due to the difficulty in analysing TEM data in terms of quantifying dislocations without an extensive data set, and intensive quantification methods, the analyses performed were qualitative in nature, identifying whether the radiation damage forms were of higher occurrence in one sample over another. While qualitative analyses would not allow quantification of the radiation damage, or calculation of the enrichment of the uranium, it would provide confidence in the analysis method, while deciding whether the influence of radiation was significant enough to allow differentiation from a control sample. This would point towards TEM being a suitable characterization method in the future, and would be viable for future research work to be completed.

For analysis of the received images, the overall atomic structure was identified, with any identifiable phenomena, or dislocation forms noted. From these forms, the overall occurrence, that being both location and concentration around macro size structures was identified to compare the overall dislocation propagation throughout the sample surface between the control sample and that of the potentially radiation damaged sample. After a dislocation was noted, the overall atomic structure was highlighted with post processing tools to allow observation and identification of the type of dislocation, and the most likely cause of formation.

5.6.3. TOF-SIMS ANALYSIS

The initial data output from ToF-SIMS was in the form of signal intensity vs. δ time, as the time elapsed between the sputtering of the sample, and the material detection as the mass spectrometer would differentiate the materials based on atomic mass. Due to the inherent small mass differences, materials with a higher atomic mass would have a lower velocity, and would therefore have a higher time of

flight, indicating a larger molecule. Due to the high atomic masses expected in this work, the time been sputtering pulses was increased to allow the heavier molecules additional time to travel to the mass spectrometer and reducing clumping or inaccurate detection of molecules. As mass of the target molecules increases, the ability to differentiate becomes more difficult as singular unit masses become a lower percentage change. A singular unit of mass increase from H to He would be a 200% increase, and is much more simple to isolate than when the mass delta is within a decimal of a unit mass, making differentiation between actinides and possible contaminants in the same range difficult. While it is more difficult, isolation of actinides should be possible with a consistent detection surface, and high enough initial composition for the relevant isotopes.

Two samples were analysed utilizing SIMS, those being a singular water washed sample and a singular ethanol based sample, such that the compositional differences between the two could be properly identified. From each of the samples, multiple areas were analysed to increase confidence that locational based artifacts were both not missed, and not the only areas analysed. In addition to the locational artifacts, the relatively rough surface caused issues with higher mass detection due to the relative difference in mass detection time due to surface height variance. As the height of the mass spectrometer from each surface point was not consistent, multiple analyses were performed with the data with low height areas excluded from the analysis due to the crowding or noise added to the data. An example of this can be seen in Figures 5.14 and 5.15, where only the areas consistent in height and roughness were included as the resultant peaks were much more clear with higher confidence. Removal of the non-consistent areas reduced the base width of the peaks, and constrained the overall estimated atomic masses of the detected materials, allowing much higher confidence peak observations to be made.

While the data indicates mass, a calibration of the data was required before results could be taken as accurate, and as such a series of common contaminants were utilized to calibrate the mass results. Due to the nature of sample handling, and ambient atmosphere, several well known hydro-carbon contaminants are common in the surface results of SIMS, those being compounds such as: NH_4, C_3H_3, C_3H_5, SiC_3H_9 and C_7H_7, which are common across samples, and were utilized in a calibration series for the results obtained in this work. Calibration of the results requires several materials that validate a wide range of potential masses, allowing accurate identification of materials into the high hundreds

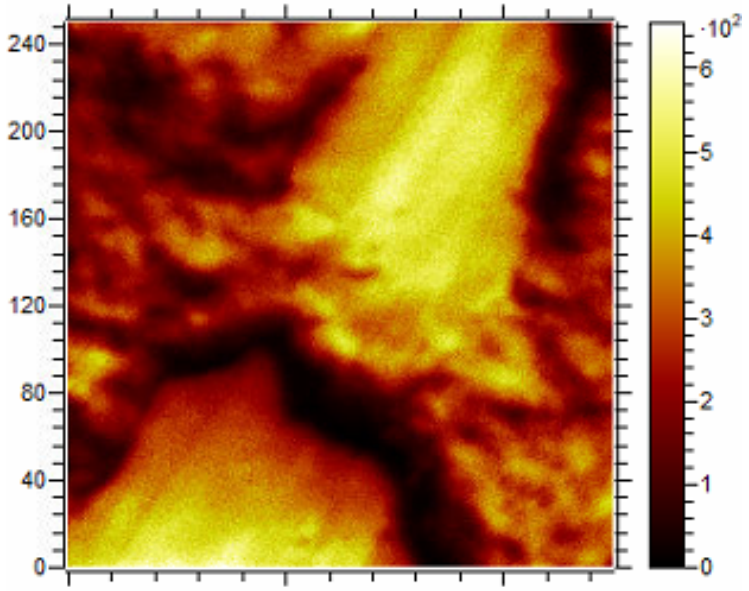

Figure 5.14: Example SIMS output area. High sample surface variance can be seen in the upper corners, and around the lower section of the image. Data collection area was 250 µm x 250 µm.

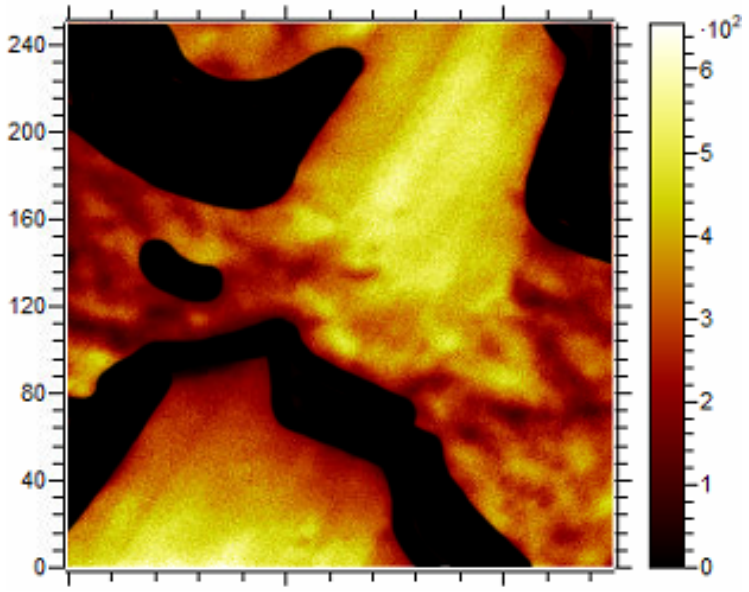

Figure 5.15: Example of SIMS height data cleaning. Sections with high surface variance were blocked out to reduce noise within the mass signal peaks. Data collection area was 250 µm x 250 µm.

of atomic mass units. As many of the compounds being examined within this work are in the high accuracy range, identification of uranium and actinide compounds should be possible, with isolation from singular mass unit differences.

After the results had been calibrated, the peaks associated with potential uranium and actinide

compounds were identified, and integrated to obtain the relative concentration of the materials on the outer surface sample. After the concentration had been determined, the results could potentially be ratio-ed according to natural radio-isotopic quantities to determine whether quantification of uranium enrichment was possible with the given accuracy.

5.6.4. FLASHDSC ANALYSIS

The data obtained from the FlashDSC analysis was given as a flow of heat, in the form of mW based on the temperature increase of the chip calorimeter, given in °C. To obtain the final stored energy release in a usable form, the data had to be converted to an amount of energy in J. The temperature was divided by the heating rate to convert the x-axis to time, which allowed isolation of the peaks of the curve. To remove background noise, and correct the baseline value, the 2^{nd} through 6^{th} heating cycles were used as a baseline, and the values normalized to be removed from the preliminary heating curve. The cycle curve was split up into relevant areas to identify each section, as two predominant areas were identified, one centred around 100 °C, and one around 200 °C to 400 °C. Due to the small difference within the curve centred around 100 °C, retrieval of heat flow was not performed, as the results would not have high confidence. The secondary peak was isolated and the background from later curves adjusted to fit the onset point of the peak. While the results could be improved through calculus based means, the data sets obtained through the limited experiments did not indicate enough data to fully isolate the stored energy fingerprint. Additional experimentation with added methods would improve repeatability and isolation of the peaks. After the peaks were isolated the integrated mW value was determined and divided by the time frame which heating occurred over, after which a final value in kJ could be obtained. These values were then compared to previous results to determine whether the energy was in the expected magnitude. The isolation of a singular first heating peak can be seen in Figure 5.16, in which a simple fit was utilized to set a baseline for the curve.

Determination of an energy value in kJ does not hold significant value without the ability to compare to other material forms and transitions. As such, comparison of a value in terms of kJ/mol would provide an avenue to compare the energy released to other phenomena such as phase transitions, and other forms of radiation damage. Generally the mass of the sample, as well as some knowledge of the material properties are required to properly convert the determine value into an accepted form. Due

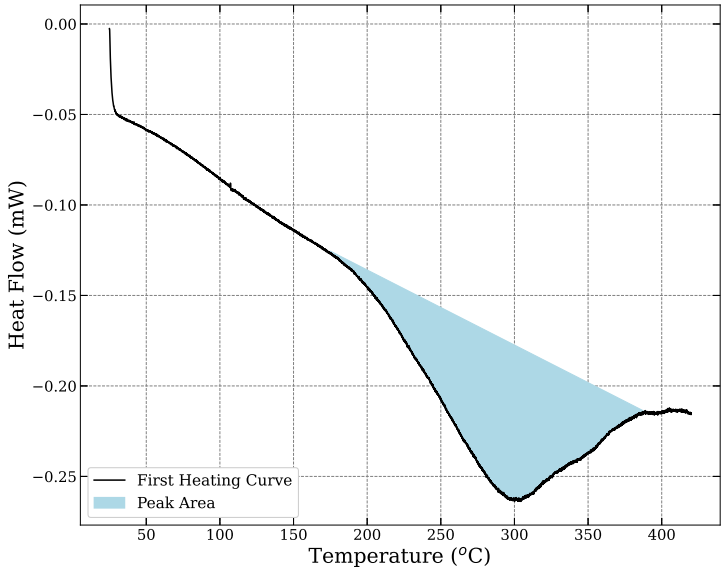

Figure 5.16: Overview of peak isolation from first heating curve. Various fit types were tested with minimal differences between final outputs.

to the lack of knowledge of the exact materials on the surface, as well as a lack of mass data, estimations had to be made to determine estimations of the molar mass, and quantity of mols that would be present. While methods to determine mass through heat capacity measurements are available, the lack of knowledge of the heat capacity of the surface leads to an inability to accurately determine the overall mass of the sample.

To begin, an estimation of the mass of the sample was required. Previous works determined the average mass of the sample when utilizing FlashDSC was in the middle 100 ng range, indicating a probable mass in the 300 ng to 1000 ng range would be reasonable [15, 16]. With this estimation, a range of values were taken for the mass and an averaged molecular mass applied in bins, allowing rough estimations to be performed. As previously discussed, it was likely that the outer surface of the material underwent corrosion in a predictable manner, leaving a series of materials ranging from Fe to UF_6. With this list, each of the molecular masses was determined, and binned due to the similarity between material molecular masses. As can be seen in Table 5.3, the molecular masses were determined, and separated into four bins, in which the masses would provide significant differentiation, while encompassing the materials that may be present. This would allow a high, and conservative estimation to be made on the overall energy released from the samples in kJ/mol. After the materials had been iden-

tified, and their molecular masses calculated, the averages could be grouped into four separate bins for further calculations, as given in Table 5.4. This list, while being approximate to what would be expected on the surface would cover a wide range of molecular masses in the case of the peak being a phase transition, while identifying potential energy release values.

Table 5.3: Molecular masses of expected cylinder surface materials [30].

Material	Molecular Mass	Group Number
$U_2O_3F_6$	638.09	1
UF_6	352.0	2
UOF_4	330.0	2
UF_4	314.0	2
UO_2F_2	308.0	2
Fe_2F_3	168.7	3
Fe_3	167.5	3
FeF_3	112.8	4
FeF_2	93.8	4
Fe	55.8	4

Table 5.4: Grouped molecular masses.

Group Identifier	Average Molecular Mass [g/mol]
Highest (1)	638.1
High (2)	326.0
Medium (3)	168.1
Low (4)	103.3
Lowest (5)	55.8

Once the energy released from each curve had been determined, it was converted to an appropriate range of values utilizing the estimated masses, along with the grouped molecular masses. Each FlashDSC experiment performed with an isolatable peak was utilized within the calculations, and overall top and bottom ranges found instead of a fixed singular value. The processing of results, along with the usage range of values obtained will be further discussed within Section 6.5.

6

RESULTS

This chapter describes the results obtained throughout the various analysis methods utilized, and gives an overview of the trends and significant factors. The results sections have been split according to the outcomes, and their relevance to the research topic.

6.1. DETERMINATION OF SURFACE COMPOSITION

On delivery, the composition and kinetics of the outer corrosion deposition layer were unknown, leading to difficulties with characterization due to the unknown materials present, as well as a lack of knowledge of the lattice structures present. To improve analysis abilities, efforts were made to characterize the composition of the outer surface to understand a better place to start subsequent analyses.

6.1.1. DISSOLUTION OF OUTER LAYER

After an initial test in which a sample was cleaned within a beaker of de-ionized water instead of ethanol, it was obvious that material on the sample surface had a much higher solubility in water than ethanol. This indicated that it was likely the deposits on the surface were composed of uranyl fluo-

ride compounds. Before cleaning, the samples were composed of a dark surface with spots of orange or beige, whereas after cleaning the sample surface became much darker, with the brighter spots removed (see Figure 6.1). The underlying colour was also consistent with the reported colours for ferric fluorides, as if the material had been iron oxide it would display a red or brown colour. Additionally, a radiation scan was completed on the cleaned sample in which no radiation counts were detected over a prolonged period. While the uncleaned samples were consistently low in radiation, occasionally an alpha particle was detected, whereas after cleaning a radiation scan of 3+ minutes did not indicate any counts. This indicated that any present radioactive material had been removed during the cleaning process, whether they were in the form of fluoride deposits or material dispersed over the surface.

After cleaning of the sample, it was noted that a layer of dissolved material had attached itself to the sample bag and solidified as observed in Figure 5.9. The material was orange in colour, as was expected with uranyl fluorides and was believed to have been removed from the cleaning bath with the sample as a discolouration of a similar shape was present on the surface. After observation of the material and the performance of a radiation scan to confirm radiation was being produced, it was covered with tape to prevent any material from being lost, or the material becoming an inhalation hazard. The presence of a radiation emitting material dissolving in water increased confidence in the hypothesis that the outer layer was composed of uranyl fluorides, and additional analyses could further identify the outer composition. Additionally, the lowered activity of the bulk sample after cleaning along with the radiation detected from the removed dissolved material leads to the conclusion that the dissolved material included all radioactive material on the outer surface of the samples.

From visual inspection, there was not any significant damage to the surface of the sample itself, only the removal of bright spots, leaving the surface a slightly different colour. It was expected that the outer deposition layer was removed, exposing the underlying iron fluorides or bare metal surface, which would likely hold significant forensic information and would allow better access for analysis.

6.1.2. OPTICAL MICROSCOPY

After determining that evolution of the metal surface through a UF_6 oxidation gradient was likely along with the solubility of the deposits, the samples were investigated utilizing an optical microscope such that colour of the surface could be determined as a better qualitative analysis check for the surface

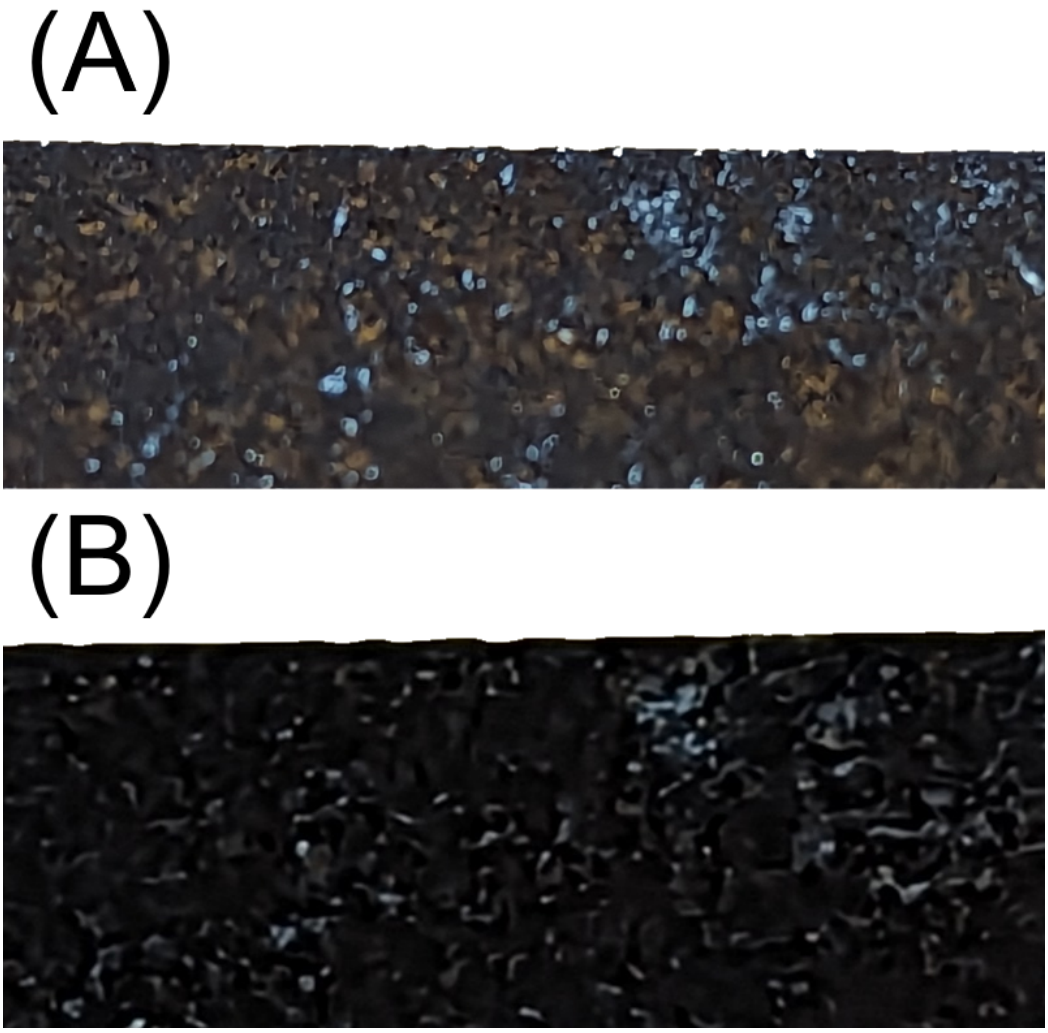

Figure 6.1: Comparison of ethanol washed sample (A) and water washed sample (B). The water washed sample indicated significant colour change.

composition. As the fluoride compounds each had differentiable colour schemes, the presence of bright orange or yellow materials would likely indicate that uranyl fluorides were present, which when combined with the results from Section 6.1.1, would help confirm the presence of uranium in the surface deposits. As can be observed in Figures 6.2 and 6.3, the ethanol washed sample exhibited large sections of raised orange deposits, whereas the water washed sample was observed to have fewer deposits that were ingrained in the surface. After altering the microscope's focal point, it was determined that these areas peaked from the lower darker surface, indicating a deposition on the outer surface as opposed to a metal alloy gradient. Additionally, the darker surface seemed to consist of a material of dark green or purple colour, which was consistent with the iron and uranyl fluorides located within the expected gradient. This further supports the development of the gradient within the cylinder conditions, and provides additional evidence for the previous claims.

The presence of these raised deposits was consistent with what was observed within the SEM results as will be discussed in Section 6.2, in which a primary consistent layer was present over the porous under-layer. This heavily indicates that the primary layer observed within the samples is a form of uranyl fluoride, and is the location and form in which the uranium within the samples is located.

Spherical structures were identified in the deposit areas (as seen in Figure 6.4), which were consistent with those seen later during SEM analyses (Section 6.2.2). While it was not possible to measure the size or dimensions of the objects using optical microscopy, the material surface finish, and overall metallic material were noted, for use in later comparisons.

Finally, close-up images were taken of the sample surface of the water washed sample to identify how the orange material was held on the outer surface. It was noted in Figure 6.5 that the deposit material left on the surface after washing was contained within lowered sections of the surface, in what seem to be cracks and crevices. This was consistent with what was expected, as the material would have a lower likelihood of being washed out during the cleaning procedure. It was also noted that an area of bare metal had been exposed due to a scratch on the sample surface. This area exhibited a distinct colouring and metallic finish, differentiating the area from the surrounding outer layer. Due to the differentiated colouring and finish, it is likely the outer layer of the surface is oxidized or fluorinated, as expected according to previous literature [30].

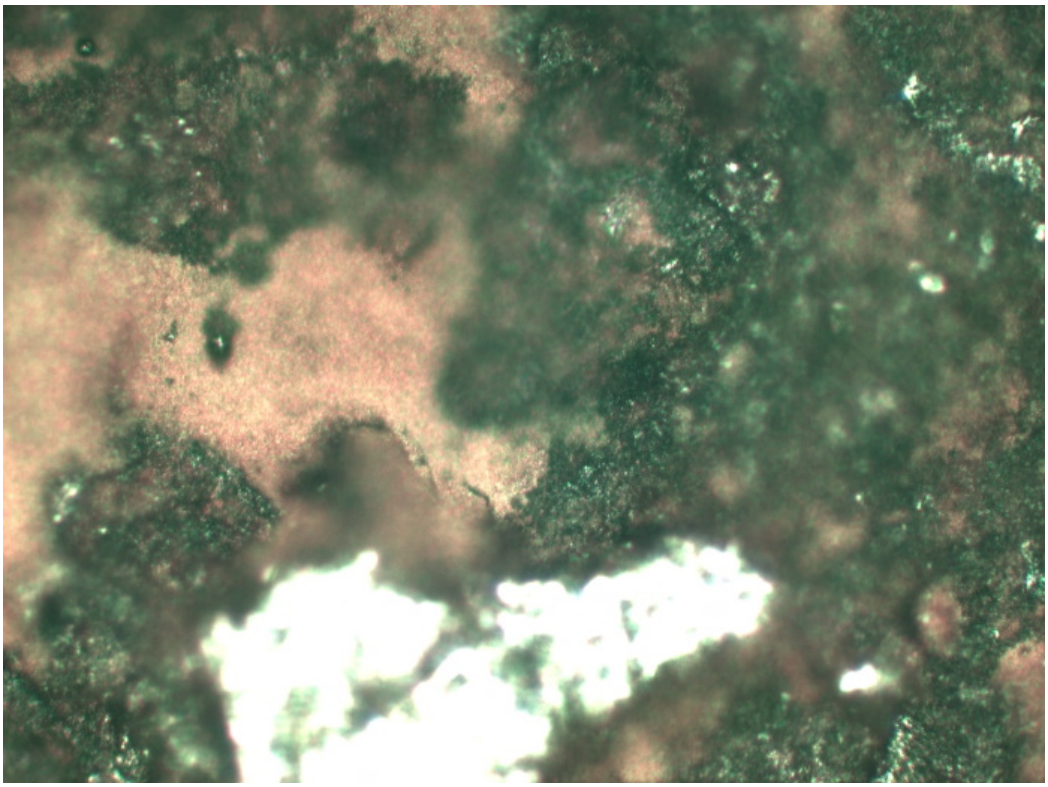

Figure 6.2: Optical microscopy photograph at 20x of ethanol washed sample, indicating significant raised deposit areas.

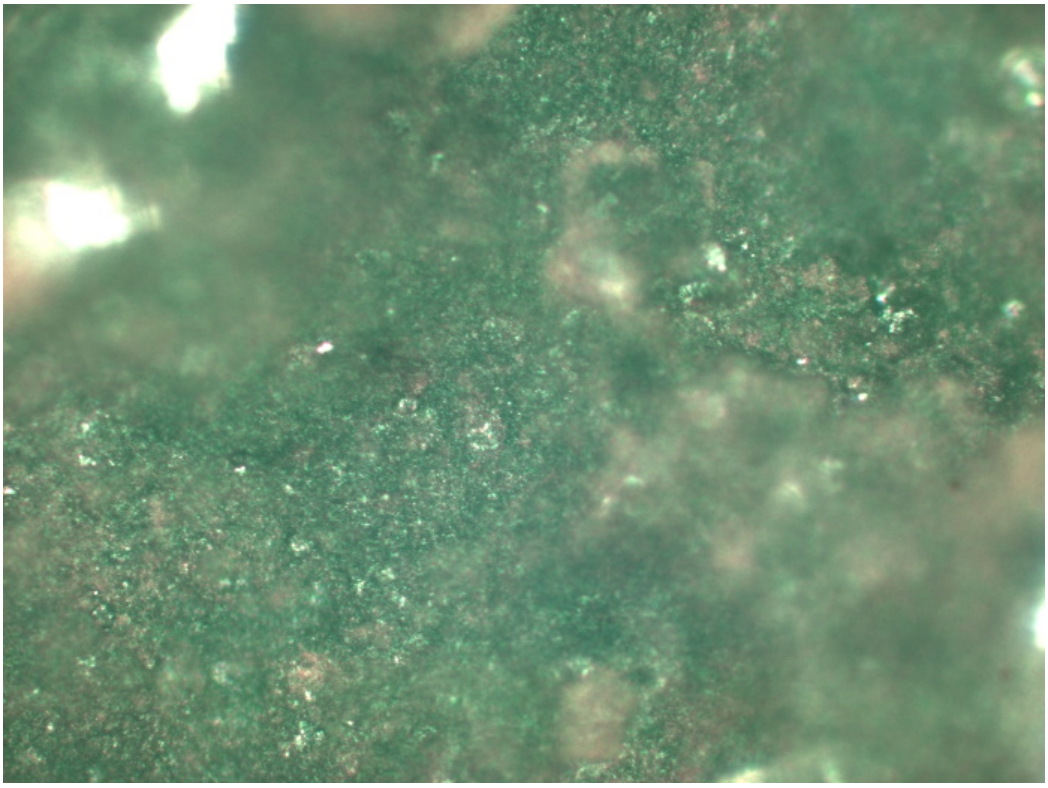

Figure 6.3: Optical microscopy photograph at 20x of water washed sample, indicating little deposit presence.

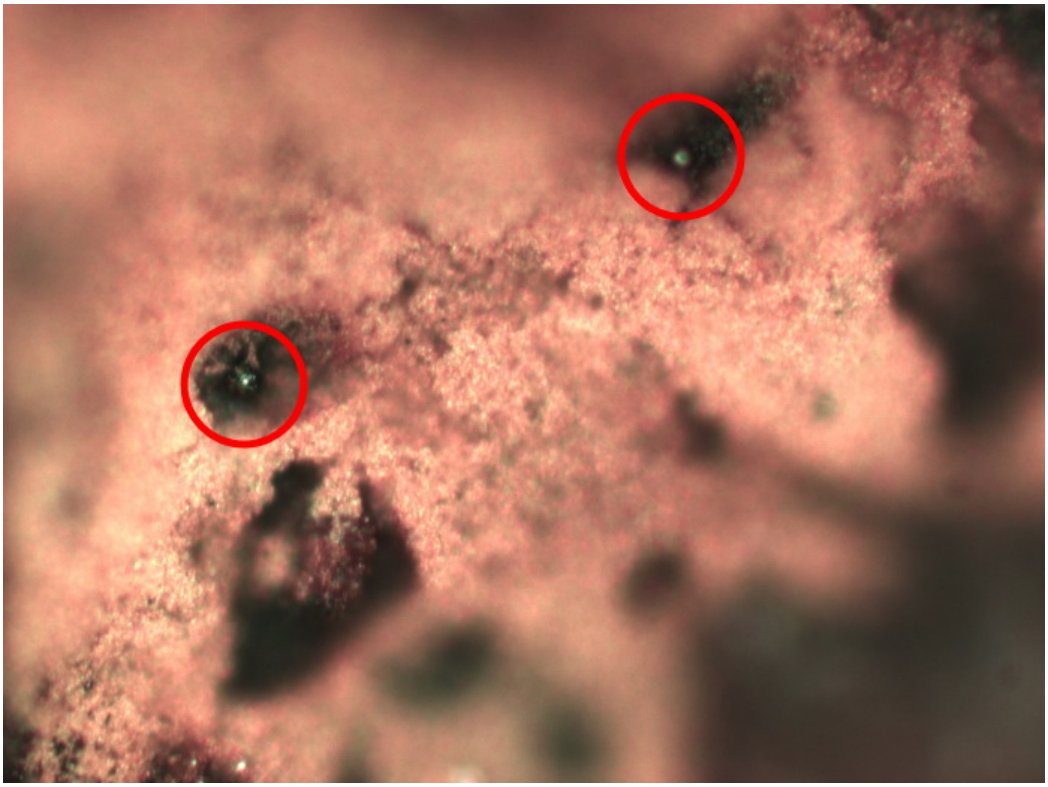

Figure 6.4: Optical microscopy photograph of identified spheres in deposit layers.

6.2. SAMPLE HEALTH VERIFICATION

During sample preparation, there were concerns that the outer surface of the samples would undergo significant damage due to the vibrations and contact with cutting fluids during the cutting stages. To ensure the samples were in good health before starting more complicated or precise analysis methods, such as XPS and TEM, the samples were investigated using SEM and EDS, to provide low magnification microscopy and elemental composition. The main purpose of performing SEM and EDS analyses was to confirm that sample preparation methods did not cause any significant damage to the outer surface of the samples, and to determine if there were any evident possible radiation damage markers that could be used in later analyses. A total of 6 samples were analysed using SEM, in which 5 were of the sample corrosion deposition layer, and one was used as a control test, in which a centre cut of the sample was taken to identify a baseline composition. For each sample, the corrosion deposition layer was observed to determine if any visible gradients or oxide hot-spots were present that could indicate the presence of phenomena such as re-alloying of the material, or re-crystallization of the oxide layer.

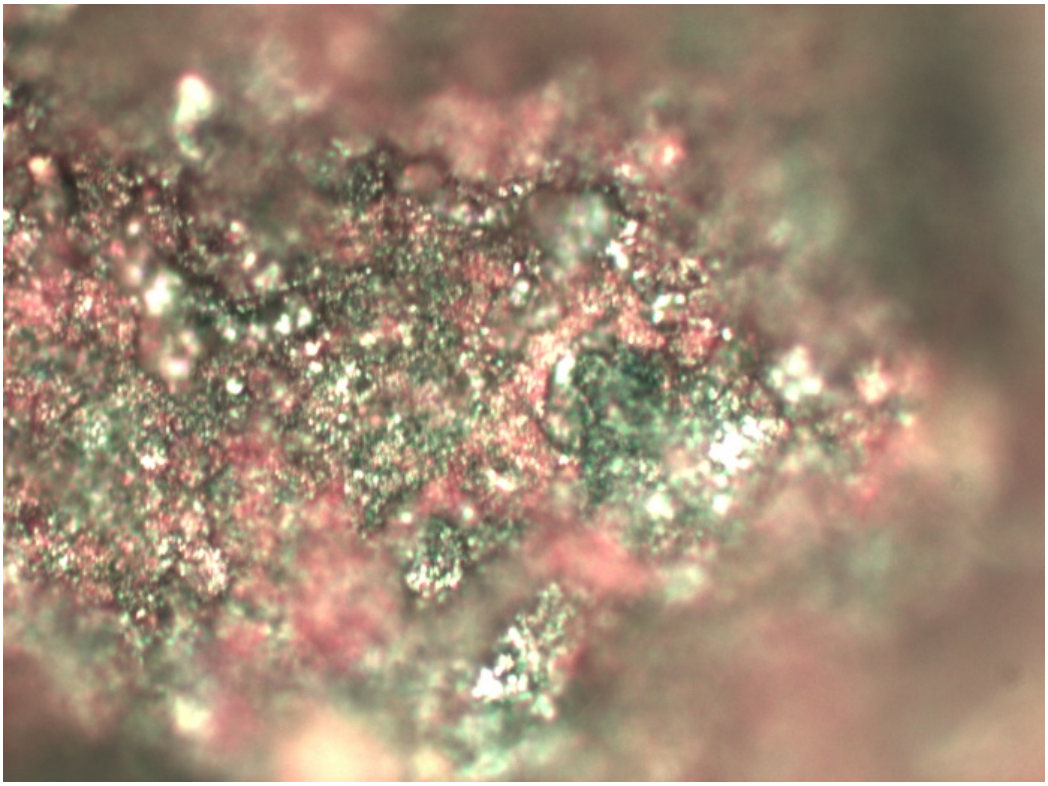

Figure 6.5: Optical microscopy image at 50x of surface deposits in water washed sample surface. It was noted that the orange deposits were contained within crevices and cracks in the surface.

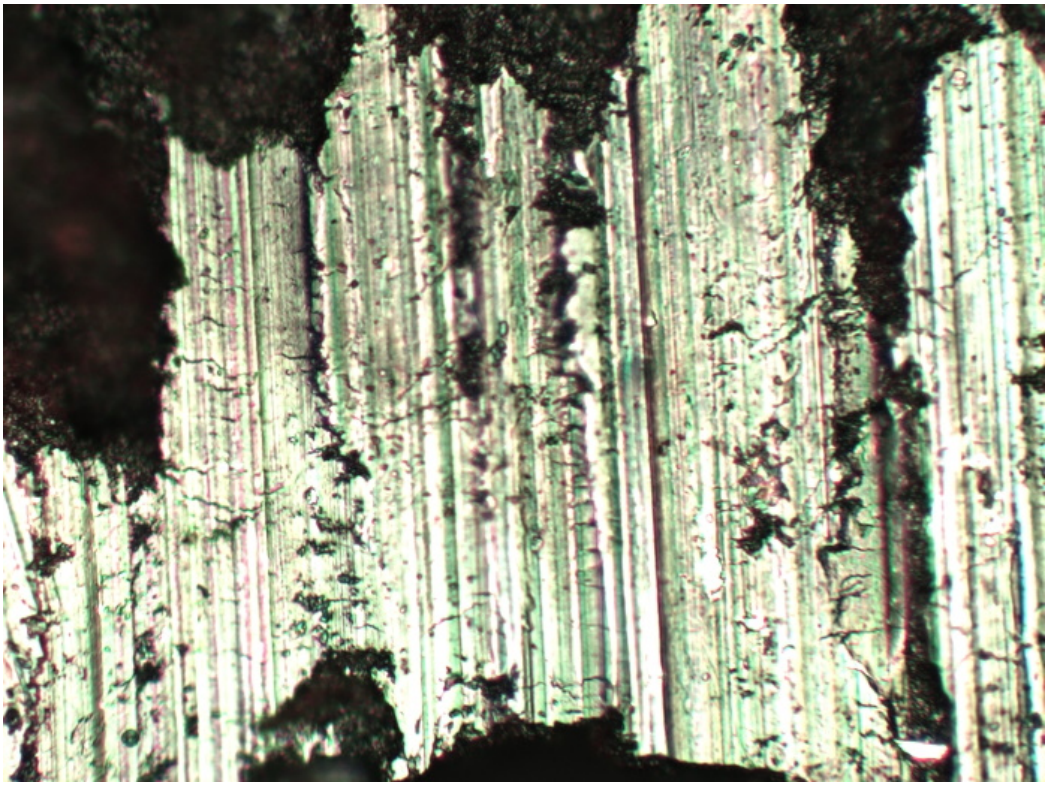

Figure 6.6: Optical microscopy image at 50x of a scratch on the water washed sample surface. The exposed bare metal displayed a metallic finish, and distinct colouring, different to the rest of the outer layer.

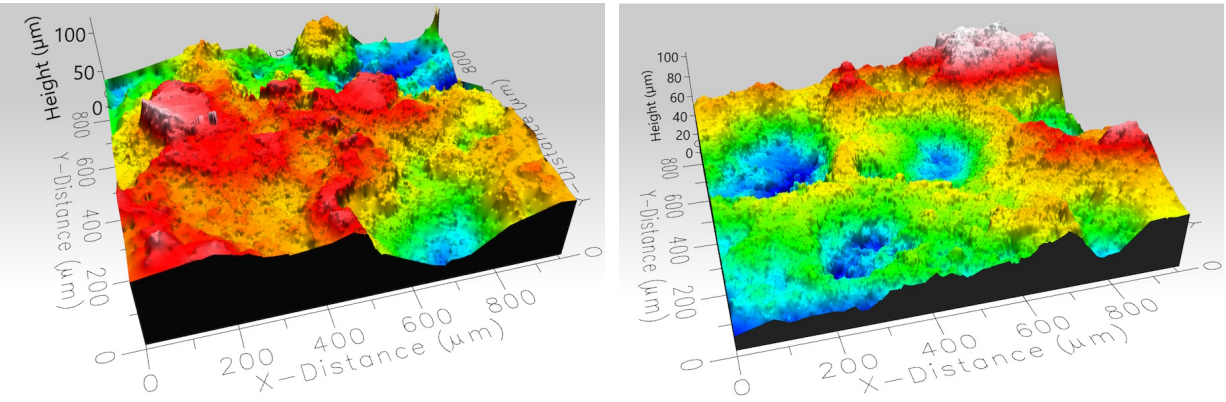

(a) Sample 7A-2-2.

(b) Sample 8A-1-1.

Figure 6.7: Overview of the topography of samples 7A-2-2 and 8A-1-1, indicating high variance in outer surface height. Both samples indicated a similar structure with high variance.

Additionally, any visible phenomena were documented, such as any structures or oxide phase areas that may be present.

6.2.1. SURFACE TOPOGRAPHY

Topographical images of the samples were additionally taken during initial surface analysis, to investigate the overall surface roughness and take a high level look at any potential large-scale surface damage to the samples. The analyses were performed with a Profilm3d profilometer within the Material Characterization faciltiy at Ontario Tech University at the time that the XPS analyses were performed. The results of two topographical analyses can be seen in Figures 6.7(a) and 6.7(b), in which it can be noted there was significant height differences within the oxide of the material, with up to 100 µm deltas observed. Figure 6.7(a) indicates a number of plateau regions, in which the oxide flattened, with minimal peaking observed. While Figure 6.7(b) shows several cratered regions with minimal flat or even surfaces observed. The two images were consistent with the results seen within the SEM images. It is likely that sample 7A-2-2 indicated regions of the surface deposit, where large flat areas were present, while sample 8A-1-1 indicated a region of partial deposit with areas broken off or otherwise removed from the outer layer.

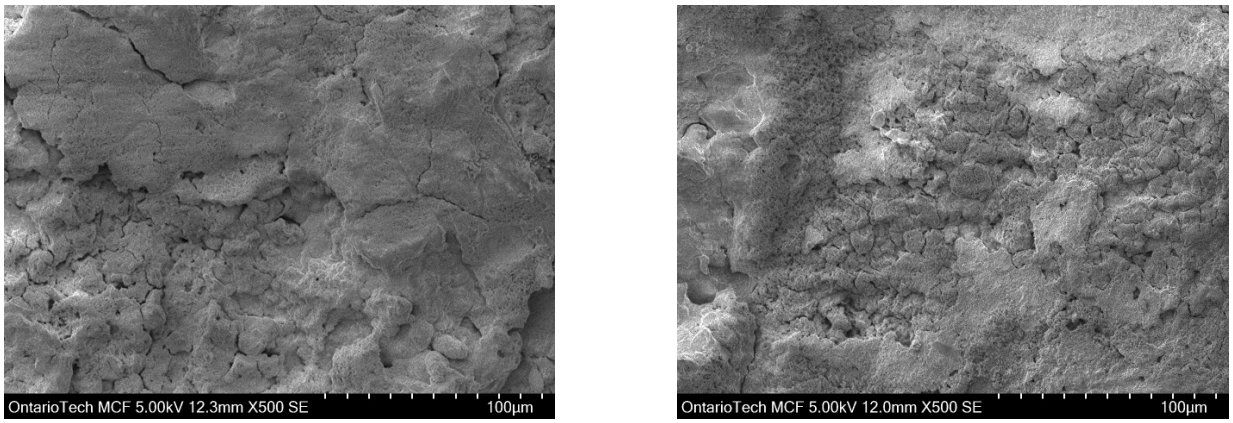

(a) Sample 7A-1-1.

(b) Sample 8A-1-1.

Figure 6.8: Overview of the general surface deposition of samples 7A-1-1 and 8A-1-1 through SEM. Surfaces indicated significant cracking, pitting and cratering, but were consistent between samples.

6.2.2. SEM ANALYSES

Performance of SEM on the selected samples indicated that the overall health of the sample surface was acceptable, and there seemed to be an outer deposition layer on the outer surface, whether that be an oxide or fluoride based material. As seen in Figures 6.8(a) and 6.8(b), the outer surface formation for samples 7A-1-1 and 8A-1-1 exhibited similar oxide formation with no visible damage or outliers observed.

Analysis of the samples cleaned in de-ionized water exhibited a surface condition different than those cleaned in ethanol, with the previously apparent surface deposition layer having seemingly disappeared, exposing the underlying oxide/fluoride iron, and bare metal spots. The surface indicated areas with similar cracking and pitting, however the overall surface finish was more consistent across the sample with no smooth areas. As can be seen in Figure 6.9, large areas of pitted and cracked surface are visible with few smooth surfaces present. Figure 6.10 indicates an area believed to be bare metal showing through the deposition layer. The deposition layer can be seen over the lighter material, indicating the presence of an inner and outer layer of the sample surface, giving confidence in the layering of corrosion products.

SPHERICAL INCLUSIONS

During SEM analyses, spherical growths were observed on the outer surface of the sample, ranging in size on the 100 µm scale. Initially the growths were noted on the outer layers of the surface, located on

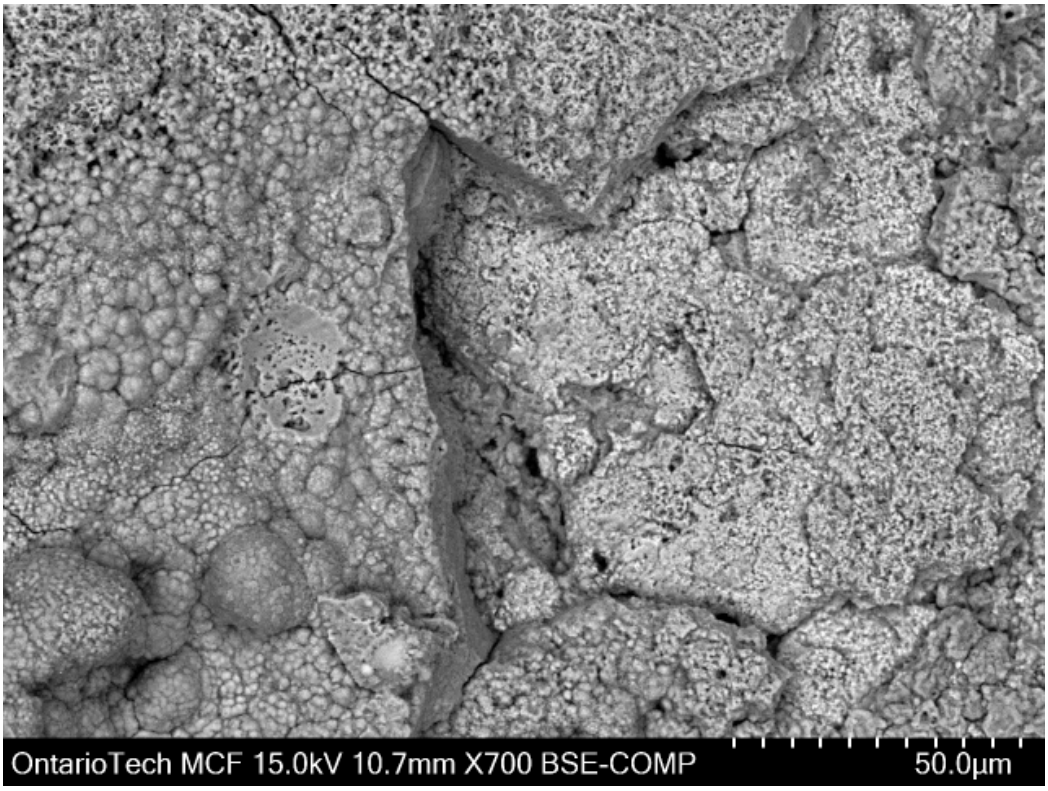

Figure 6.9: SEM image at 700x of the surface of a water washed sample, showing wide pitting and cracking of the surface.

the more consistent, smooth areas, which were later believed to be uranyl fluoride compounds. Figure 6.11 shows a spherical growth located in the outer layer, with slight damage to the outer surface. Through this damage, the inner grain boundaries of the material were observed, where it was noted the structure was significantly different than the surrounding material. In comparison, Figure 6.12 indicates a spherical structure from the lower layers of the water washed sample, wherein the outer surface was missing, and the inner structure of the sphere was hollow. It is likely this was caused by washout or removal of the inner sphere material, as opposed to the sphere being hollow initially. The presence of the spherical growths in both the deposition layers, and underlying surface indicate growth during the lifetime of the cylinders, not contamination of the surface afterwards. Additionally, the presence underneath the deposition layer indicate the possibility that these spheres may be a contamination or inclusion in the UF_6, and may act as an outside indicator of UF_6 presence.

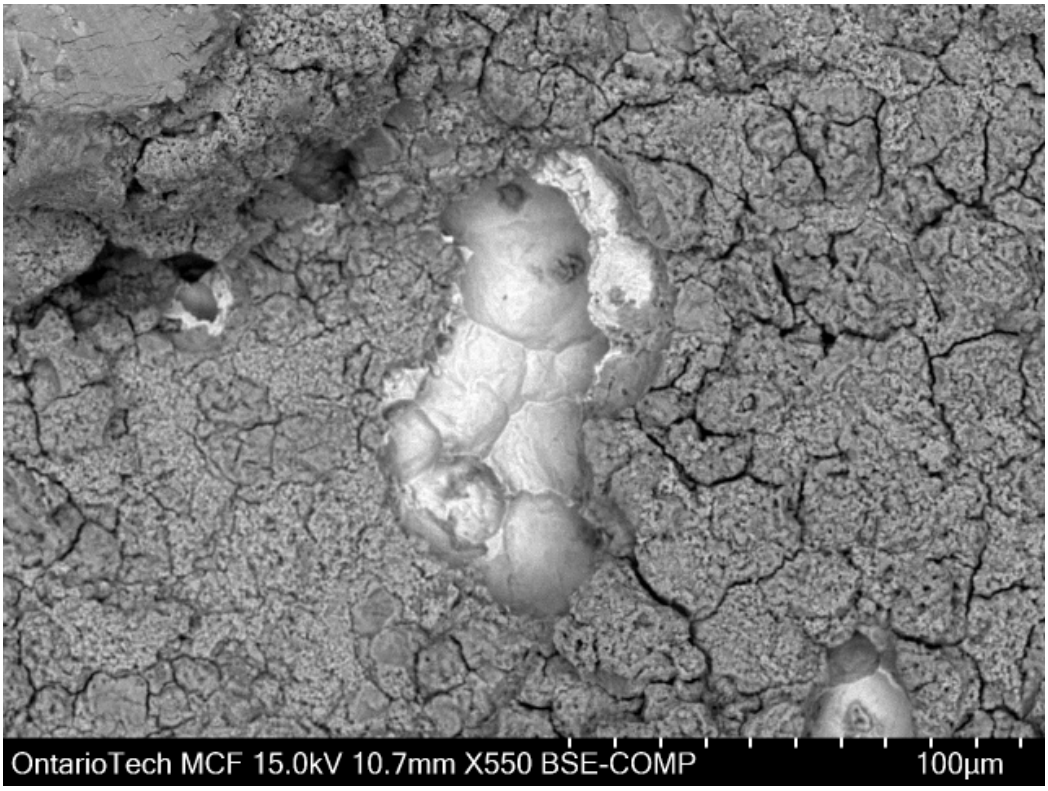

Figure 6.10: SEM image at 550x of the surface of a water washed sample, showing an area that is believed to be bare underlying metal. The right side of the damaged area shows a thick gray deposition layer over the below material. The light gray material does not exhibit any significant cracking or damage present.

6.2.3. OUTER LAYER THICKNESS

Initially it was believed that the outer layer of the sample was an iron oxide, which would be influenced heavily by the radiation damage occurring during the cylinder lifetime. While it is likely that the outer layer in many places is composed of a fluoride, the measurement of the layer is important for understanding the mechanics of corrosion and radiation interactions with the inner material. Determining the thickness of the outer layer was vital for the viability of layer analyses due to the penetration range of α particles. As the penetration of particles is roughly 20 µm in metals [15, 16, 25], for radiation damage to be contained within the outer deposit layer the thickness must be greater than the penetration depth. Sample 7A-1-1 was taken and flipped sideways to observe the thickness of the outer layer through a cross-sectional analysis to determine whether the layer was developed enough, or whether it was too thin to consistently measure damage from. As can be seen in Figure 6.13, the outer layer can be visibly differentiated from the inner material, with the thickness varying greatly with the general area

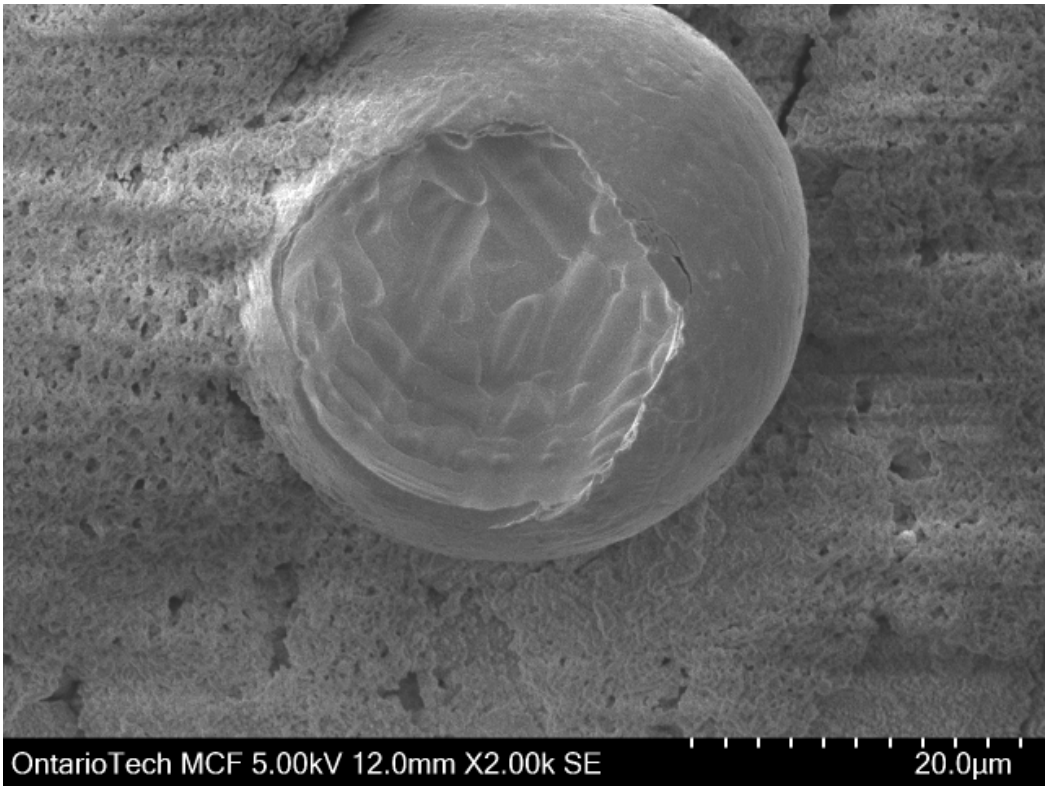

Figure 6.11: Sample 7A-2-2 at 500x magnification. The surface indicated a mostly intact spherical growth located in the outer layer.

of the layer. Some areas are much thinner than others and are likely due to the lack of layer deposit on the surface, but was quite thick, being much thicker than required to contain the radiation penetration into the sample. As such, additional investigation into whether these areas contain significant radiation damage should be performed to determine if the layer is protective of the underlying metal through prevention of the development of lattice damage, or is receptive to damage itself. Figure 6.14 indicates the outer layer, coloured in blue, and the relative thickness utilizing the scale from the SEM imaging instrumentation. While the layer thickness varied, it was quite thick in many areas.

6.2.4. EDS ANALYSES

EDS analysis was utilized to identify any significant compositional changes between the samples and obtain a general overview of the elements present in the surface while checking if actinides were visible with the equipment available. While less accurate than SIMS in terms of detection limits, the use of EDS was a preliminary check analysis to provide a basis for subsequent analyses, while checking what

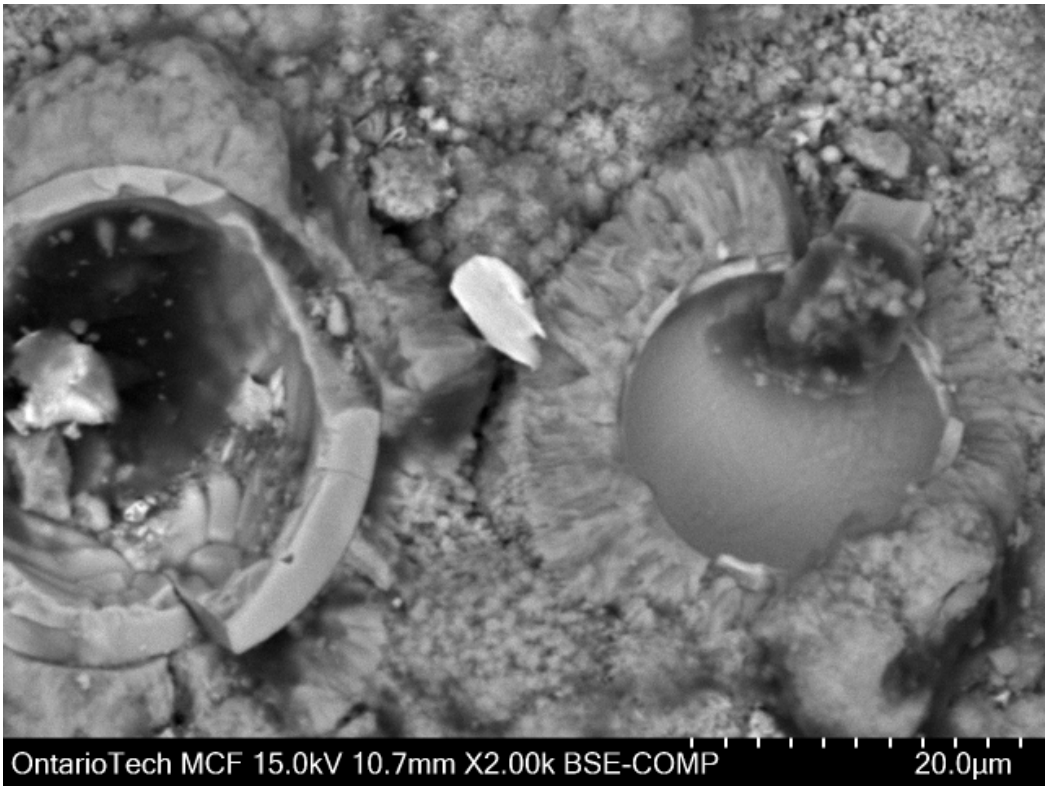

Figure 6.12: Water washed sample at 700x magnification. The spherical inclusions were observed in the lower layers of the material. The outer layer of the spheres had degraded, indicating a hollow shell.

capabilities were possible to determine uranium enrichment in the future. During the analysis, EDS analyses of both the water and ethanol washed samples was performed, which helped confirm results of the outer layer being affected. As can be seen in Figure 6.15, an area with a high Fe composition and low oxygen or other contaminants was observed. This indicated it was likely that the inner bulk metal had been exposed during washing, confirming bulk metal material was present, and would likely be exposed to radiation.

INITIAL COMPOSITION RESULTS

While the use of EDS was confirmatory and used as a low barrier of entry way to confirm sample health, it provided important results confirming the presence of alloy constituents and elements such as O and Mn while identifying any high compositional areas. Certain elements could not be accurately determined due to their proximity in energy if one element has a much higher compositional presence. This effect was most prevalent with elements such as Fe and F, whose energy areas overlap and with Fe constituting such a large percentage of the composition of the surface. As can be seen in Figure 6.16,

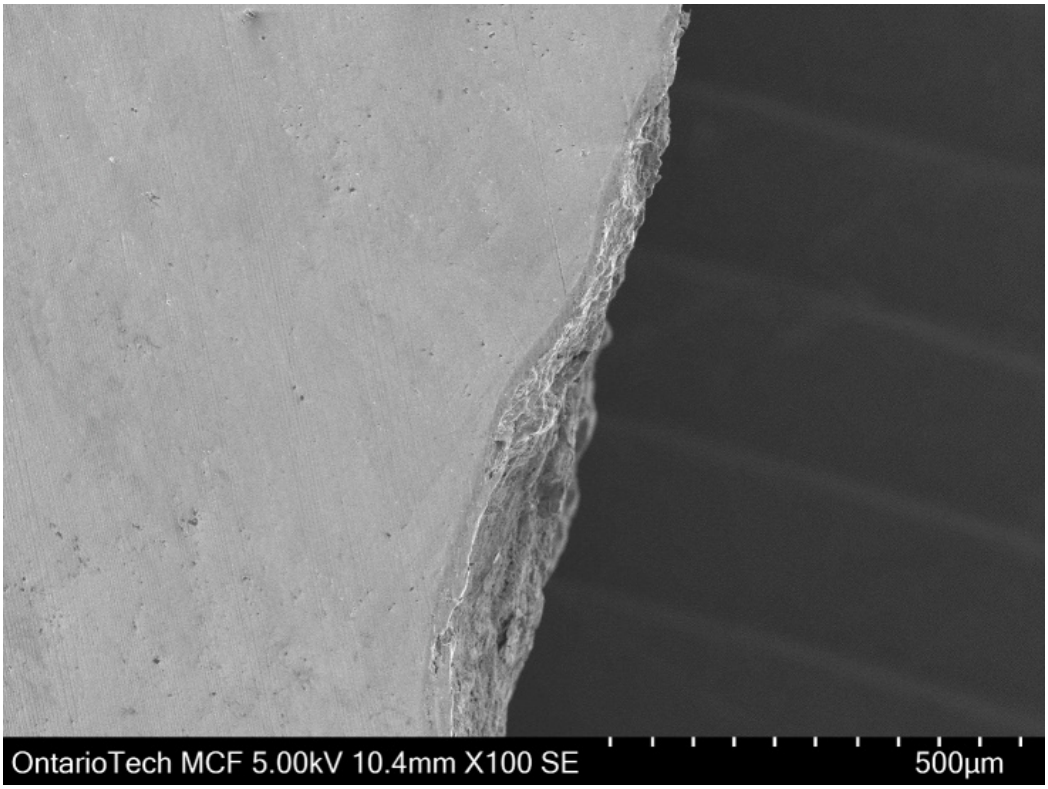

Figure 6.13: SEM image at 100x indicating the general thickness of the deposit layer, and the significant difference in colour.

any potential signal that may be present indicating F would be hidden within the peak for Fe, reducing confidence in the results. It is also worth noting that the detection of lighter elements such as O and F in general is difficult or impossible with EDS due to the measurement methods utilized. As EDS instruments utilize K x-rays, the energy of the resultant x-rays would be low, and likely to be absorbed, and many elements lack characteristic x-ray energies, such as H. This leads to an inability to measure and quantify the elements accurately, and elements with a Z value lower than 11 are generally taken as non-accurate.

6.2.5. XPS ANALYSES

The main elements being investigated within the performed XPS analyses included the constituents of A516 Grade 65 steel, as well as uranium, fluorine, and decay products of both U-235, and U-238. The purpose of the analysis was to determine if there was consistency between samples and identify if actinides could be observed, and accurately measured if possible.

During the analysis, the atomic percentage of each elemental scan was taken and a comparison

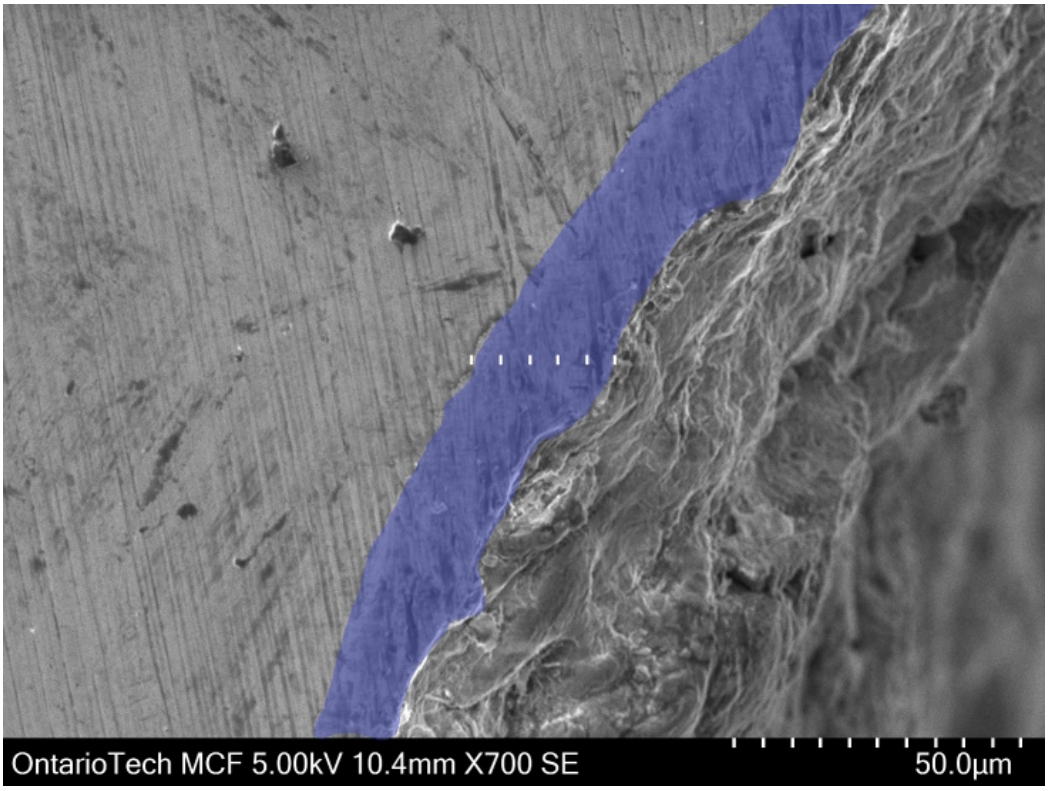

Figure 6.14: SEM image at 700x indicating the thickness of the layer is over 250 µm in some areas, greater than the required thickness for α penetration.

performed to determine whether the elemental distribution was consistent across each sample. The analysis shown in Figure 6.17 indicates the relative atomic percentages of each elemental scan. Each scan related to a different binding energy peak. The presence of secondary peaks or compounding peaks indicated the presence of contaminants, or lower compositional bindings. It was noted that while most elemental scans indicated consistency between samples, the scans relating to O, C and F exhibited disparities. These disparities were indicative of varying compositions in the case of F, and a difference in which elemental bond was present in the case of O and C due to the overall parity between all scans of the element. As seen in Figure 6.18, the elemental scan for sample 8A-1-2 exhibited a much lower composition for scan A, indicating less O was held in that specific bonding.

CARBON RE-CRYSTALLIZATION

While performing XPS analyses, the carbon crystallization of the samples was measured to identify if any re-crystallization was occurring. If the radiation had been affecting the carbon within the sample, and causing re-crystallization or re-alloying, the crystallization number would have changed, causing a

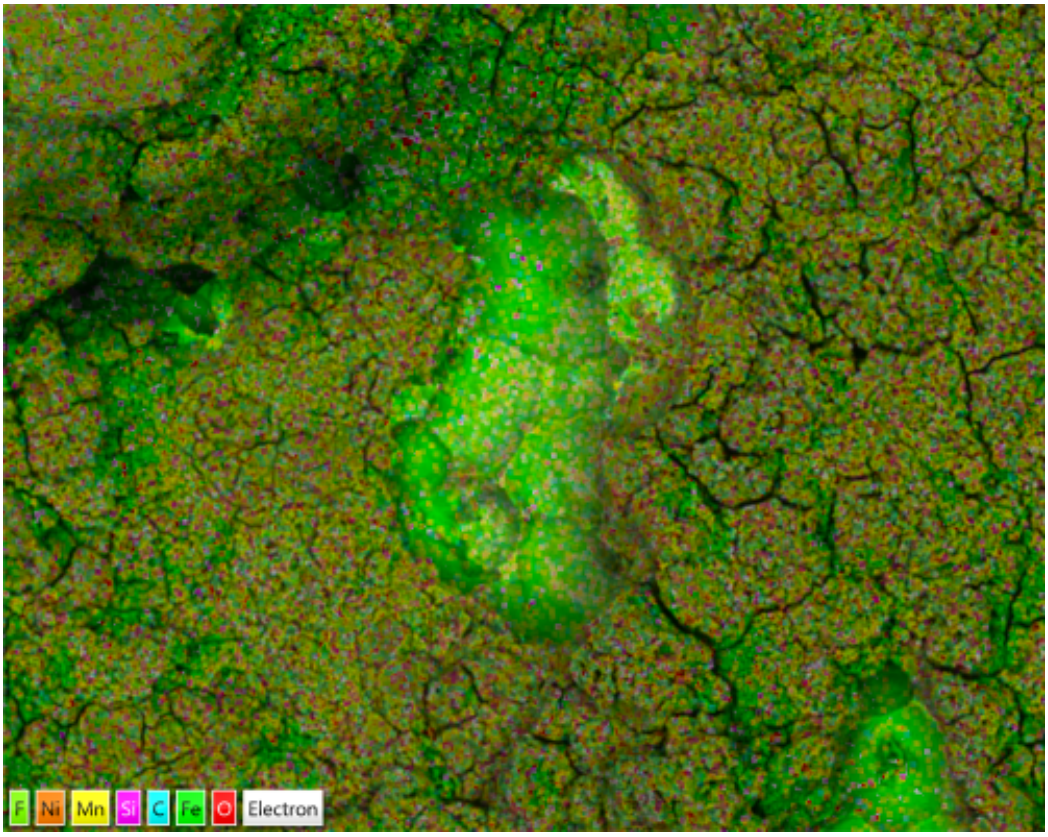

Figure 6.15: EDS ouput for the water washed sample, indicating the general EDS composition analysis for the outer layer of the surface. Results indicated an area of bulk metal had been exposed after dissolution in water.

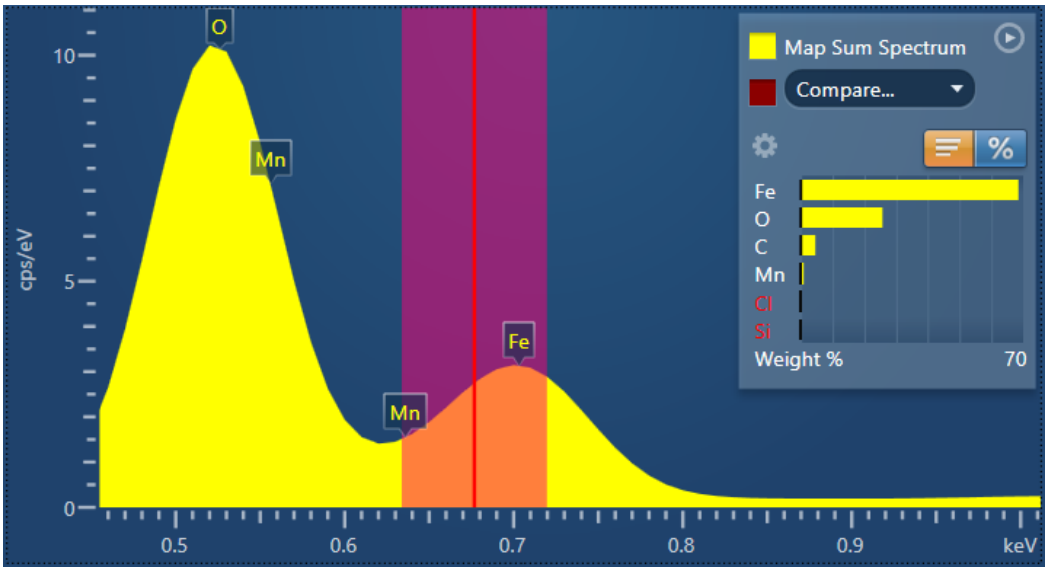

Figure 6.16: EDS output for sample 7A-1-1, indicating the overlap between Fe and F for EDS purposes. The overlap makes it difficult to reliably detect F in Fe rich materials.

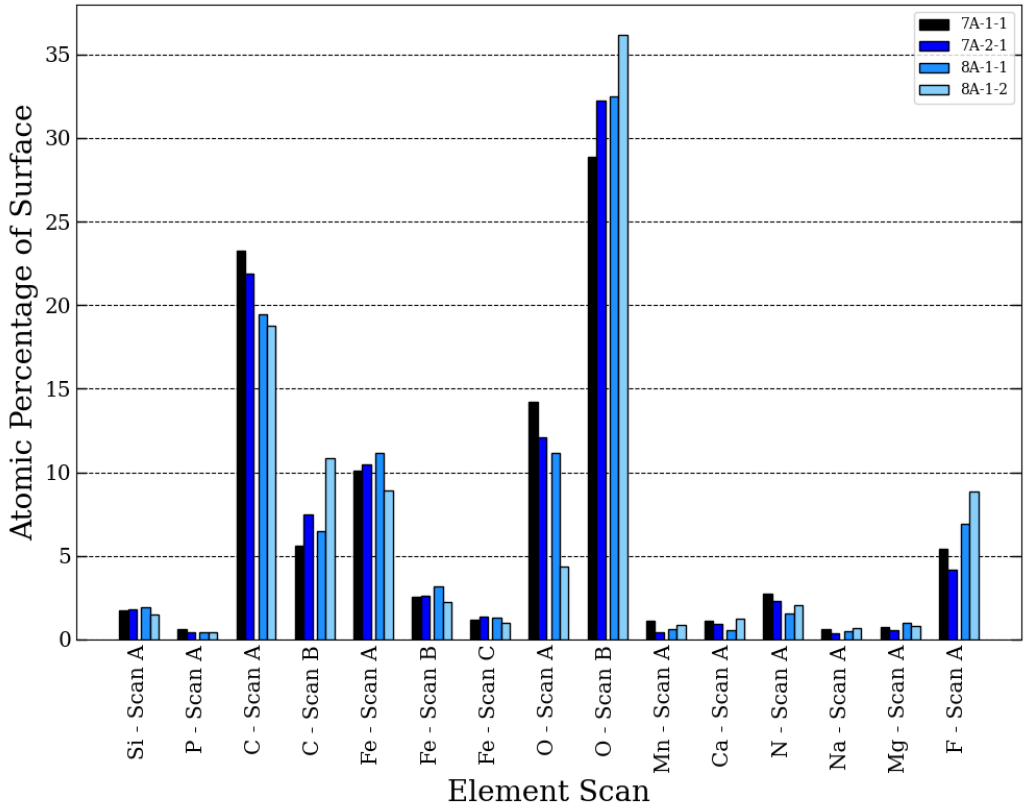

Figure 6.17: Atomic percentages of each elemental scan, indicating relative percentage across samples. Most elements remained consistent, with oxygen, carbon and fluorine indicating the biggest disparities.

quantifiable difference in the results. The hypothesized main elements for re-alloying would be carbon and manganese due to the high compositional values, ability to measure crystallinity, and presence in the material alloy. A value was taken for the surface of each of the samples, which indicated similar values for crystallization of the material on the oxide surface. During the analyses, crystallization was determined to be consistent across the samples, indicating that there was little to no variance of the phenomena at the surface level. While radiation would cause re-crystallization consistently across the sample, it is likely there would be some differentiation across the surfaces. Additional experiments could be performed at lower depths, measuring the crystallization as a function of depth to determine if the radiation penetration has a greater effect.

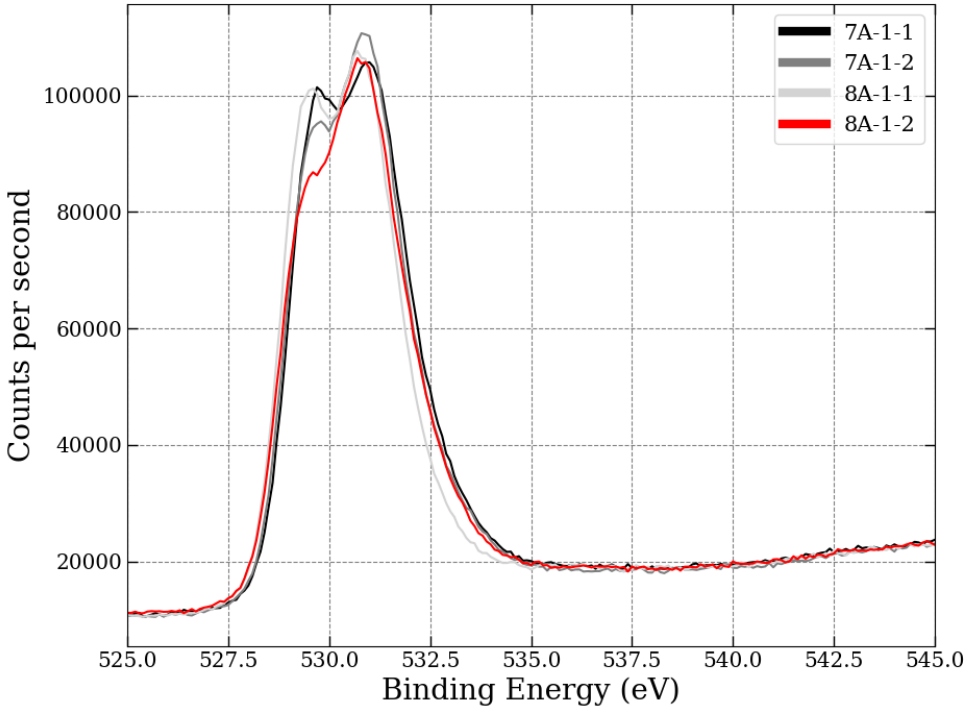

Figure 6.18: XPS scans relating to O composition. Sample 8A-1-2 indicated a much lower composition for scan A.

6.2.6. ToF-SIMS For Compositional Analysis

While the main purpose of SIMS was to identify trace quantities of actinides and other elements, the technique allowed the detection of elements such as fluorine, iron and their derivatives, allowing a better estimation of the surface compositions to be made. It was previously hypothesized that the surface of the samples was composed of iron and uranyl fluorides, which were water soluble. If that were the case, SIMS results would indicate heightened F signals from ethanol washed samples, and iron based signals from water-washed samples. As can be seen in Figure 6.19, significant disparities were observed between the samples, with minimal F in the control sample, and a high O and F to Fe ratio seen in the non-control samples.

From the results it was indicated that the F to Fe ratio from sample 7A-1-1 was significantly higher than that of sample 7A-2-2, as expected due to the reduction in washed away material. This indicates that the deposit on the outer surface has a high F content, and was likely composed of a combination of uranyl and iron fluorides as posited. When compared to the control results, the F ratio of both samples

was much higher, which indicates that even after washing there are considerable deposits remaining on the surface, likely in crevices and cracks. Due to this residual material, uranium is expected to be detected in minute amounts, even after water washing, at a much lower amount than ethanol washed samples.

It is worth noting that in the case of sample 7A-1-1, the signals relevant to F and O compositions reached the detection limit of the instrument, indicating it was likely that counts were missed and the relative ratios were higher than indicated. Additionally, the data from the control sample indicated significant Fe presence, with little to no hydrocarbon contamination, as would be expected from an inner surface of the material. As the material would not have been exposed to the atmosphere until after sample sectioning, little hydrocarbons should have been present, placing higher confidence in the results. As such, the presence of such a high O ratio, and low F composition leads to confirmation that any outside F within the sample surface was introduced through interaction with the UF_6 material.

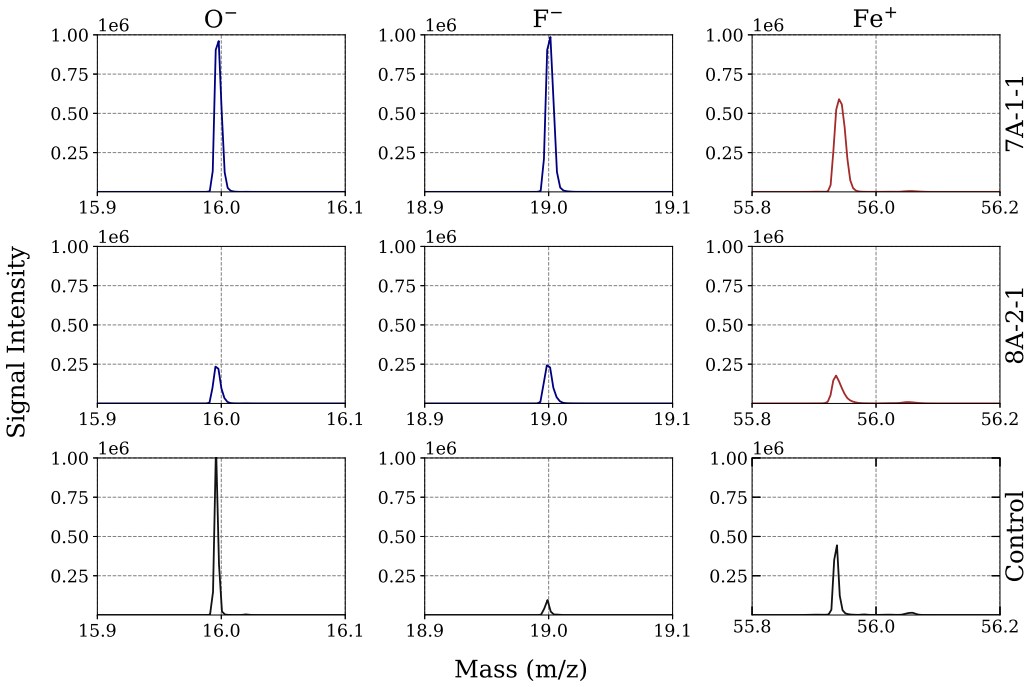

Figure 6.19: ToF-SIMS output showing masses for O, F, and Fe. Samples 7A-1-1, 7A-2-2 and a control data set were shown. Positive ions are shown in red, negative in blue, with the control set in gray.

6.3. IDENTIFICATION AND QUANTIFICATION OF ACTINIDES

6.3.1. INITIAL CHECK WITH EDS

While performing sample surface checks with EDS, the energies for actinides were investigated to determine if the composition was high enough for detection even with the much higher threshold required. Analysis of the EDS data for several spots within the samples determined the overall composition was far too low to be detected using the EDS instrumentation available. Additionally, the binding energies for the actinide compounds likely present were not defined within the software or instrumentation utilized, leading to lower confidence in the received results, and increased difficulty in determining the compounds even if detection was possible.

6.3.2. PRELIMINARY CHECKING OF TH, PA AND AC USING XPS

While performing XPS analyses, additional scans were performed based on previous work done by Krause *et al.* [50], which indicated binding energies of various actinide based compounds, allowing elements such as Pa, Ac and Th to be potentially observed. From this data, scans of existing materials were extended to include the reported binding energies to determine whether consistent peaks could be observed within the data [50]. As can be seen in Figure 6.20, the regions corresponding to both Pa and Th did not indicate any significant peak in the expected regions above background counts. While these elements could very well be present, the lack of visible peaks indicated they could not be quantified through XPS analysis. Additional analyses were performed to identify if Ac was present, as well as U, but neither range indicated a significant increase over background counts. From this observation, while it is almost guaranteed that the decay products were present within the surface of the samples due to the radiation measured, they could not be adequately detected through the methods previously utilized. The presence of F in the elemental scans also supports the presence of U and decay products, but due to the ratios present, and the likely low overall concentration of decay products within the surface makes detection difficult without a sufficiently high accuracy and low noise threshold.

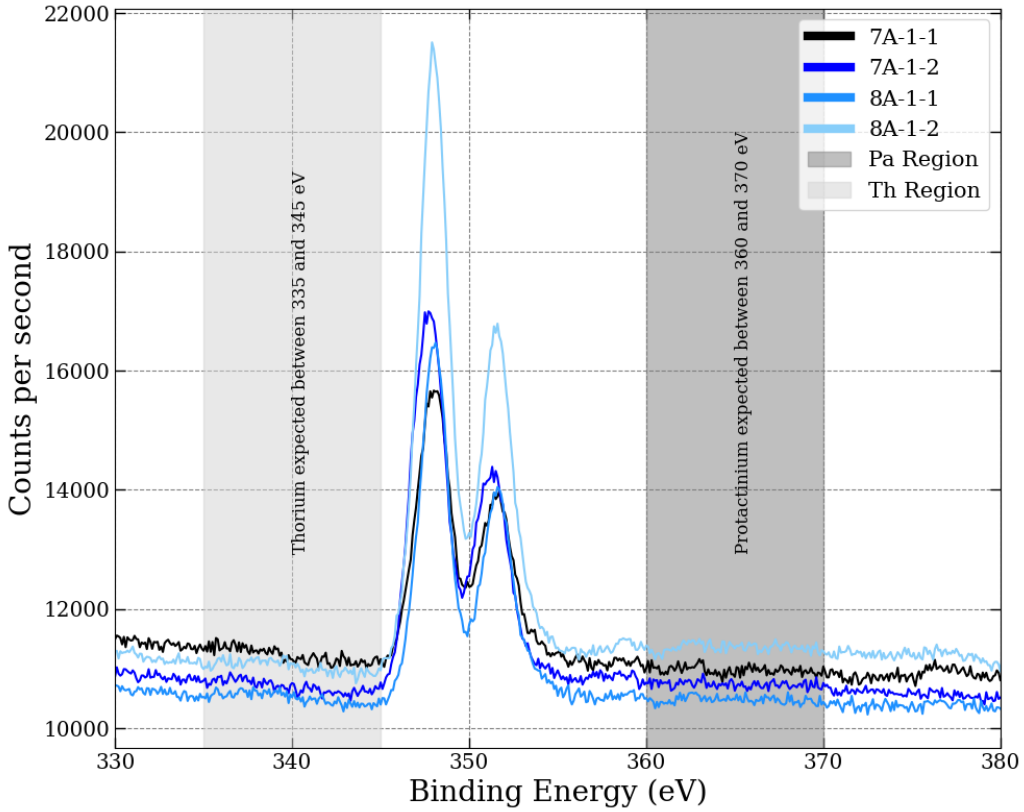

Figure 6.20: Enlarged Ca scan, indicating regions in which Th and Pa would be present if detectable. Neither actinide was determined to be detectable above background counts.

6.3.3. LIMITATIONS OF PREVIOUS LITERATURE FOR XPS PURPOSES

The search for actinide products utilizing XPS relied heavily on the available data on the present materials, as combinations of materials or compounds can significantly alter the binding energies observed. Previous literature was available using an XPS setup in which pure or oxide compounds were analysed to determine binding energies of the actinides that were examined. Unfortunately, a limitation was present within the search due to the availability of accurate data for the specific use case of this research. While it is possible that the actinides are in pure or oxide compound form as the exact properties of the material are unknown, it is much more likely that the actinides are in fluoride form, leading to different binding energies for the elements. While it is possible the materials were in such insignificant concentrations that they were not picked up at all, it is a possibility that the difference in binding energies between fluoride and oxide based compounds led to the actinide regions not being in the area that was observed. Future research isolating the binding energy ranges for the actinides

could be performed to better identify what regions they would be expected in, to better quantify the elements in the future.

6.3.4. SIMS ANALYSES

While previous data from SIMS indicated the deposit was high in F content and was likely composed of uranyl and iron fluorides, the presence of actinides would further confirm the presence of uranium, and the likelihood of radiation damage beneath. If counts were high enough for actinides, quantification and ratioing of isotopes would provide enrichment estimations, but would require consistent identifiable peaks over the control tests.

The data from multiple scans of the samples, as seen in Figure 6.21 indicated increased signal count for peaks associated with the isotopes in question in sample 7A-1-1 (water washed). While sample 7A-2-2 (ethanol washed) indicated heightened peaks, the water washed sample exhibited similar count rates and peak shapes to the data from the control sample, indicating the lack of of radioisotopes present that would have been contributed by, or held within the fluorides in the outer deposit layer. The increased F composition reported in Section 6.2.6 was consistent with what was observed in the actinide peaks, with the peaks present in sample 7A-1-1 possibly being contributed by the radioisotopes being investigated.

From Figure 6.21, it was clear that there was both a peak present slightly above the expected atomic mass (roughly 0.2 amu above), as well as a heightened signal output for isotopes such as ^{238}U, right at the expected atomic mass. Specifically for ^{238}U, the peak structure of the output centred on 238 amu was consistent across all three data sets, with the ratio of the peak in sample 7A-1-1 being much more prevalent. This could indicate the presence of ^{238}U in low quantities remaining on the surface after washing.

The peak slightly above the expected mass unit, while it potentially could be the isotope in question, would be due to a slight miscalibration of the mass to charge ratio of the data sets and would result in all signals being slightly shifted. If that were to occur, the peaks for all isotopes expected would be slightly offset, to account for the difference in mass, with peaks at lower masses being less offset. Additionally, if the isotopes were accurate to what was expected, it is unlikely that ^{235}U would be detectable due to the background noise, and the much lower concentration within the UF_6 sample held in the

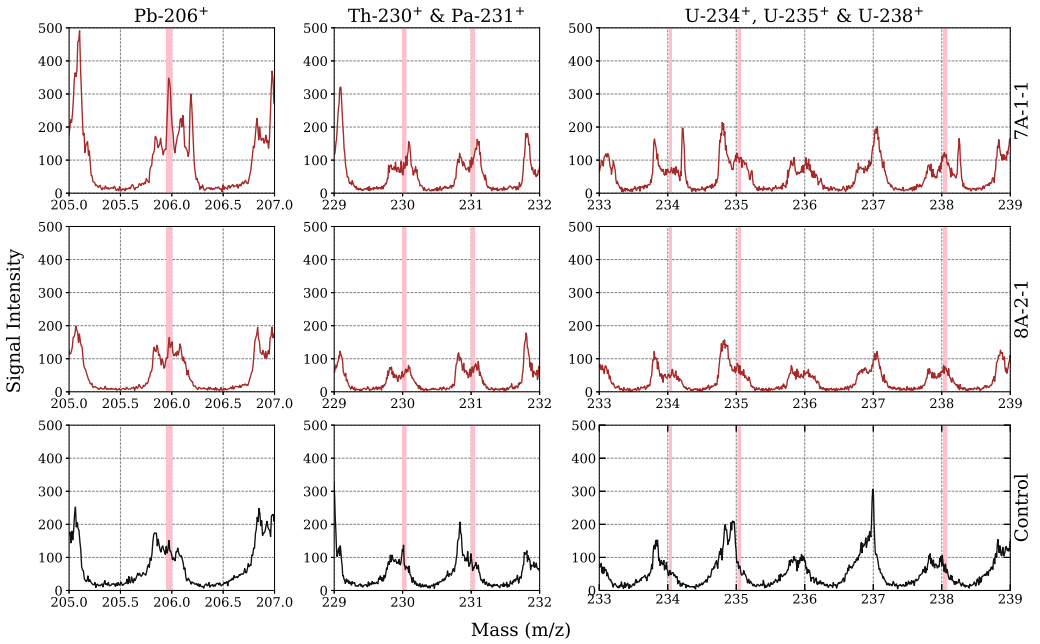

Figure 6.21: ToF-SIMS output showing masses for ^{206}Pb, ^{230}Th, ^{231}Pa, ^{234}U, ^{235}U and ^{238}U. Peaks were indicated on isotopes expected in higher quantities in sample 7A-1-1.

cylinders. As can be seen in Figure 6.21, additional peaks were identified for ^{206}Pb, ^{231}Pa, ^{234}U and ^{238}U. The isotopes other than ^{231}Pa would be expected to be observed if the peak was relevant, but the composition of Pa should be low enough due to its place in the ^{235}U decay chain to not be detectable without the parent. As such, all of the peaks in question could be due to contamination by an outside hydrocarbon or other molecule, and are present due to the surface's exposure to air over long periods or could be due to additional molecules present in the outer fluoride surface.

If ^{238}U were to be detected, it would be likely that other molecules such as UO_2F_2 would also be identified in visible amounts, which was not the case for any of the samples identified. Examination of other mass to charge ratio ranges relevant to uranyl fluoride compounds did not indicate significant peaks present, or any heightened signals over baseline control sample values. The lack of other peaks leads to two possibilities in which fluorides would be detected, but not any radioisotopes, with those being: i) the uranium bearing compounds were dissolved, leaving fluorides or ii) the tested location did not analyse an area which fluorides were present. Due to the heightened fluoride composition, in all samples, possibility ii is less likely to have occurred, and it was instead the dissolution of uranium compounds from the surface. As discussed within Chapter 5, both samples were washed in ethanol at

one point, to remove the machining oils used in the preparation stages. While this was initially thought to be a non factor due to the very visible orange and yellow colouring on the outer surface, the solubility of uranium fluorides, especially UO_2F_2 is well known. This indicates that the uranium compounds in the fluoride rich outer layer were dissolved during initial cleaning attempts, before the water washing occurred on the secondary sample. This would explain the lack of uranium detectable in both samples over the baseline, and would prevent any expected materials from being detected. While the lack of clear radioisotope peaks present could be due to a low overall composition, the high F ratio leads to the likely conclusion that the uranium bearing compounds were previously dissolved in early cleaning attempts.

6.4. DISLOCATION LOOP PROPAGATION

6.4.1. TEM ANALYSES OF CONTROL MATERIAL

To make a comparison and quantification of dislocation propagation between radiation influenced samples and base material, a control analysis had to be performed on a centre cut sample, isolated from the effects of α particle interactions. This would provide a baseline comparable on the quantity and structure of dislocations within the material, while allowing identification of any significant radiation induced effects that may be present such as amorphization or re-crystallization of the material, or the propagation of dislocation loops and interstitials. The control sample, a piece of material taken from the side of a sample that was not exposed to the atmosphere, UF_6 or any radiation damage, indicated consistent dislocations throughout the material, with several phenomena often observed in steels present.

As can be seen in Figures 6.22 and 6.23(a), significant dislocations can be observed in the sample surface with the general form of dislocations being line dislocations, which can often be caused by plastic deformation, and could be increased by sample preparation methods. While macroscopically, the dislocations present in the material are wide ranging, the dislocations are constrained to line dislocations and the overall structure of the material is consistent with few stacking fault dislocations observed throughout the material. As can be seen in Figure 6.24, the overall atomic structure and grains of the material are consistent with little variance in the direction observed. Even the struc-

ture located around the larger dislocation does not indicate any stacking faults and the overall lattice is observed to be consistent. This indicates the overall dislocations in the lattice are more likely to have been caused by deformation of the material instead of outside influences, such as radiation damage or inherent defects within the material. Many of the TEM images taken of the control samples indicated similar results with a consistent structure noted, and the major damage form being the presence of line dislocations, with visible branching. The overall defect concentrations in areas such as that observed in Figure 6.23(a) indicate low microscopic defect propagation.

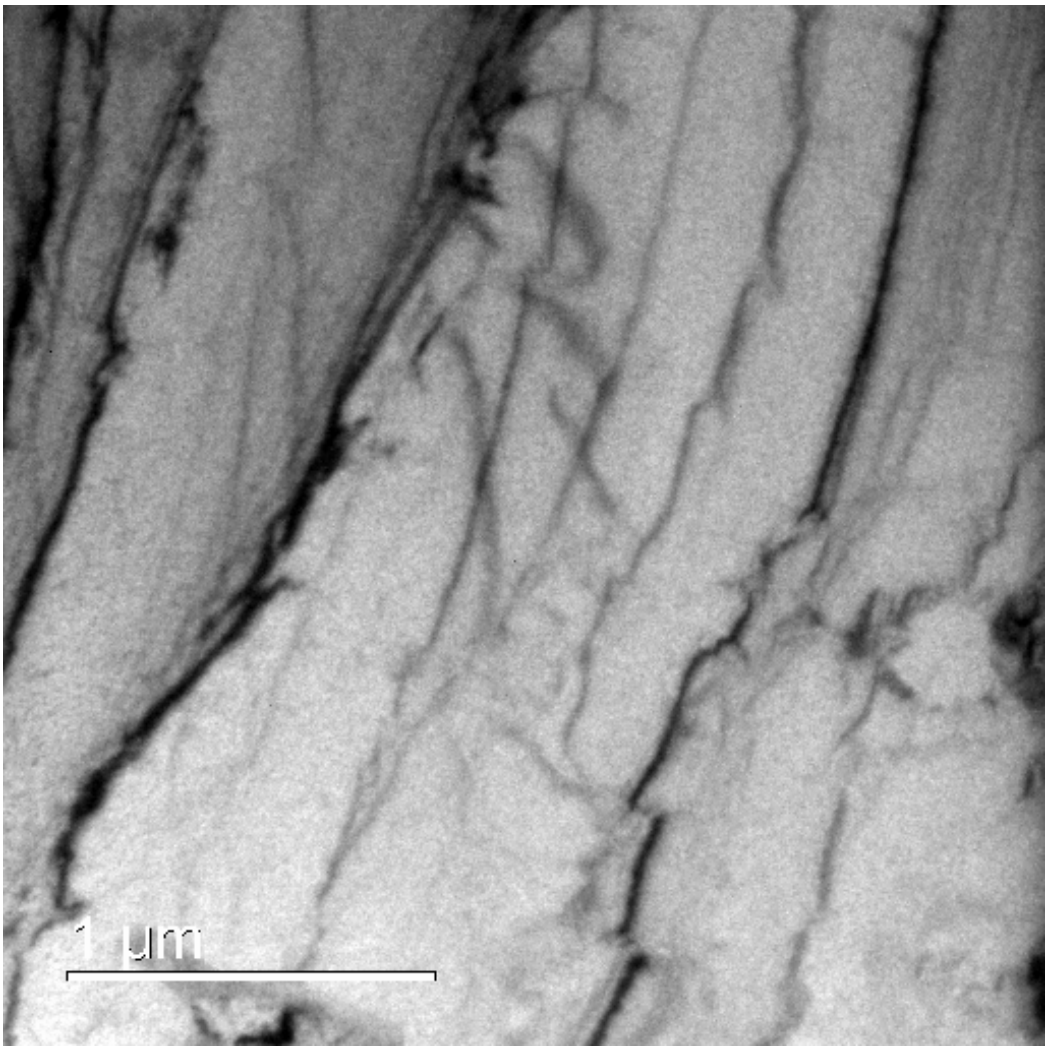

Figure 6.22: Low magnification TEM image of control sample indicating dislocation lines and branching dislocations.

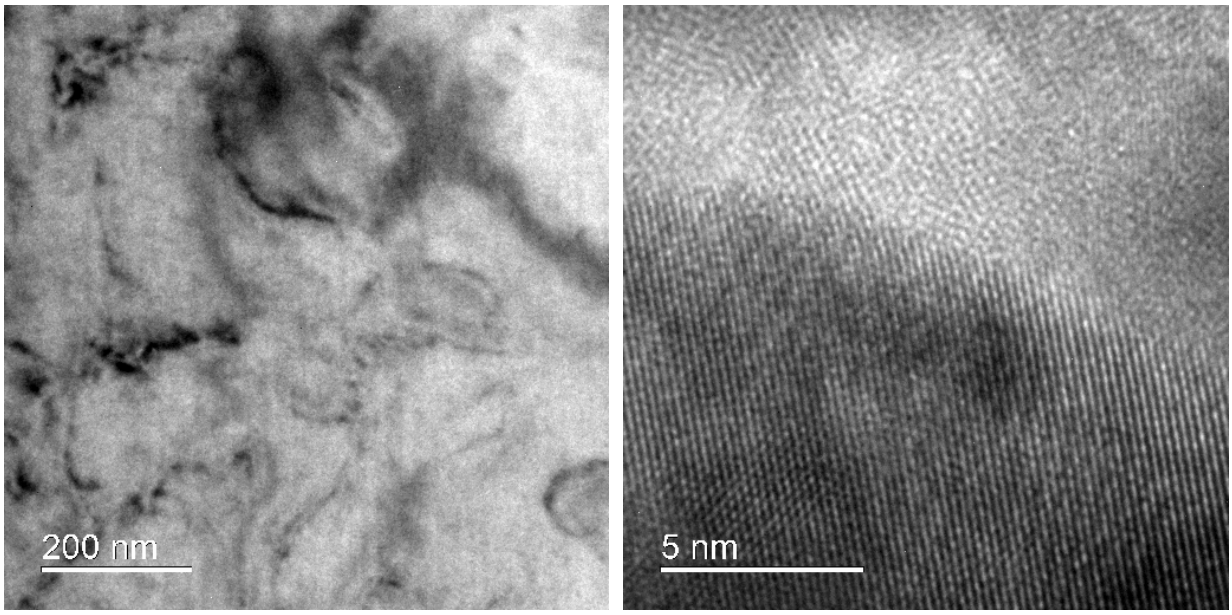

(a) TEM image of control sample showing dislocation consistency.

(b) TEM image showing various lattice directions.

Figure 6.23: TEM images with similar scales of (a) Control sample, (b) Radiation damaged sample.

6.4.2. TEM ANALYSES OF INNER METAL SURFACE

The TEM analyses performed on the inner metal material at a maximum of 100 nm from the deposit metal boundary interface, indicated significant dislocations propagated through the material. Low magnification images taken indicated a higher dislocation concentration than was observed in the control sample, as can be seen in Figure 6.25. The overall patterns and spread of the dislocations in the area were much more concentrated, indicating it was likely that the material had a higher overall dislocation count, and therefore had been influenced by an outside source.

The structure of the material was not amorphous, as was a possibility when dealing with oxides and fluoride materials, and was found to adequately be able to contain and propagate defects throughout the structure. As can be seen in Figure 6.26(b), a structured lattice was observed throughout the image, with multiple directions being noted. This was unlike the control sample that displayed very little variance in lattice direction.

Several regions of interest were noted within the TEM observations, with areas displaying stacked fault dislocations, leading to varied lattice directions after vacancy and interstitial dislocations had impacted the atomic planes in the structure. The presence of vacancies causing an impact on the lattice

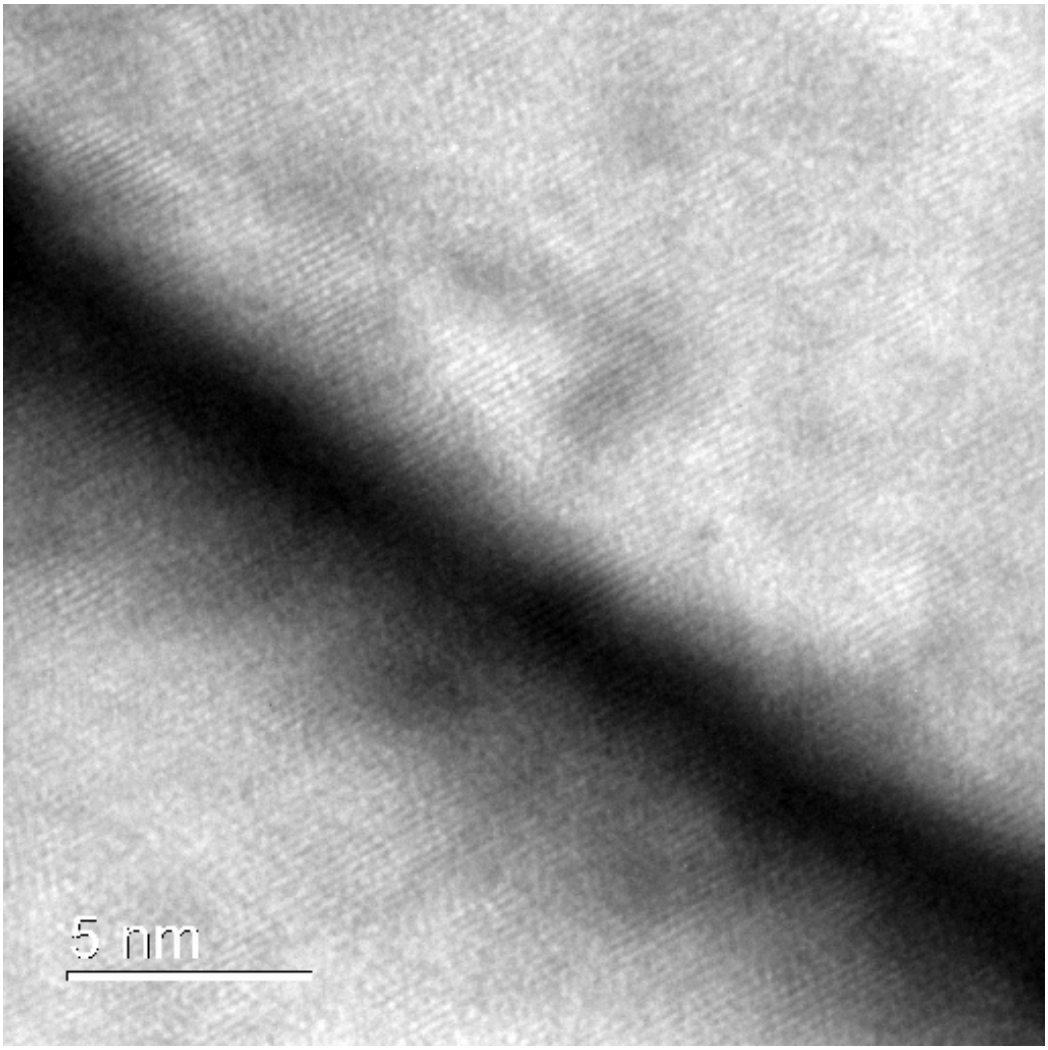

Figure 6.24: TEM image of area around line dislocation in control sample. The structure around the dislocation was consistent in size and direction.

was observed, as well as the clear occurrence of several stacking faults across the images analysed. As can be seen in Figure 6.27(a), several stacking faults were identified, impacting the direction and consistency of the structures, causing the planes to become non-parallel. These dislocations are often caused by the introduction of vacancies and interstitial dislocations into the lattice, causing the movement and offset of atomic planes. Due to this, it is more likely that the impacts of radiation may have influenced the growth of dislocations such as the ones observed. The effects were also noted in Figure 6.27(b), where the faults were much more clear with the vacancy dislocations present, and the directionality of the planes being altered. Breaks can be seen in the planes, an indicator of stacking fault dislocations, a common outcome of radiation based interactions with the atomic lattice.

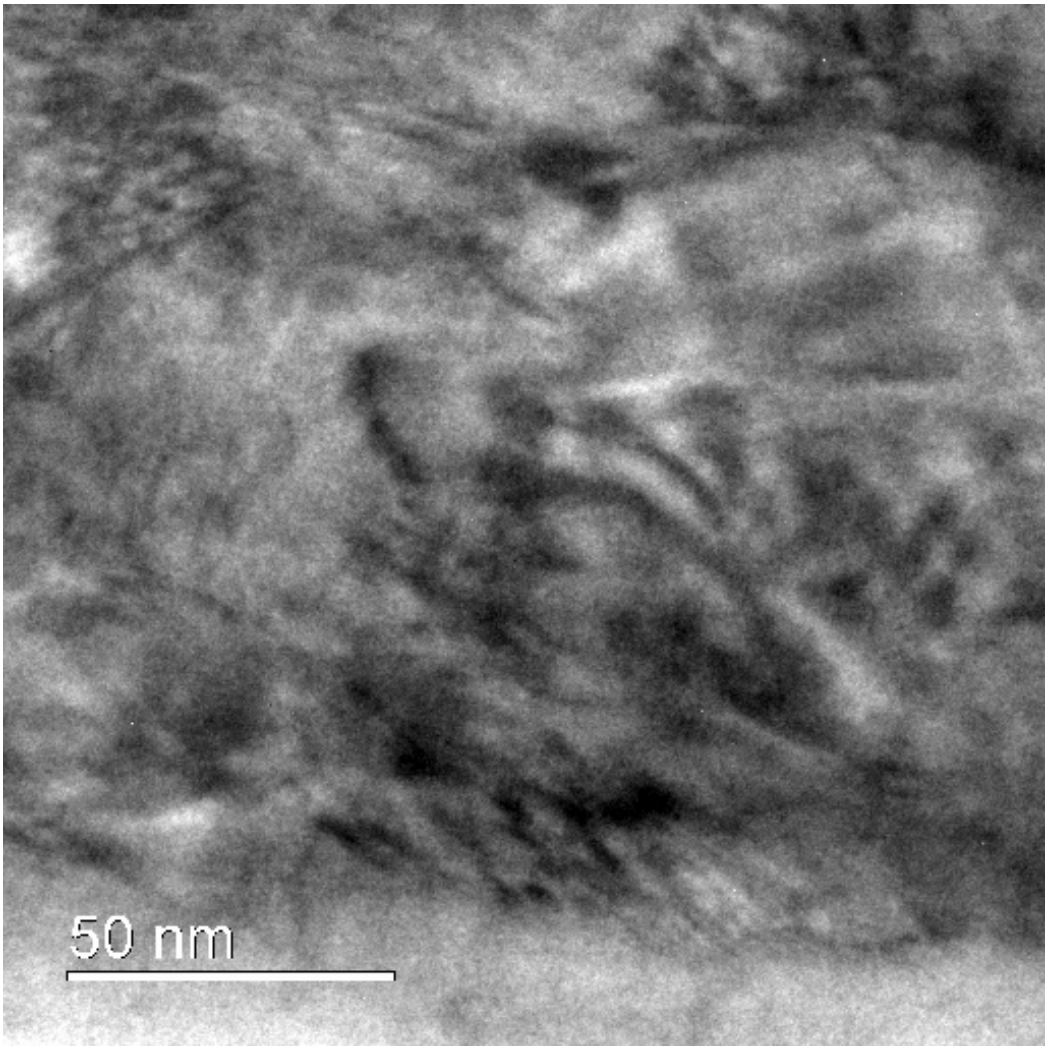

Figure 6.25: TEM image indicating general dislocation propagation through the surface. Overall dislocation concentration was observed to be higher than that of the control sample.

The results of TEM investigations indicated that through a qualitative analysis, the dislocations observed were much higher in concentration, especially when observed around larger structures, in which the atomic lattice was much more severely impacted by dislocations, such as stacking faults and the introduction of vacancies and interstitials. While the control sample indicated a large number of dislocations, the presence of line dislocations is much more likely due to the sample preparation methods, as the use of a drill press, and precision cutter would likely apply stresses to the outer edges of the samples, therefore causing plastic deformation and the production of dislocation lines. The results indicate that it is likely that the number of dislocations within the first 100 nm of the surface are significantly increased, without being in the prime area for nuclear stopping to have occurred.

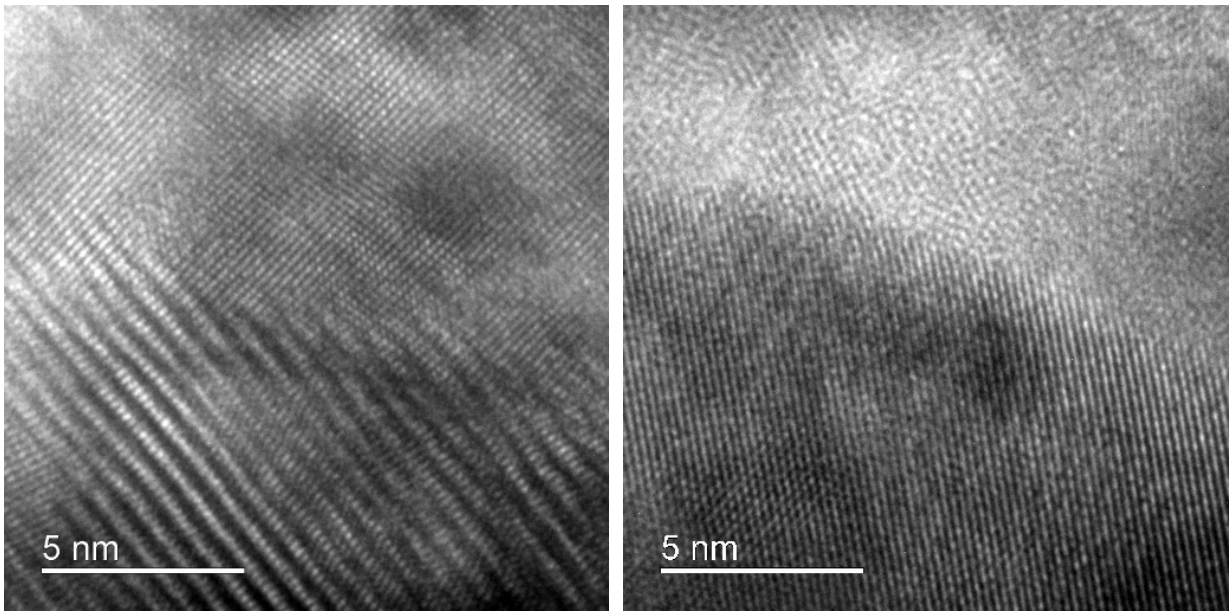

(a) Formations less than 1 nm in width.

(b) TEM image showing various lattice directions.

Figure 6.26: TEM images of radiation influenced sample, showing different lattice directions and formation of ribbons.

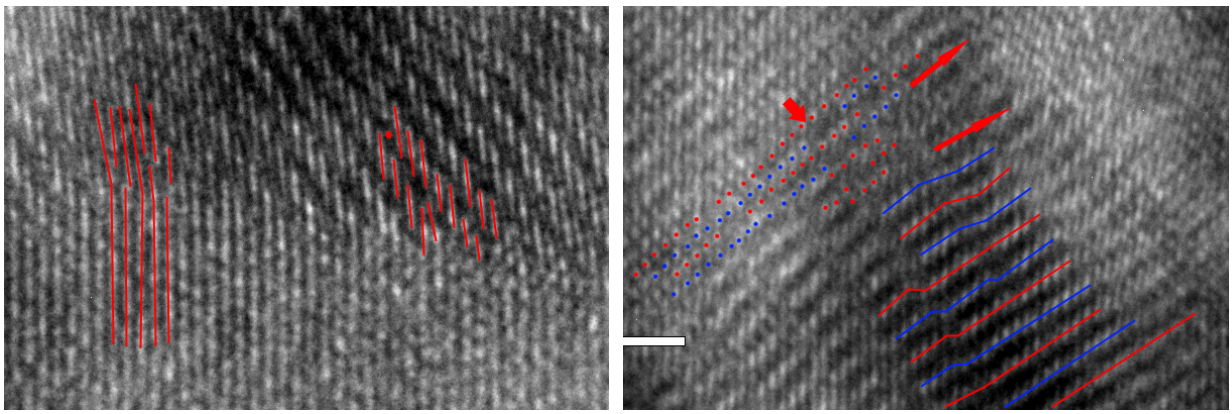

(a) TEM image indicating several stacking fault dislocations.

(b) Vacancies (arrow), and stacking faults were identified.

Figure 6.27: TEM images indicating stacking faults, and the presence of vacancies and interstitial dislocations.

From the heightened concentration, it is likely that the dislocations at a depth of roughly 20 µm would be greater, and helium implantation into the lattice would likely have also occurred. Overall, the use of TEM indicated qualitative analysis of the radiation induced dislocations was possible and a clear gradient was observed between the control sample, and the sample exposed to α particle radiation effects.

6.5. POTENTIAL STORED ENERGY RELEASE USING FLASHDSC

6.5.1. VARIOUS HEATING CYCLES AND EXPERIMENTAL SETUPS

Completion of FlashDSC indicated a distinct artifact within the first heating cycle of the DSC output, which would be expected if some form of surface material damage was present. This indicated the surface was undergoing some form of chemical change, or the annealing and removal of stored defects. As can be seen in Figure 6.28, the heating and cooling cycles observed were consistent with the exception of the first heating cycle. The first cycle indicated an initially lower heat flow into the sample, before significantly changing slope at approximately 180 °C. The slope change indicated the presence of a phase change, or release of stored energy, which would indicate radiation damage being annealed out. The slope temperature was found to be consistent with results from other materials utilizing the same method [15, 16]. To isolate the effects, a comparison could be made to the enthalpy of the peak in comparison to other well known phase changed and chemical interactions relevant to the materials in question.

To further investigate the first heating cycle, the phenomena had to be confirmed as real by ensuring it was consistent in value and spacing, for which an additional 4 experiments at different heating rates (10 °C/s to 500 °C/s) were performed. The resultant first heating curves can be observed in Figure 6.29, in which it was observed that utilizing a heating rate of 50 °C/s provided a middle ground, in which the definitive peak wasn't lost due to the higher rate, and the peak wasn't hidden in the inherent machine signal noise at lower rates. Additionally it was observed that with higher heating rates, the temperature at which the change was most prevalent increased, which was consistent with previous results [15, 16].

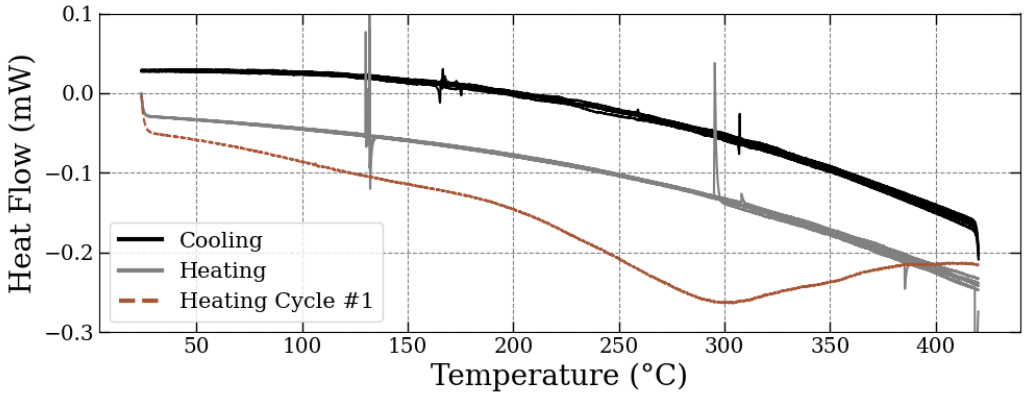

Figure 6.28: FlashDSC results from the 50 °C/s experiment, indicating the difference in first heating curve from the following heating and cooling curves.

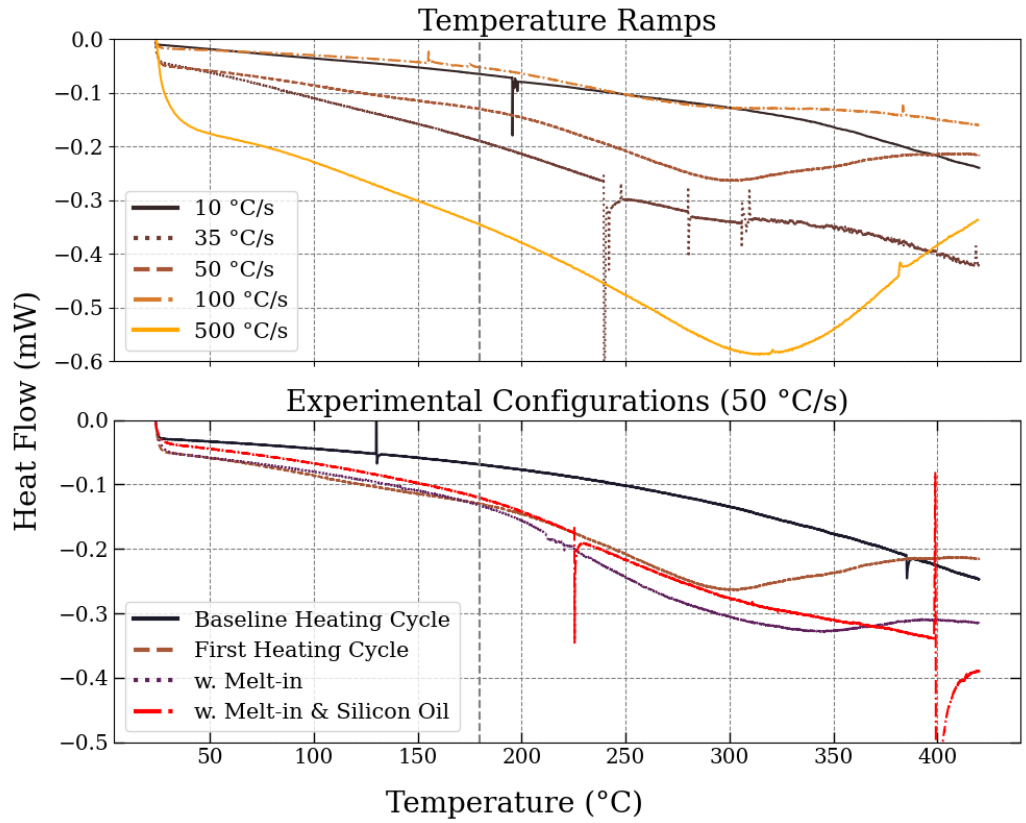

Figure 6.29: FlashDSC results from the various experimental methodologies utilized to both confirm realness of the first curve, and identify optimal conditions. The first curves were found to be consistent for a stable heating rate, with a slightly changed tail based on use of silicon oil.

6.5.2. DSC OF FIRST HEATING CYCLE

After confirming the best heating rate for use with the material, additional experiments were performed to determine whether impurities or thermal contact of the sample with the microchip had a significant effect on the observed curves. The material likely had impurities such as moisture that may have been causing unwanted curve effects, which had to be removed. For this, five melt-in cycles were utilized, as described in Chapter 5, in which the samples were heated to remove impurities below the annealing temperature. The resultant curve was observed to be similar in shape to the 50 °C/s experiment with a tail shape similar to the base-line curves.

Additionally, it was possible that the reduced thermal contact due to the powdered form was leading to the peaks observed, and to reduce the possibility of such, silicone oil was added to increase thermal conductivity throughout the sample areas. A single droplet was added to the microchip before placing the sample on the surface to increase the thermal contact of the material with the chip, to hopefully isolate any potential conductivity effects. As can be seen in Figure 6.29, the introduction of both the melt-in cycles, and silicone oil on the surface of the chip displayed the same curve shape, and did not introduce any significant curve change effects. This indicated the thermal contact was adequate, and any impurities present were not the cause of the curve observed. Several FlashDSC experiments indicated the lack of a significant peak, and were excluded from the results due to the inability to retrieve data. Additionally, experiments such as the 500 °C/s did not indicate a significant peak curve start and end period, and as such would not provide confidence in the temperature intervals analysed.

6.5.3. STORED ENERGY RELEASE CALCULATIONS

After estimation of the release of energy in kJ/mol and comparison to literature values for phase transitions, it is clear that even with a low molecular mass taken, the released energy was much higher in magnitude than that of a melting phase transition. As can be seen in Figure 6.30, even being conservative with the use of a high mass 1000 ng sample, and a low atomic number (55.8 amu), the results are slightly higher than that of a phase transition for the relevant transition temperature. For viewing purposes, the three values from each experiment, for the estimated molecular masses was averaged to produce an upper and lower bound. The bounds were then used as an upper and lower error limit. Individual data points for the results from the FlashDSC experiments can be seen in Figure 6.31, with

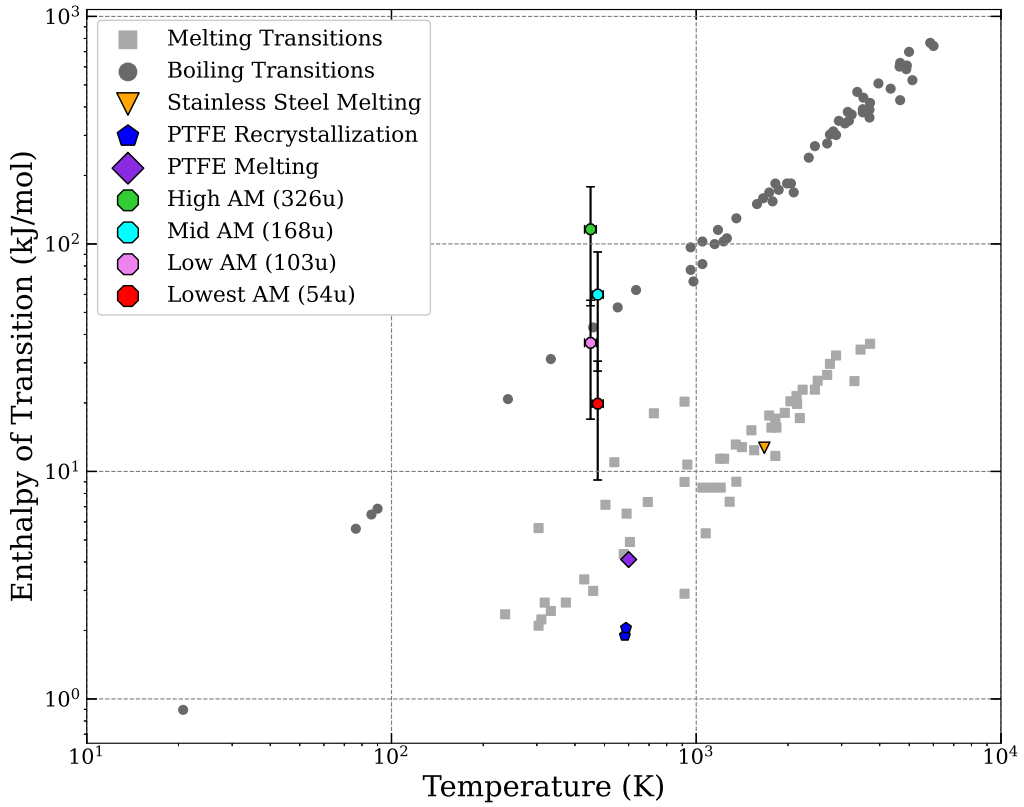

Figure 6.30: Comparison of determined potential energy ranges to melting and boiling phase transitions, as well as previous literature for stainless steel transitions, and PTFE re-crystallization after irradiation [15, 51–53].

the individual experimental data curves utilized. The temperature error of the points was selected as 20 °C due to the inaccurate measurements of the onset point of the peak, and due to how the peak was slightly offset with increasing heating rates.

Had the material been a higher molecular mass, much like some of the middle transition stages in the corrosion process, the value would instead be expected to be closer to two magnitudes higher in value than other melting transitions. The results, along with the lack of a peak present in the 2nd through 6th heating and cooling cycles suggests that it is extremely unlikely that a phase transition was present, leaving a number of phenomena left to cause the peak curve change.

While it is unlikely that a non-permanent phase transition occurred, there was potential for a phase transition from a radiation induced non-stable phase into a more energetically stable phase due to the heightened temperature. Additionally, the release of stored defects through annealing of the material may have occurred, indicating radiation induced defects, or the propagation of defects within the

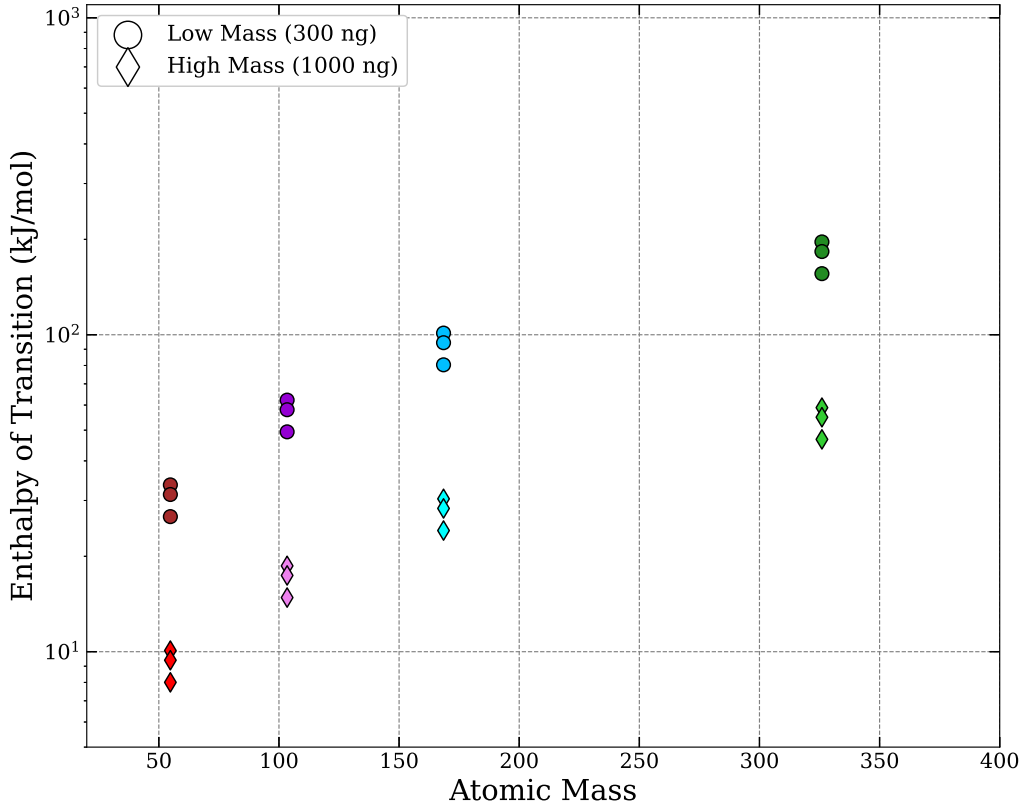

Figure 6.31: Comparison of all FlashDSC experimental results from this work against the estimated molecular mass data. The upper and lower bounds from the three valid experiments, for all molecular masses is presented.

Table 6.1: Final estimations for stored energy release.

Molecular Mass Group	**Low Energy Bound [kJ/mol]**			**High Energy Bound [kJ/mol]**		
	Base Exp.	Base Exp. #2	w. Melt-In	Base Exp.	Base Exp. #2	w. Melt-In
Highest (1)	115.3	107.5	91.5	384.2	358.3	305.1
High (2)	58.9	54.9	46.8	196.3	183.1	155.9
Medium (3)	30.4	28.3	24.1	101.2	94.4	80.4
Low (4)	18.7	17.4	14.8	62.2	58.0	49.4
Lowest (5)	10.1	9.4	8.0	33.6	31.3	26.7

outer material layer. Finally, a chemical reaction or interaction may have occurred within the surface due to the heightened temperatures, allowing a chemical reaction to occur with the introduced energy. While it currently is not possible to eliminate any of the remaining possibilities due to a lack of literature on the subject, and additional experiments being required, the potential for the outer surface to contain a radiation signature is significant. Due to the energy release being in the correct magnitude, and not lower than a phase transition, as well as the previous radiation signatures as described in Connick *et al.* [15], it is possible for the observed release to be radiation induced in nature.

The final bound estimations can be seen in Table 6.1, where each higher and lower bound for estimated energy of grouped molecular masses can be compared.

7

DISCUSSION

This chapter discusses and compares the results obtained in this work, determining the analysis methods that have hopeful use for future nuclear forensics research, and the methods that were found to not provide significant characterization data. Each section summarizes a type of characterization, and explains the main strengths and weaknesses found.

7.1. MICROSCOPY ANALYSES

The use of low magnification microscopy based methods was limited to verification that sample preparation did not overly damage the outer layer of the samples, or cause the loss of obfuscation of any radiation damage signatures. While characterization methods such as optical microscopy and SEM provided valuable results regarding the corrosion of the outer layer, and the potential growth of the surface deposition, its use in forensics based research is limited due to the limited ability to see micro-scale changes in the structure of the material, and the inability to differentiate the uranium bearing compounds on the surface. As was seen in Figures 6.8(a), 6.8(b) and 6.9, the differentiation between the deposit layer and the metallic layer underneath was possible, and provided valuable information

used to characterize the composition and layers of the surface in combination with later analyses. When used in combination with the optical microscopy results, which allowed visualization of the surface height, and the colours of the surface materials, it was expected that the deposits on the surface were composed of uranyl and iron fluorides, matching literature [30]. As was seen in Figures 6.2 and 6.5, a clear distinction in colour was observed between the deposits and underlying surface, which was seen to be almost green in colour. This helped confirm the presence of fluorides, and gave direction for future analyses. While the methods did provide valuable data for the research performed, its continued use for later characterization, or using the methods as a step to differentiate radiation damage quantities and estimate uranium enrichment is very unlikely due to the accuracy and magnification limits of the instruments.

After the low magnification instruments had been tested, the samples at UofT were prepared with a FIB to undergo analysis with a TEM. The much higher magnification of the TEM, allowing the observation of atoms within the material, and subsequent dislocations within the atomic lattice were posited to be able to qualitatively analyse the radiation damage currently, and have future use in quantification after additional research. After initial analysis on the control sample, which indicated large line dislocations on the inner surfaces of the sample, it was clear that radiation induced dislocations would be clearly visible if the α particle received fluence was high enough. Analysis of the dislocations on the control sample, as shown in Figures 6.23(a) and 6.24, indicated a very consistent atomic lattice, with clear directionality observed, and little to no amorphization of the material. This confirmed little damage to the lattice was caused due to the sample preparation methods, and provided a solid base for future comparative analysis to the potentially radiation damaged sample.

Analysis of the images produced of the non-control sample indicated significant dislocations and defects present within the material with large areas of dislocations observed in Figure 6.25, which in comparison to the control sample was significantly more damaged. While non-confirmatory, the higher damage concentrations was hypothesized to be due to the radiation damage from α particles. The likelihood of dislocations being increased due to radiation interactions was increased after observation of the atomic lattice around the larger macro structures, as the presence of stacked fault dislocations was a potential indicator of radiation damage. While the dislocations do have other causes, the lack of stacked fault dislocations in the control sample and the overall lack of other features such

as the ribbons observed in Figure 6.26(b) indicated the surface of the sample was more damaged than the control. While this could have been due to environmental factors, and the overall heightened exposure of the material to corrosion and other damage mechanisms, radiation damage was a potential cause. The presence of heightened dislocations in the outer layer were also consistent with what was observed in other characterization methods (such as FlashDSC), and gave confidence to the presence of stored energy release within the first heating curve, as the dislocations were annealed.

The dislocations in the surface were clear, with very obvious stacked faults visible in Figures 6.27(a) and 6.27(b) where the atomic planes became non-parallel, and non-linear in certain areas as the planes were pushed due to the presence of interstitial and vacancy dislocations. The same dislocations were not seen in the control sample, at least in the images taken, which is not absolute due to the nature of TEM. For higher confidence in the lack of dislocations in the control sample, significantly more analyses would have to be performed to get a dataset closer to being representative of the whole sample. In addition to the dislocations, the presence of non-linear grains observed in the damaged sample was also observed, as the control sample indicated consistent directions of the atomic planes and an overall consistent surface. Localized re-crystallization or alteration of the atomic lattice could be caused by radiation damage, and would have high concentrations in the outer surface, where significant α particles would have passed through or interacted with the lattice. While TEM data is never confirmatory due to the large data set required, the varying grain directions and boundaries have potential to be caused by localized radiation damage.

The dislocations present in the potentially damaged sample in comparison to the control sample is strong evidence that radiation damage from UF_6 was present in the outer layer, and that steel materials have promise as forensics information carriers. From the images available from the analyses, the dislocations observed were clearly much higher in the surface sample, indicating some source of heightened dislocation propagation, in which radiation damage is a strong candidate. Future research could be performed on the area to better isolate the potential effects now that the surface is better understood, and higher sensitivity analyses and sample preparation methods could be utilized to improve future results. The results indicate high magnification microscopy as a valid method for future research that seemed to have promise as a potential characterization method for uranium enrichment determination in the future.

7.2. COMPOSITIONAL ANALYSES

7.2.1. SELECTION CRITERIA FOR ANALYSES

There are a number of important isotopes for this work when considering the ^{238}U and ^{235}U decay chains for both α particle production and isotopic concentration analysis means. Half-lives for decay products in the two decay chains range in magnitude from fractions of a second to hundreds of thousands of years, indicating certain isotopes are much less likely to decay at a given time, or be present within an isotopic analysis [1]. As can be seen in Figure 7.1, a majority of isotopes within the chains had a relatively low half-life, that being below 1 year, whereas 5 isotopes were identified that had longer half lives [1]. These consisted of ^{234}U, ^{231}Pa, ^{227}Ac, ^{226}Ra, and ^{230}Th. From this selection, ^{234}U was not significant due to the inability to distinguish it from ^{238}U and ^{235}U through conventional compositional analysis methods, withstanding mass based analyses. Due to it's position behind ^{230}Th, and lower half-life, ^{226}Ra was excluded as an option as the results would likely be less significant than other isotopes. The same reasoning was selected for ^{227}Ac, although fewer options for measurement indicated ^{227}Ac should be additionally checked, for confirmatory purposes. As such, the isotopes best suited for compositional analysis included ^{231}Pa and ^{227}Ac for the ^{235}U decay series, and ^{230}Th for the ^{238}U decay series. These isotopes gave a wide range of masses while providing long half-lives for compositional means. For radiation count based methods, it is likely that a β emitting isotope would be better suited due to the difference in penetration depth and identified half-lives [1].

In addition to the list of actinides identified for compositional analysis, He would also be present in high levels in the outer surface due to implantation of the α particles after nuclear stopping had caused enough energy loss for total stopping of the particle. For most analytical purposes, the α particles would be identical to He, with the absence of 2 electrons. While He is difficult to detect with many analysis methods due to the element's high ionization potential, making it much more difficult to identify with many mass based spectrometry methods, ToF-SIMS could potentially detect He in the outer surface. If He were to be detected, the areas in which radiation damage had been sustained could be identified, and correlated with later results such as TEM analysis of dislocation loops, and the calorimetric data obtained through FlashDSC.

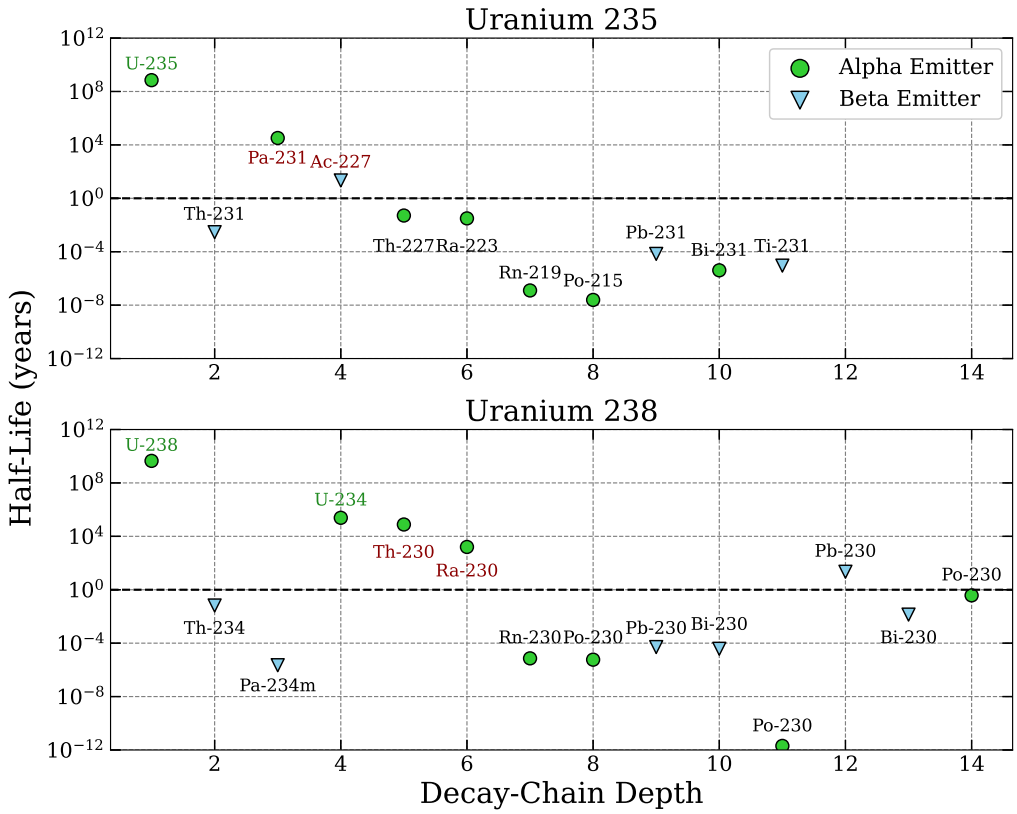

Figure 7.1: Comparison between ^{238}U and ^{235}U decay series, indicating α and β emitters, and their relative half-lives. Three isotopes were identified that were significant to the analyses performed. [1]

7.2.2. COMPOSITIONAL CHANGES

Using both XPS and ToF-SIMS as compositional analysis techniques, investigating the material surface through both chemical bindings and mass based spectrometry provided significant data for the overall compositional change, and presence of outside contaminants. The composition of A516 Grade 65 steel is given in Table 7.1, in which a number of elemental inclusions are listed, with their estimated percentage. The results from XPS indicated a significant increase in common contaminants such as silicon and carbon (common due to hydrocarbon contamination), as well as an increase in fluorine, indicating interaction of the surface of the alloy with the UF_6. The compositional percentage of fluorine was found to be in the range of 5 - 10%, indicating a significant increase in the presence of the element, with the expected method of introduction being interaction with uranium compounds. Due to this increase, it was likely that uranium would be present on the surface of the samples in some form, whether that be UF_6 or a uranyl-fluoride compound. As will be discussed in Section 7.2.3, while

Table 7.1: A516 Grade 65 Composition vs. Observed Results

Element	Alloy Composition (wt%)	XPS Composition (at%)
Fe	Fill	N/A
Mn	0.9 - 1.5	1
Si	0.4	2 - 3
C	0.08 - 0.2	20 - 25
F	0	5 - 10
Ca	0 - 1.5	1 - 2

detection of actinides was difficult with XPS, the identification of fluorine increased confidence in the later ability to find uranium deposits on the surface.

Other than the increased presence of fluorine on the surface, there were no major compositional changes noted that would indicate radiation damage markers through XPS analysis. Determining the uranium content of a low enriched sample would likely be impossible with the current XPS instrumentation available due to the low compositional presence, and the knowledge gaps associated with the binding energy of actinide compounds in fluorine bound states.

7.2.3. ACTINIDE SEARCH

Combination of EDS and SEM provided a method for determining the overall outer surface consistency and identifying any locations that were of compositional interest. The method provided a low barrier to entry sample health verification, while examining the deposits on the outer surface, and locating phenomena such as spherical growths and the underlying bare metal areas. While the EDS instrument used did not contain the elemental data required for detecting uranium and other actinide materials, it is unlikely that they would be detected due to the lower accuracy of the instrument when compared to XPS. The use of EDS as a forensics tool regarding steel materials is unlikely to bear fruit as the scale of damage caused by radiation interactions is far too small to be detected through spectroscopy or microscopy on this scale.

The use of XPS for actinide determination did not provide confident results, and the presence of Pa, Ac, and Th was not noted through the analyses performed. It is possible that the analyses did not focus on an area with the actinides present, however the increased fluorine composition indicates high fluorine interaction, consistent with what would be expected in an actinide rich area. As was seen in Figure 6.20, the areas where the actinides would be expected did not indicate any significant peak

forming, suggesting that the concentrations were below XPS detection limits. While the use of XPS for uranium enrichment determination is unlikely without a much higher accuracy instrument, what is important is understanding that actinide detection on low enrichment samples is not possible. If a sample is analysed and actinides are detectable, it is likely that the sample has undergone enough enrichment to increase the compositional percentage of actinides from the ^{235}U decay chain. If this were possible, it would provide an avenue for detection of HEU; however, at the current time, it is not certain whether that is feasible.

The use of ToF-SIMS to analyse the composition using a mass detection method instead of relying on unknown binding energies proved to be a higher reliability method for detection of radioisotopes than XPS and EDS previously had. Comparison of the data produced from the control sample, to both the samples washed in water and ethanol indicated peaks in the relative ranges expected for radioisotopes in reasonable quantities.

As was seen in Figure 6.21, a heightened peak was identified where ^{238}U would be expected in mass range. However, the peak was not indicative of the presence of the radioisotope, and could have been caused by outside contamination due to the exposure of the samples to the outside environment (e.g. hydrocarbons). The increased F to Fe ratios observed in the ethanol washed samples meant it was likely that fluorides were present in higher quantities on the outer surface of the ethanol washed sample, which would correlate to the presence of uranium bearing compounds. However, due to the previous washing of the samples in ethanol after initial sectioning during sample preparation, it is possible that any uranium was dissolved from the surface before the fluorides were both identified, and water washing occurred. As such, while identification of radioisotopes is very possible with the use of ToF-SIMS, the analyses performed may have lacked the presence of uranium before analysis was done. This could be confirmed through additional experiments in which the samples did not undergo ethanol washes after preparation, or if the deposit layer is isolated without the need to section the samples in the first place.

While the results did not allow easy detection of uranium or decay product peaks, the results show evidence of F, which would only occur due to reaction with UF_6 and the subsequent deposition of fluorides on the surface, as confirmed by the presence of very low radiation emissions. Future analyses could remove the sectioning component of the research to better isolate the fluorides and remove the

need to use water or ethanol washing in the first place.

7.2.4. USE OF COMPOSITIONAL ANALYSES FOR FORENSICS

The compositional analyses performed indicated hope for use in determining enrichment of the material through the identification of uranium and actinide materials with mass based detection methods. The use of XPS, while useful in indicating the presence of fluorine on the surface of the material, did not provide evidence of uranium within the samples. XPS did provide a low-barrier of entry method for determining fluorides with easier sample preparation than for ToF-SIMS, but likely would not provide the results needed in any realistic forensics investigation of a steel material for being in contact with enriched uranium.

Results from ToF-SIMS did indicate that the atomic masses associated with uranium and other actinide materials were possible to detect, and would provide enough accuracy to adequately ratio the components, especially in a sample with a higher ^{235}U enrichment. The samples analysed would not have had a sufficiently high enough ratio of ^{238}U to ^{235}U to identify the composition to a degree of confidence. However, if the enrichment of the uranium held in the cylinders used for this research was higher than 0.711%, it is likely that the presence of ^{235}U (and ^{236}U from re-processed samples) would reach a point of both detection and determination. This indicates that ToF-SIMS has promise as a method for the determination of uranium enrichment if scratch tests of a sample can be done to remove the outer layer for analysis. Additionally, the detection thresholds for ToF-SIMS are low enough to potentially identify ^{236}U in samples in low quantities with high enough confidence to determine when enriched material has been passed through a system. The presence of ^{236}U would heavily indicate enriched material due to its inclusion from the re-processing of spent nuclear fuels. Overall, ToF-SIMS provides a quality characterization method that provides compositional data for uranium and other actinide compounds that are likely to appear on the material surface, and contain the radioisotopes that are vital for determining the enrichment of a sample.

7.3. CALORIMETRIC ANALYSIS

The use of FlashDSC, with its reduction of sample size to a nanogram scale, allowed enough isolation of the outer surface to potentially identify radiation induced effects, even with the low penetration range

of α particles. While direct calculation of a final result relating the potential stored energy release was not possible due to the unknown material properties, estimations of the peak energy were in the predicted energy range. The heating curves of the utilized experimental data was observed to be both consistent in value and peak temperature range, and indicated the presence of a significant interaction (as isolated in Figure 6.28). Even when utilizing various experimental methods, such as various heating rates, and the use of both melt-in cycles and silicon oil to improve thermal contact, the first heating cycle was differentiable, with a clear peak present indicating the occurrence of some form of damage annealing.

The lack of known material properties regarding both mass and molecular mass of the samples increased the potential error for the performed experiments, but conservative measurements and estimations still place obtained data well above previously recorded values for phase transitions of other materials (as was compared in Figure 6.30). While the presence of radiation induced stored energy release is not confirmed through the performed experiments, the presence of a significant change in the first heating cycle, along with the lack of following phenomena in other cycles removes the potential for certain phenomena to occur. If a simple phase change were to occur, secondary cycles would indicate a similar peak shape or temperature, where as if a permanent effect had occurred, the observed peak would be likely. This indicated the potential causes of the peak were limited to the following: i) radiation induced stored energy release, ii) chemical reactions / interactions, and iii) non-permanent phase transition. Chemical interactions and reactions are possibly due to the fluorine compounds present on the surface, which have high likelihoods to react with other materials at energetic conditions. The other two possibilities, those being stored energy release and non-permanent phase changes, can be linked to radiation damage due to their initial causes. It was possible for radiation damage to induce localized phase changes to an energetically less stable phase that when heated, underwent a transition to a more stable phase. Additionally, as was observed through other analyses such as TEM and ToF-SIMS, the presence of uranium compounds on the surface, and dislocations in the outer layer indicate the presence of some radiation interactions, and the release of stored energy would be likely.

Previous literature on PTFE re-crystallization caused by radiation damage [15] indicated a stored energy release roughly one order of magnitude lower than the obtained results. Due to the lower expected energy storage ratio in plastics and polymer materials when compared to metals, the difference

in value is not impossible and the heightened results are accurate to what has previously been hypothesized. As the energy required to produce defects and dislocations in the atomic lattice is much higher for ordered lattices in metals, a higher energy release from annealing would be consistent.

While errors for the results are relatively high, the magnitude of difference to other materials even with conservative values leads to the possibility that the energy released is within an expected range for metal materials. While the possibility remains for the stored energy to be radiation induced in nature, the isolation of radiation based effects would require additional analyses with higher precision sample preparation and additional characterization of the outer material. The unknown characteristics of the surface of the samples, along with the relatively complex chemical composition and effects present introduce significant errors into the analysis, but the calorimetric data obtained provides a confident first step in quantifying radiation damage contained in the outer layer.

7.4. FINAL COMPARISONS

From each of the characterization method types utilized, there were results that were hopeful and indicated the possibility of quantifying the radiation interactions in the outer surface, whether that be direct quantification through TEM and FlashDSC, or retroactive analyses utilizing compositional markers with ToF-SIMS. For future nuclear forensics research on steel or steel like materials, the characterization methods that produced the best results were those that could detect trace amounts of uranium and other actinides, and those that could quantify defect propagation through α radiation interactions with the surface.

The improvement of sample preparation methods to better isolate the radiation affected zones would increase confidence in the currently obtained results, while continuing to remove outside error influences associated with the unknown properties of the surface and chemical composition. Each of the analyses has provided specific results for the characterization of the surface, while helping determine which analysis methods have promise for future research.

Through the analyses it was determined that due to the atomic scale of the damage, highly accurate, specific analyses are required for any quantification to occur. While low magnification, or low accuracy methods can be utilized to confirm surface health, the use of SEM, EDS, and XPS did not provide results that proved any significant radiation damage, or presence of uranium bearing mate-

rials. However, their use as a check on sample health can provide important low cost of entry data on the overall surface composition. There were not any indications of macro scale radiation induced effects on the surface, however the analyses were vital for initial characterization attempts, as overall knowledge of the surface was greatly increased. Due to the lack of results for radiation quantification, it is unlikely that those methods would provide useful data for quantification of uranium enrichment, or would be useful for supporting data in the determination of radiation damage. The use of higher specificity characterization methods such as TEM, with a much higher magnification, ToF-SIMS with a detection limit in the ppb, and FlashDSC, with detection of atomic dislocation annealing provide the best methods to determine radiation interactions in steel materials.

The use of TEM as a microscopic dislocation based method proved to be an adequate method to qualitatively compare the dislocation concentrations of the sample surface, and to identify whether smaller lattice based dislocations were occurring. The detection of a number of dislocation forms, as well as various grain directions indicated the potential for radiation based damage, which was not observed in the control samples, proving to be a viable method for giving confidence to other characterization analyses. The use of TEM, while not able to entirely confirm radiation damage in the current state, when used in combination with FlashDSC and other analyses, strongly indicated that radiation damage markers had been contained within the outer metallic surface, and provided significant qualitative results to portray radiation damage fingerprints in the material.

Compositional based analyses determined that methods that measure binding energy or x-ray release were not accurate enough to determine enrichment, but could be used to confirm the presence of fluoride based components for identifying if the sample had been in contact with uranyl fluorides. The use of a mass based spectrometry method such as ToF-SIMS provided high enough accuracy to quantify signals related to separate uranium isotope masses, as well as other actinides. Isolation of enrichment based data was found to be possible even without the distinct detection of radioisotopes, and the use of ToF-SIMS was identified as the highest accuracy characterization method for quantifying materials in the expected mass range of the samples in their current form. Continued research regarding isolation of radioisotopes from the wider sample surface for detection in ToF-SIMS would be a good direction for future research, as direct quantification of uranium enrichment would be straightforward with a higher detection quantity. Additionally, isolation of the deposit layer without stringent

sample preparation would be much easier to perform than for other methods, and would remove noise and error within the SIMS results.

The results obtained through FlashDSC, indicated a significant phenomena was occurring within the first heating curve that could indicate the release of energy stored within the atomic lattice, caused by defect propagation. While the results were inconclusive within this study regarding the isolation of radiation based effects, the presence of a distinct peak within the first heating curve, and the magnitude of the calculated enthalpy place the results firmly in the plausibly radiation damage category. As the list of current potential sources of energy release include chemical interactions and permanent phase changes, additional research could remove these from consideration through higher precision sample preparation, confirming the presence and quantification of radiation induced stored energy.

8

CONCLUSION

The use of a variety of experimental methods throughout the term of this research has reached a number of conclusions on the overall characterization of the inner surface of steel 48Y cylinders, and the material's viability for future research in the nuclear forensics field. For each of the methods utilized, valuable information on the material properties of the cylinders was obtained, and the ability for the method to be utilized in future research as a forensics tool for the determination of uranium enrichment was identified. Overall, the main objectives set forth at the beginning of the research were reached, with those being:

A Perform a proof of principle first look at characterizing how radiation damage can be quantified in UF_6 bearing steel 48Y cylinders.

B Utilize a variety of characterization methods to examine the stored radiation damage, if any, and how it can be quantified.

C Determine the viability of each method for future research, and their potential use as a forensics tool to quantify uranium enrichment through the damage signatures on the material surface.

The viability of the utilized characterization methods and their overall use in future research has been laid out below in a number of points:

1. The radiation damage signatures on the surface of the steel is very limited; any damage observed was on the nm scale with no clear macro level phenomena observed.

2. Low accuracy, low detection threshhold analyses such as Optical Microscopy, SEM, and EDS do not provide sufficient analytical data to be useful for quantification of radiation damage, but can be used to characterize the corrosion and overall health of the surface.

3. Measurement of dislocations through high magnification microscopy such as TEM provides a qualitative comparison of radiation damage, but to obtain a true quantification of radiation damage would require a significantly large dataset to have statistical significance.

4. Higher accuracy compositional analyses such as ToF-SIMS have promise in the determination of uranium enrichment through quantification of uranium and other actinide decay products. The presence of ^{235}U decay products would be indicative of enrichment, but are not visible in low enrichment samples.

5. If isolation of the damaged area is possible, the use of FlashDSC will likely provide a high accuracy method for determining uranium enrichment through indirect quantification of the dislocations present. Unlike TEM, FlashDSC requires far fewer measurements to be representative of the whole sample.

6. It is unlikely that it would be possible to determine if HEU was held within a steel container without a sufficiently long holding time due to the corrosion mechanics, and low overall fluence per unit time.

7. Finally, A516 grade 65 steel specifically has been shown to exhibit multiple damage signatures that may provide an avenue for uranium enrichment quantification, but the concepts shown within this research are likely applicable to a larger number of steel materials in use within the nuclear industry.

While the conclusions stated are the findings of this work, additional research can be done to further increase both the accuracy of the performed analysis, and further identify the methods and techniques that can accuracy quantify the contained radiation damage with high accuracy and sensitivity. The techniques utilized within this work, and the exact methodologies were found to be limited in certain areas, and a number of additional paths have been suggested for future research work in Chapter 9. Due to the proof of principle nature of this work and the low previous knowledge on the concepts and material in question, future research can significantly improve upon the suggested techniques while continuing to pursue the determination of uranium enrichment through radiation damage quantification in the hopes of producing a method of use to the safeguarding and inspections community.

9

RECOMMENDATIONS FOR FUTURE WORK

The content of this chapter details some recommendations for future research to improve the results obtained in this study, as well as the furtherment of nuclear forensics within steel materials for enrichment determination purposes. Each of the sections will detail a potential path for research to follow to fill in knowledge gaps present after the completion of this work.

Improvement on nuclear forensics techniques relies on the investigation and compilation of material characterization data to build a portfolio of materials that can be utilized for measurement purposes. By continuing to both expand the materials for characterization to be performed upon and the list of techniques with viable results will vastly improve uranium detection, and enrichment correlation capabilities.

9.1. HIGHER ENRICHMENT SAMPLES

While the results of the research led to a number of conclusions on the effectiveness of steel materials as forensics information carriers, several knowledge gaps are still present regarding the scalability of the techniques with increasing enrichment. Whether higher enrichment samples would have an effect

on the observed radiation damage markers, and if so, after how long would the effects be noticeable. Isolating the time based effects of enrichment, or the ratio of high enrichment to low enrichment use time for visible effects would improve the capabilities of the research in determining high enrichment use of the material.

As the use time of the cylinders is high compared to other common materials used in storage settings, the possibility of identifying ratios of ^{235}U after low use time, or singular flow through of the material would be instrumental in the detection of nuclear proliferation when use of this technique is considered. The contributed radiation damage to the material by ^{235}U is relatively low in comparison to the ^{238}U and ^{234}U based effects, indicating isolation of higher enrichment effects may be significantly more difficult than determining the presence of uranium or other actinides.

Accessibility of steel material samples that have been exposed to higher enrichment UF_6 would provide an avenue to better understand both the radiation damage mechanisms regarding steels, and the potential chemical interactions that may provide another avenue in enrichment detection.

9.2. RAMAN SPECTROSCOPY

To further the previous discussion, it was believed that the radiation damage could be further confirmed through analysis of both heated and non-heated samples. The analysis of such samples would further allow isolation of the radiation damage effects by observing the samples before and after annealing had occurred, to determine if phenomena such as radiation induced re-crystallization of the material were possible. Additionally, annealing of dislocations would have a much larger effect had the damage been radiation based, as the isolation of the defect area would lead to differentiable Raman results. Performing a sensitivity analysis on the bounds of heating that would affect the radiation affected zone would also improve knowledge gaps on the resistance of the forensics fingerprint to damage through exterior conditions. The ability to detect forensics data after the sample had been heated above ambient temperatures would improve detection capabilities for material.

Additionally, performing additional experimentation on the outer radiation affected zone compared to the inner, non-damaged area would help confirm any radiation based effects. To confirm the effects are caused through α radiation interactions, the outer 20 µm of material should be removed through a precise sectioning method (such as FIB), before being analyzed within a Raman

spectroscopy instrument, or other chemical binding analysis method. This would provide a baseline comparable measurement through the non-radiation damaged zone and would confirm whether effects had been radiation based or chemical interactions. As chemical effects would likely have a much higher interaction depth than the α radiation, a series of sections could be analysed to determine depth gradient effects.

Currently, it is unknown whether the outer discrepancies in the DSC curves are caused by radiation damage or other phenomena, but use of an analysis method such as Raman spectroscopy with isolation of the radiation zone would immensely improve current confidence in the results, and hopefully isolate the results through a depth gradient, possibly identifying the distinct regions at which α radiation would undergo nuclear stopping and cause defect propagation and helium impantation.

9.3. FLASHDSC OF CONTROL SPECIMEN

The FlashDSC results indicated a differentiable peak from the first heating curve, however isolation of the peak was difficult due to the lack of a baseline heating curve that could isolate effects caused by other materials in the surface. To further improve confidence in the observed peak, and remove error propagation through the analysis, additional experiments could be performed using a sandblasted sample that would have the outer surface deposit entirely removed, allowing isolation of the base metal flashDSC heating curve. This would identify if the first peak was influenced, or caused at all by the base material, and would improve results and the ability to integrate the energy released during the heating cycle.

Additional control samples would also be improved by utilizing a methodology similar to what was discussed within Section 9.2, with further isolation of the potentially radiation damaged zone. This could be done with a number of additional experiments in with FIB it utilized to section samples, which could take samples from past the radiation damaged area. This would further isolate the potential for the peak to be radiation induced, and would reduce the number of phenomena potentially causing the peak to occur.

9.4. RECOMMENDED ANALYSIS METHODS BASED ON THIS WORK

For future research, the selected characterization methods have proved to have promise for radiation quantification, and it is likely that further higher precision sample preparation and repeated measurements would further improve both confidence, and ability to quantify results. The methods of use have been shown to have the ability to differentiate signals at the required precision and accuracy for quantification from metal materials, with the expectation that additional work would remove further error sources while improving the precision of the measurements. By identifying the levels of precision required, the methods utilized can be expanded to target more specific areas, with abilities improving as knowledge of the characterization of the overall surface increases.

With that, the final recommendations for characterization of the surface regarding radiation quantification, methods such as TEM, ToF-SIMS and FlashDSC are required to detect dislocations and radiation based interactions at the accuracy and detection limits required for the low overall radiation influence in the steel, and the low penetration depth of the α particles. With the current results, it is possible that direct quantification of radiation damage can be performed, and the results utilized to calculate uranium enrichment, and the fluence received by the steel materials.

REFERENCES

[1] "The Environmental Behaviour of Radium," Tech. Rep. 476, International Atomic Energy Agency, Vienna, Austria, 1990.

[2] H. H. Rogner, "World Outlook for Nuclear Power," *Energy Strategy Reviews*, vol. 1, no. 4, pp. 291–295, 2013.

[3] "Treaty on the Non-Proliferation of Nuclear Weapons," tech. rep., Eighteen Nation Committee on Disarmament, Moscow, Russia; London, United Kingdon; Washington D.C., United States, 1970.

[4] W. Kötter, H. Müller, and D. Fischer, *Nuclear Non-Proliferation and Global Order*. Oxford University Press, 1994.

[5] *REGDOC-2.13.1, Safeguards and Nuclear Material Accountancy*. Ottawa, Canada: Canadian Nuclear Safety Commission, 2018.

[6] "Agreement Between the Government of Canada and the International Atomic Energy Agency for the Application of Safeguards in Connection with the Treaty on the Non-Proliferation of Nuclear Weapons," tech. rep., International Atomic Energy Agency, Government of Canada, 2000.

[7] M. P. Murchie and S. J. Reid, "Uranium Conversion and Enrichment," in *Advances in Nuclear Fuel Chemistry* (M. H. A. Piro, ed.), pp. 331–370, Woodhead Publishing, 2020.

[8] G. Kessler, *Proliferation-Proof Uranium/Plutonium Fuel Cycles: Safeguards and Non-Proliferation*. Karlsruhe, Germany: KIT Scientific Publishing, 2011.

[9] E. M. Saylor, A. Lang, W. B. J. Marshall, and R. Hall, "Analysis of the 30B UF_6 Container for Use with Increased Enrichment," Tech. Rep. ORNL/TM-2021/2043, Oak Ridge National Laboratory, Oak Ridge, United States, 2021.

[10] H. A. Smith Jr., *Passive Nondestructive Assay of Nuclear Materials*, ch. The Measurement of Uranium Enrichment, pp. 195–220. United Stated Nuclear Regulatory Commission, 1991.

[11] D. R. Olander, "The Theory of Uranium Enrichment by the Gas Centrifuge," *Progress in Nuclear Energy*, vol. 8, no. 1, pp. 1–33, 1981.

[12] S. Niemeyer and L. Koch, "The Historical Evolution of Nuclear Forensics: A Technical Viewpoint," (Vienna, Austria), International Conference on Advances in Nuclear Forensics, 2014.

[13] "Uranium Hexafluoride: Handling Procedures and Container Criteria," Tech. Rep. ORO-651, United States Atomic Energy Commission, Oak Ridge, United States, 1972.

[14] C. Lopez, C. Morrow, D. J. Ammerman, M.-A. Charette, and T. Korbmacher, "Thermo-mechanical Study of Bare 48Y UF_6 Containers Exposed to the Regulatory Fire Environment," (London, United Kingdom), 16th International Symposium on the Packing and Transportation of Radioactive Materials, 2010.

[15] R. C. Connick, *Assessing Differential Scanning Calorimetry as a Retrospective Dosimetry Method for the Verification of Uranium Enrichment Activities*. PhD thesis, Massachussetts Institute of Technology, Cambridge, United States, 2022.

[16] C. A. Hirst, *Quantifying Radiation Damage Through Stored Energy Released During Defect Annealing in Metals*. PhD thesis, Massachussetts Institute of Technology, Cambridge, United States, 2022.

[17] T. C. Kaspar, C. A. Lavender, and M. W. Dibert, "Evaluation of Uranium-235 Measurement Techniques," Tech. Rep. PNNL-26490, Pacific Northwest National Laboratory, Richland, United States, 2017.

[18] S. Tavernier, *Experimental Techniques in Nuclear and Particle Physics*, ch. Interactions of Particles in Matter, pp. 23–53. Springer, 2009.

[19] R. H. Müller, "Interaction of Beta Particles with Matter," *American Chemical Society*, vol. 29, no. 6, pp. 969–975, 1957.

[20] S. Zinkle, "Radiation-Induced Effects on Microstructure," in *Comprehensive Nuclear Materials* (R. Konings, ed.), vol. 1, ch. 1.03, pp. 65–98, Elsevier, 2012.

[21] G. Knop and W. Paul, "I - Interaction of Electrons and Particles with Matter," in *Alpha-, Beta- and Gamma-Ray Spectroscopy* (K. Siegbhan, ed.), pp. 1–36, Amsterdam: Elsevier, 1968.

[22] K. Daub, *A Study of Gamma Radiation Induced Carbon Steel Corrosion.* PhD thesis, Western University, London, Canada, 2013.

[23] M. Jin, P. Cao, and M. P. Short, "Mechanisms of Grain Boundary Migration and Growth in Nanocrystalline Metals Under Rrradiation," *Scripta Materialia*, vol. 163, pp. 66–70, 2019.

[24] C. A. Hirst, F. Granberg, B. Kombaiah, P. Cao, M. Scott, R. S. Kemp, J. Li, K. Nordlund, and M. P. Short, "Revealing Hidden Defects Through Stored Energy Measurements of Radiation Damage," *Science Advances*, vol. 8, no. 31, 2022.

[25] U. Fano, "Penetration of Protons, Alpha Particles, and Mesons," *Annual Review of Nuclear Science*, vol. 13, no. 1, pp. 1–66, 1963.

[26] D. Hull and D. J. Bacon, eds., *Introduction to Dislocations.* Oxford, United Kingdom: Butterworth-Heinemann, 5 ed., 2011.

[27] K. Hattar, "Deformation Structures Including Twins in Nanograined Pure Metals," in *Nanostructured Metals and Alloys* (S. H. Whang, ed.), pp. 213–242, Woodhead Publishing, 2011.

[28] S. Wu, C. Cao, H. Bo, and Q. Zhang, "In-situ Atomic-scale Observation the Escape of Irradiation-induced Dislocation Loops in Magnesium," *Journal of Alloys and Compounds*, vol. 895, p. 162708, 2022.

[29] M. Griffiths, J. Ramos-Nervi, and L. Greenwood, "A Rate Theory Model of Radiation Induced Swelling in an Austenitic Stainless Steel," *Journal of Nuclear Engineering*, vol. 2, no. 4, pp. 484–515, 2021.

[30] E. J. Barber, "Chemical Aspects of Cylinder Corrosion and a Scenario for Hole Development," vol. 25, (Oak Ridge, United States), pp. 9–20, Second International Conference - Uranium Hexafluoride Handling, 1991.

[31] R. Ritter and E. J. Barber, "Aspects of Uranium Chemistry Pertaining to UF_6 Cylinder Handling," vol. 25, pp. 3–8, Second International Conference - Uranium Hexafluoride Handling, 1991.

[32] B. Hafner, "Scanning Electron Microscopy Primer," (Minneapolis, United States), University of Minnesota - Twin Cities, 2007.

[33] Y. Leng, *Materials Characterization: Introduction to Microscopic and Spectroscopic Methods*. Wiley, 2nd ed., 2013.

[34] D. B. Williams and C. B. Carter, "The Transmission Electron Microscope," in *Transmission Electron Microscopy: A Textbook for Materials Science*, pp. 3–17, Boston, United States: Springer US, 1996.

[35] T. A. Carlson, *Photoelectron and Auger Spectroscopy*. Springer, 1975.

[36] F. A. Stevie and C. L. Donley, "Introduction to X-ray Photoelectron Spectroscopy," *Journal of Vacuum Science Technology*, vol. 38, no. 6, p. 063204, 2020.

[37] P. Gill, T. T. Moghadam, and B. Ranjbar, "Differential Scanning Calorimetry Techniques: Applications in Biology and Nanoscience," *Journal of Biomolecular Techniques*, vol. 21, no. 4, pp. 167–193, 2010.

[38] B. Feng, X. Fang, H.-X. Wang, W. Dong, and Y.-C. Li, "The Effect of Crystallinity on Compressive Properties of Al-PTFE," *Polymers*, vol. 8, no. 10, 2016.

[39] Z. Tang, M. Wang, F. Tian, L. Xu, and G. Wu, "Crystal Size Shrinking in Radiation Induced Crosslinking of Polytetrafluoroethylene: Synchrotron Small Angle X-ray Scattering and Scanning Electron Microscopy Analysis," *European Polymer Journal*, vol. 59, pp. 156–160, 2014.

[40] B. Feng, X. Fang, H.-X. Wang, W. Dong, and Y.-C. Li, "The Effect of Crystallinity on Compressive Properties of Al-PTFE," *Polymers*, vol. 8, no. 10, p. 356, 2016.

[41] W. Ge, S. Zhao, C. Wang, H. Liu, Y. Su, J. Huang, Z. Gao, J. Xue, and Y. Wang, "A Model for Dose Dependence of the Void Swelling in Electron-Irradiated Alloys," *Metals*, vol. 12, no. 2, p. 244, 2022.

[42] S. I. Choi and J. H. Kim, "Radiation-Induced Dislocation and Growth Behavior of Zirconium and Zirconium Alloys - A Review," *Nuclear Engineering and Technology*, vol. 45, no. 3, pp. 385–392, 2013.

[43] T. Ungár, P. Frankel, G. Ribárik, C. P. Race, and M. Preuss, "Size Distribution of Irradiation Induced Dislocation Loops in Materials Used in the Nuclear Industry," *Journal of Nuclear Materials*, vol. 550, p. 152945, 2021.

[44] B. Yao, D. J. Edwards, and R. J. Kurtz, "TEM Characterization of Dislocation Loops in Irradiated bcc Fe-Based Steels," *Journal of Nuclear Materials*, vol. 434, no. 1, pp. 402–410, 2013.

[45] J. Brechtl, M. Crespillo, S. Agarwal, H. Bei, and S. Zinkle, "Effects of Irradiation Spectrum on the Microstructural and Mechanical Properties of Bulk Metallic Glasses," *Journal of Nuclear Materials*, vol. 533, p. 152084, 2020.

[46] M. Kiritani, "Recoil Energy Effects and Defect Processes in Neutron Irradiated Metals," *Journal of Nuclear Materials*, vol. 155-157, pp. 113–120, 1988.

[47] W.-Y. Chen, J. D. Poplawsky, Y. Chen, W. Guo, and J.-W. Yeh, "Irradiation-Induced Segregation at Dislocation Loops in CoCrFeMnNi High Entropy Alloy," *Materialia*, vol. 14, p. 100951, 2020.

[48] J. Yu, Y. Chen, Q. Yang, Y. Shi, Y. Yao, X. Li, and Y. Wang, "Microstructural Changes of 316L Stainless Steel Under Energetic Alpha Particle and Proton Irradiation at 500°C," *Chinese Institute of Atomic Energy*, vol. 191-194, pp. 728–732, 1992.

[49] T. A. Aljohani, M. H. Geesi, and A. Kaiba, "Evidence for Enhancement of Corrosion Resistance of Carbon Steel After Exposure to High-dose Gamma Radiation," *Journal of Saudi Chemical Society*, vol. 23, no. 5, pp. 525–535, 2018.

[50] M. Krause, R. Haire, O. Keski-Rahkonen, and J. Peterson, "Photoelectron Spectrometry of the Actinides From Ac to Es," *Journal of Electron Spectroscopy and Related Phenomena*, vol. 47, pp. 215–226, 1988.

[51] C. J. Smithells, *Smithells Metals Reference Book*. Oxford, United Kingdom: Butterworth-Heinemann, eighth ed., 2004.

[52] H. W. Starkweather Jr., P. Zoller, and G. A. Jones, "The Heat of Fusion of Polytetrafluoroethylene," *Journal of Polymer Science*, pp. 751 – 761, 1982.

[53] K. Yamaguchi and S. Ueda, "High temperature enthalpy measurement of sus340 stainless steel," *High Temperature Materials and Processes*, vol. 30, no. 6, pp. 569–572, 2011.